UNIVERSIDADE FEDERAL DO CEARÁ

CENTRO DE CIÊNCIAS

DEPARTAMENTO DE FÍSICA

PROGRAMA DE PÓS-GRADUAÇÃO EM FÍSICA

DOUTORADO EM FÍSICA

DANIEL BRITO DE ARAÚJO

SURFACE INTERACTIONS IN MOS_2: A STUDY ON THE EFFECTS OF CONTACT ON A 2D SEMICONDUCTOR

FORTALEZA

2023

DANIEL BRITO DE ARAÚJO

SURFACE INTERACTIONS IN MOS_2: A STUDY ON THE EFFECTS OF CONTACT ON A 2D SEMICONDUCTOR

Tese apresentada ao Programa de Pós-Graduação em Física do Centro de Ciências da Universidade Federal do Ceará, como requisito parcial à obtenção do título de doutor em Física. Área de Concentração: Física

Orientador: Prof. Dr. Eduardo Bedê Barros

Coorientadora: Prof. Dr. Stephanie Reich

FORTALEZA

2023

Dados Internacionais de Catalogação na Publicação
Universidade Federal do Ceará
Sistema de Bibliotecas
Gerada automaticamente pelo módulo Catalog, mediante os dados fornecidos pelo(a) autor(a)

D32s de Araújo, Daniel Brito.
SURFACE INTERACTIONS IN MOS2: A STUDY ON THE EFFECTS OF CONTACT ON A 2D SEMICONDUCTOR / Daniel Brito de Araújo. – 2023.
98 f. : il. color.

Tese (doutorado) – Universidade Federal do Ceará, Centro de Ciências, Programa de Pós-Graduação em Física , Fortaleza, 2023.
Orientação: Prof. Dr. Eduardo Bedê Barros.
Coorientação: Profa. Dra. Stephanie Reich.

1. MoS2. 2. Strain. 3. Gold Nanoparticles. 4. Excitons. 5. Plasmons. I. Título.

CDD 530

DANIEL BRITO DE ARAÚJO

SURFACE INTERACTIONS IN MOS_2: A STUDY ON THE EFFECTS OF CONTACT ON A 2D SEMICONDUCTOR

Tese apresentada ao Programa de Pós-Graduação em Física do Centro de Ciências da Universidade Federal do Ceará, como requisito parcial à obtenção do título de doutor em Física. Área de Concentração: Física

Aprovada em: 10 de Julho de 2023

BANCA EXAMINADORA

Prof. Dr. Eduardo Bedê Barros (Orientador)
Universidade Federal do Ceará (UFC)

Prof. Dr. Stephanie Reich (Coorientadora)
Freie Universität Berlin (FUB)

Profa. Dra. Jenaína Ribeiro Soares
Universidade Federal de Lavras (UFLA)

Dr. Florian Schulz
Universität Hamburg (UH)

Prof. Dr. Diego Rabelo da Costa
Universidade Federal do Ceará (UFC)

Prof. Dr. Antônio Gomes de Souza Filho
Universidade Federal do Ceará (UFC)

ACKNOWLEDGEMENTS

This work is not mine, it was made by multiple hands and it belongs to all those involved in it, be it in the past or in the future. I would not be able to present such a scientific work without the hard work and great company of my advisor Prof. Dr. Eduardo Bedê Barros, who extended his hand and his network to me, making my study in Berlin posible, with my co-advisor Prof. Dr. Stephanie Reich, whom I thank for the guidance and support. I thank my advisors for taking their time to teach me physics and how to do science.

Agradeço a meu pai, José Carlos de Araújo, maior conselheiro profissional e a voz do meu superego. Agradeço à minha mãe, Liana Brito de Castro Araújo, que me deu carne, corpo e terapia! Meus primeiros e maiores professores, que sempre estimularam minha curiosidade e meus estudos, me apoiando ao longo de toda minha vida. Sou feliz em ter dois irmãos com quem compartilhar a vida numa intimidade que só irmãos sabem, Filipe e Jaqueline, eu amo muito vocês! (Mesmo querendo fugir às vezes). Também me alegra e dá energia a pequena Assussena! Eu sei que gosto mais de batata e mais de estudar, mas eu gosto mais, mais mesmo de vocês.

Agradeço aos meus outros pais e mães que descobri no caminho, eu sempre me achei sortudo, mas ter vocês em minha vida é algo muito maior do que qualquer sorte. Dani, Márcio e Marisa frutos da minha linda e real amizade com o Rafa, essênciais na formação do que sou hoje. Tia Lúcia Helena e minha irmãzinha Júlia, que me são casa. Tio Duda, tia Ofélia, Beatriz e Levi cuja acolhida me fez renascer mais de uma vez, é da casa deles (da minha torre na casa deles) que escrevo essa tese, paquerando de frente com a Chapada do Araripe (-Obrigado, chapada! -De nada, chapado!). Vocês me são solo firme em momentos de ventania. À Beatriz agradeço mais de uma vez, pois não só enche meu tanque nas conversas de cidade, rua, Marx, memes, na intimidade, mas também trabalhou ativamente nesta tese produzindo quase todas as figuras.

À minha família com seus desafios, cheia de amor e cheia de professores. Vovó Miryam; Dilva; tia Beth, conselheira acadêmica e motorista; tia Teca, don Teresa, fonte de força; tia Titá e Gabi (buchuda!) e nossas conversas infinitas; Mariana (olha a licenciatura vindo aí!); Marina, André Luís e Gabriel; Vitor e Cá; os muito mais primas, primos, tias e tios.

À minha terapeuta, Dra. Silvia Rosane, que acompanha meus caminhos e tropeços à muito tempo e me ajuda e encontrar, se não o caminho certo, pelo menos o meu caminho!

Às minhas amizades que fazem a vida valer à pena! To my friends who make life worth living! A mis amistades que hacen que la vida valga la pena! Mein Deutsch ist immer noch schlecht, es tut mir leid, Freunden! Agê, Dani, Hanna, Bruna, Erinaldo, Carol, Vitor, Carmen,

Júnior, Thithi, Sapão, Vitle, Vivi, Eline, Quel, Mardônio, Inaldo, Vinicius, Dani, Euníce, Fia, Neguim, Diana, Lis, José, Lucas, Ramon, Misa, Manelzão, Manelzim, Mathusa, André, Nena, Brício, Carlos William, Saulo, AllEyezonWeed, Gás Hélio, Yanjie, Jiajuin, Francesca (and her lovely family!), Olga, Felix, Laura, La Gabi, Arseniy, Igor, Aditya, Charlotte, José, Oisín, Sabrina, Pedro, Bruna, Camila, Dam, Naiara, Felipe, Arthur, Juliana, Rodrigo, Brennda, Sullas, Suzi, Ioná, Felipe, Sabrina, Gabi, Victor, Larissa, Gabriel, Raquel, Max .

I thank collaborators and staff that facilitated my work. Rejane, Luis P., Jan Kirchhof, Alphonse, Alen, Kati, Moritz, Gudrun, Alen, Leo Campos, Rodrigo Almeida (who measured the I-V curves in Chap. 4), Andreij Gadelha, Natália Rezende, Carlos Salomão, Beatriz Mendes (who made all the figures, except for the ones in Chap. 4), Florian Schulz.

I thank CAPES CAFe and Portal de Periódicos for allowing me access to many valued publications. I thank Sci-Hub and LibGen for allowing me access to all the other publications.

The funding parties: I thank my parents for the financial support; this work was partly funded by the National Council for Scientific and Technological Development (CNPq); this study was financed in part by the Coordenação de Aperfeiçoamento de Pessoal de Nível Superior - Brasil (CAPES) - Finance Code 001 (Process 88887.583613/2020-00) for my sandwich; this work was partly funded by the European Research Council (ERC).

"Se você derruba uma moeda em uma rua escura,
o primeiro lugar a procurar é embaixo do poste."
–"If you drop a coin in a dark street, the first place
to look is under the light-post."

(Prof. Dr. Josué Mendes Filho)

ABSTRACT

This work investigates the influence of surface interactions in the properties of the 2D semiconductor MoS_2 when integrated in heterostructures. The work is done experimentally, it qualitatively and quantitatively describes the interaction of thin exfoliated MoS_2 under different contact conditions. In the first experiment, the MoS_2 was placed in a gold substrate and contacted from the top by a metallic Atomic Force Microscope (AFM) tip. The current-voltage curve of the tip-MoS_2-gold heterostructure was measured for different contact forces, an improvement on previously proposed circuit model is done by means of the new "3-diode" model. Through the proposed model we are able to measure the variation of the valence band energy in the MoS_2 with respect to the tip's contact force - the rates of change are 0.21, 0.23, and 0.78 meV/nN for the few-layers, three-layers, and two-layers MoS_2, respectively. In the second experiment, we placed the MoS_2 on top of a gold nanoparticle (NP) supercrystal - a plasmonic structure with high light-matter interaction. We measure and analyse the optical behaviour of the heterostructure with a micro-absorbance setup, noting the excitons in the MoS_2 are drastically affected by the evanescent dielectric screening of the supercrystal, with a blue-shift of a few hundred meV in the excitons' resonance energy. The plasmonic modes seem not to vary with the presence of the monolayer semiconductor, but by growing the number of MoS_2 layers, the influence of the dipole moment from the excitons leads to a red shift in plasmonic resonance. This thesis also includes a step-by-step description of the supercrystal fabrication procedure developed by collaborators, we show how to grow gold nanoparticles, functionalize their surface and use them to grow supercrystals. This is done in an attempt to spread the knowledge and usage of this new material with record high light-matter interaction.

Keywords: MoS2; Strain; Gold Nanoparticles; Excitons; Plasmons.

RESUMO

Este trabalho investiga a influência das interações de superfície nas propriedades do semicondutor bidimensional MoS_2 quando integrado em heteroestruturas. O trabalho é feito experimentalmente, descrevendo qualitativa e quantitativamente a interação de filmes finos de MoS_2 sob diferentes condições de contato. No primeiro experimento, o MoS_2 foi colocado em um substrato de ouro e contatado de cima por uma ponta metálica de Microscópio de Força Atômica (AFM). A curva de corrente-tensão da heteroestrutura ponta-MoS_2-ouro foi medida para diferentes forças de contato, uma melhoria no modelo de circuito proposto anteriormente é feita por meio do novo modelo "3-diodos". Através do modelo proposto conseguimos medir a variação da energia da banda de valência no MoS_2 em relação à força de contato da ponta - as taxas de variação são 0,21, 0,23 e 0,78 meV/nN para poucas camadas , três camadas e duas camadas de MoS_2, respectivamente. No segundo experimento, colocamos o MoS_2 no topo de um supercristal de nanopartículas de ouro (NP) - uma estrutura plasmônica com alta interação luz-matéria. Medimos e analisamos o comportamento óptico da heteroestrutura com uma configuração de microabsorção, observando que os excitons no MoS_2 são drasticamente afetados pela blindagem dielétrica evanescente do supercristal, com um desvio para o azul de algumas centenas de meV na energia de ressonância dos éxcitons. Os modos plasmônicos parecem não variar com a presença de uma monocamada do semicondutor, mas ao aumentar o número de camadas do MoS_2, a influência do momento de dipolo dos excitons desvia para o vermelho a ressonância plasmônica. Esta tese também inclui uma descrição passo a passo do procedimento de fabricação de supercristais desenvolvido por colaboradores, mostramos como crescer nanopartículas de ouro, funcionalizar sua superfície e usá-las para crescer supercristais. Isso é feito na tentativa de difundir o conhecimento e o uso desse novo material com recorde de força da interação luz-matéria.

Palavras-chave: MoS2; Deformação; Nanopartículas de Ouro; Excitons; Plasmons.

LIST OF FIGURES

Figure 7 – Key steps in the NP growth and supercrystal formation, with zoomed representation of the particle's configuration after each represented step, note the simplistic representations of the encapsulating molecules CTAB, CTAC and PSSH in the bottom-right corner of the figure. (a) Formation of Au clusters capped with CTAB via pipette one-shot injection of $NaBH_4$ in $HAuCl_4$-CTAB solution in water bath at 27ºC and with a magnetic stir rotating at 800 rpm (Sec. 3.2.1.1). (b) Generation of first generation Au spherical nanoparticles (NPs) by pressing the balloon attached to the volumetric pipette and rapidly injecting 20 mL of $HAuCl_4$ into the clusters in CTAC solution, the magnetic stir is at 600 rpm (Sec. 3.2.1.2). (c) Second generation NPs are formed by using a syringe-pump for the dropwise addition of 20 mL $HAuCl_4$ (during 1 hour) to the 1st generation NPs in CTAC, done in a water bath at 27ºC and with the magnetic stir at 400 rpm (Sec. 3.2.1.3). Step (c) may be repeated to grow larger nanoparticles. (d) The particles are functionalized with the specific PSSH cover (check table 4) by using a pipette to dropwise add 0.5 mL of concentrated NPs in CTAC to a THF and PSSH solution stirred at 700 rpm. (e) THF and water are evaporated from the solution in a rotary evaporator at 250 rpm with a water bath of 40ºC, leaving the dry nanoparticles in the wall of the round-bottomed flask to be latter dissolved in toluene (Sec. 3.2.1.4). (f) With the PSSH functionalized NPs now dissolved in toluene, a phase separation procedure is made by mixing and shaking water and ethanol in a flask with cap, any residual molecules soluble in water or ethanol are then removed by separating the phases in the flask. (g) The final solution of PSSH capped NPs is placed on top of DEG in a Teflon well. As the toluene slowly evaporates the nanoparticles gradually self-assemble into the supercrystal in the liquid sub-phase (visible in the zoomed representation). The substrate onto which the supercrystals will attach is visible inside the DEG sub-phase, a thin glass slide is placed on top of the Teflon well to assure slow evaporation of the toluene. A thin hole (1 mM) is visible in the bottom of the well, once the toluene is completely evaporated and the supercrystals are left floating on the DEG surface a syringe is placed in the hole and the DEG is carefully removed from the bottom of the well, leaving the supercrystals in the surface of the substrate. 48

Figure 26 – Passos principais no crescimento de nanopartículas e formação de supercristais, com zoom na configuração das partículas após cada etapa representada, veja as representações simplistas das moléculas de encapsulamento CTAB, CTAC e PSSH no canto inferior direito canto da figura. (a) Formação de aglomerados de Au encapsulados com CTAB via injeção única de $NaBH_4$ em solução de $HAuCl_4$-CTAB em banho-maria a 27ºC e com agitador magnético a 800 rpm (Sec. B.1). (b) Geração de NPs esféricas de primeira geração, pressiona-se o balão preso à pipeta volumétrica para injetar rapidamente 20 mL de $HAuCl_4$ na solução de aglomerados em CTAC, a agitação magnética é de 600 rpm (Sec. B.2). (c) As NPs de segunda geração são formadas por meio de adição gota a gota de 20 mL de $HAuCl_4$ (durante 1 hora com uma bomba para seringa) às NPs de 1ª geração em CTAC, feito em banho-maria a 27ºC e com agitação magnética a 400 rpm (Sec. B.3). A etapa (c) pode ser repetida para crescer nanopartículas maiores. (d) As partículas são funcionalizadas com o PSSH específico (ver tabela 4) usando uma pipeta para adicionar gota a gota 0,5 mL de NPs em CTAC a uma solução de THF e PSSH agitada a 700 rpm. (e) THF e água são evaporados da solução em rotaevaporador a 250 rpm com banho-maria a 40ºC, deixando as nanopartículas secas na parede do balão de fundo redondo para serem posteriormente dissolvidas em tolueno (Sec. B.4). (f) Com as NPs funcionalizadas com PSSH dissolvidas em tolueno, um procedimento de separação de fases é feito misturando e agitando água e etanol em um frasco com tampa, quaisquer moléculas residuais solúveis em água ou etanol são removidas separando as fases no frasco. (g) A solução final de NPs com PSSH é colocada em cima de DEG em um poço de Teflon. À medida que o tolueno evapora, forma-se o supercristal na subfase líquida (visível no zoom). O substrato final é visível dentro da subfase DEG, uma lâmina de vidro fina é colocada no topo do poço de Teflon para que o tolueno evapore lentamente. Quando o tolueno evapora os supercristais ficam flutuando, uma seringa é colocada no orifício (1 mm) no fundo do poço e o DEG é cuidadosamente removido, deixando os supercristais no substrato. . 97

LIST OF TABLES

CONTENTS

[1] This section was published in the Supplementary Information of the paper: De Araujo *et al.* (2020). **Controlling the electronic bands of a 2D semiconductor by force microscopy**. *2D Materials*, 7(4), 045029. doi.org/10.1088/2053-1583/aba5cb. One of the products of this Thesis.

[2] This section was published in the same reference given in the previous footnote

[3] This section was published in the Supplementary Information of the paper: De Araujo *et al.* (2020). **Controlling the electronic bands of a 2D semiconductor by force microscopy**. *2D Materials*, 7(4), 045029. doi.org/10.1088/2053-1583/aba5cb. One of the products of this Thesis.

[4] This section has been published in the same Supplementary Information mentioned in the previous footnote.

[5] This section was also published in the same Supplementary Information mentioned in previous footnotes.

1 INTRODUCTION

This thesis is the product of a long path of study that includes: attending advanced classes; deep and constant literature reading; long hours at the lab, be it preparing samples, taking measurements or setting up the equipments; long hours in front of the computer, plotting graphs, writing, modelling, analysing and fitting the results; many meetings and discussions with my advisors, colleagues, collaborators and friends who were daring enough to ask. The process that took me here includes many obstacles and mistakes overlooked in this thesis, including: losing data to corrupted media; retaking measurements due to bad calibration; dropping (and destroying!) a great sample on the floor; making science under a denialist government; a world-wide pandemic; the risk of a nuclear war; depression; not to mention projects finished with simply uninteresting results. The whole process, be it published or not, made me understand science in a deeper level, for this I believe I've earned the title of doctor, although I do not intend to abandon the title of student.

I see my approach to research in a similar way thought to me by the late Prof. Dr. Josué Medes Filho, and to the one described by Novoselov (whose outstanding research started my field of study): I prepare my research projects as I prepare my lunch, I first see what is available in my fridge before deciding what to eat.

This work is composed of two main chapters (4 and 5), both investigating bidimensional (2D) Molybdenum Dissulfide, but in different experimental approaches. I start by reviewing key concepts in the Literature Review chapter (Chap. 2), the reader familiar with the field might skip most of it, although there are some specific theory also presented here, one might save this read for when the concepts are demanded (proper references to sections are given throughout the text - with hyperlinks in the PDF version). In chapter 3, I mention MoS_2, the main material investigated, I intend to convince the reader of its importance to today's science and the technology of tomorrow. The methods to prepare and transport the MoS_2 samples are given in the Materials and Methods chapter 3, in it are also the description and preparation procedures for gold nanoparticles and their supercrystal - used as a plasmonic substrate in chapter 5. The description of the methods that are used in this investigation are also given in chapter 3.

After the introductory chapters, in chapter 4, we use Atomic Force Microscopy (AFM), specifically the Conductive AFM (CAFM), to apply an extensive range of loading forces - up to $F = 980$ nN - ten times more than ever reported before the publication[1]. The in-depth

[1] The work presented in this chapter, as well as in sections 2.3 and 2.4, was published in: De Araujo, D. B., De

exploration of the high-force domain enables us to understand better the physical meaning of the non-ideal Schottky contact present in nanometric scale contact between a metal and the semiconductor. We improve previously proposed model(QUEREDA *et al.*, 2017), incorporating the variation of the Schottky Barrier Height (SBHs) as an explicit function of the applied force. The excellent agreement between our model and the experimental data enables us to estimate how fast the MoS_2-Au Schottky barrier changes as a function of force. This model gives us a more direct approach for probing the changes in the electronic bands of the studied 2D semiconductor. Also, our model incorporates more details about the whole setup (tip-MoS_2 -Au), including the geometry, and exploring the multiple current regimes. We find two different regimes in the current between the MoS_2 flake and the Au substrate: one in which the current is spread along the MoS_2 flake surface in the low force regime and one in which the current is localized near the area of the tip-flake contact in the high force regime. This understanding of the geometric influence on the current behaviour brings forward the role of the Schottky Barrier inhomogeneity on the voltage dependence of the effective SBH, shining new light on the physical meaning of the non-ideality of the Schottky contacts in CAFM measurements. Altogether, the results of this chapter introduce new possibilities of applying Force Microscopy to probe the electronic properties of 2D semiconducting materials and to understand how to control these properties.

The second part of the investigative work is given in chapter 5. In it, we verify exciton-plasmon interactions in contacted surfaces by taking advantage of having access to a novel material with very interesting properties, the gold nanoparticles (NPs) supercrystal developed by our collaborators(SCHULZ *et al.*, 2017). This material hosts light-matter interaction in the ultra- and deep-strong coupling regimes, unprecedented in ambient conditions. By placing MoS_2 on top of the supercrystal, we verify the effect of the dielectric screening in the excitons that govern the optical behaviour of our studied semiconductor, it shifts the energy of the A and B excitons up in the order of a few hundred meV. This is due to the high index of refraction of the substrate that drastically changes the force fields of the excitons. This effect acts only on excitons formed in an evanescent volume by the supercrystal surface and becomes greatly apparent in monolayer MoS_2. The total dipole moment of the excitons in MoS_2 also affects the behaviour of the collective plasmons of the substrate, red-shifting it when the excitonic density is high enough (found in three and more MoS_2 layers).

Almeida, R. F., Gadelha, A. C., Rezende, N. P., Salomão, F. C. C. S., Silva, F., Campos, L. C., &Barros, E. B. (2020). **Controlling the electronic bands of a 2D semiconductor by force microscopy**. *2D Materials*, 7(4), 045029. doi.org/10.1088/2053-1583/aba5cb. The text presented is heavily based on the published text.

In the final chapters of the thesis, we present our general conclusions (chapter 6) with the products achieved during the doctorate, some extra images that aid the interpretations presented in chapter 5 are given in the appendix A, and a translation to Portuguese of the fabrication procedures of the supercrystal (section 3.2.1) is given in the appendix B with the intent of knowledge importation to Brazillian and Portugue-speaking research institutions.

2 LITERATURE REVIEW

In this chapter we will bring theoretical concepts that are important to the understanding of this work. The intent is to have in this text a readily available brief review of concepts needed for the clear understanding of the thesis. References lead to text books, review papers and fundamental papers with a deeper discussion on the subjects.

2.1 Crystals

Physics uses symmetries to obtain conservation laws that help determining the properties of systems, solid state abides by this. Ideal crystals are structures with translation symmetry, that is to say: if an observer looks at a crystalline structure at one point, they cannot tell the difference between this point and any other point displaced by a lattice vector (See Fig. 1)(KITTEL, 2018). A lattice vector (**R**) is any linear integer combination of the vectors that compose the lattice - the basis vectors, namely $\mathbf{a_1}$, $\mathbf{a_2}$ and $\mathbf{a_3}$:

$$\mathbf{R} = n_1.\mathbf{a_1} + n_2.\mathbf{a_2} + n_3.\mathbf{a_3} \tag{2.1}$$

$$O(\mathbf{r} + \mathbf{R}) = O(\mathbf{r}) \tag{2.2}$$

with n_1, n_2 and n_3 being integers and O any observable of the system with translation symmetry.

Crystals can be categorized by their dimensionality, determined by the portion of space filled by the lattice. Typical natural specimens like diamond and quartz fill a volume and are said to be 3D crystals. On the other hand, structures that have periodic boundaries only on a plane are said to be 2D crystals, as is the case of graphene. There are also 1D and 0D (zero-D) crystalline structures, as nanotubes and quantum dots, respectively.

Usual crystals have atoms or molecules composing their lattice, but the definitions are broader and allow the same physical treatment to apply to structures made up of more complex building blocks, like nanoparticles. For the sake of clarity, we chose to name *supercrystals* the crystalline structures composed of nanoparticles (given that each nanoparticle has its own crystalline structure).

The research presented in this thesis works with MoS_2, a hexagonal 2D crystal, as well as a 3D face-centered cubic (FCC) supercrystal composed of gold nanoparticles (see Fig. 1).

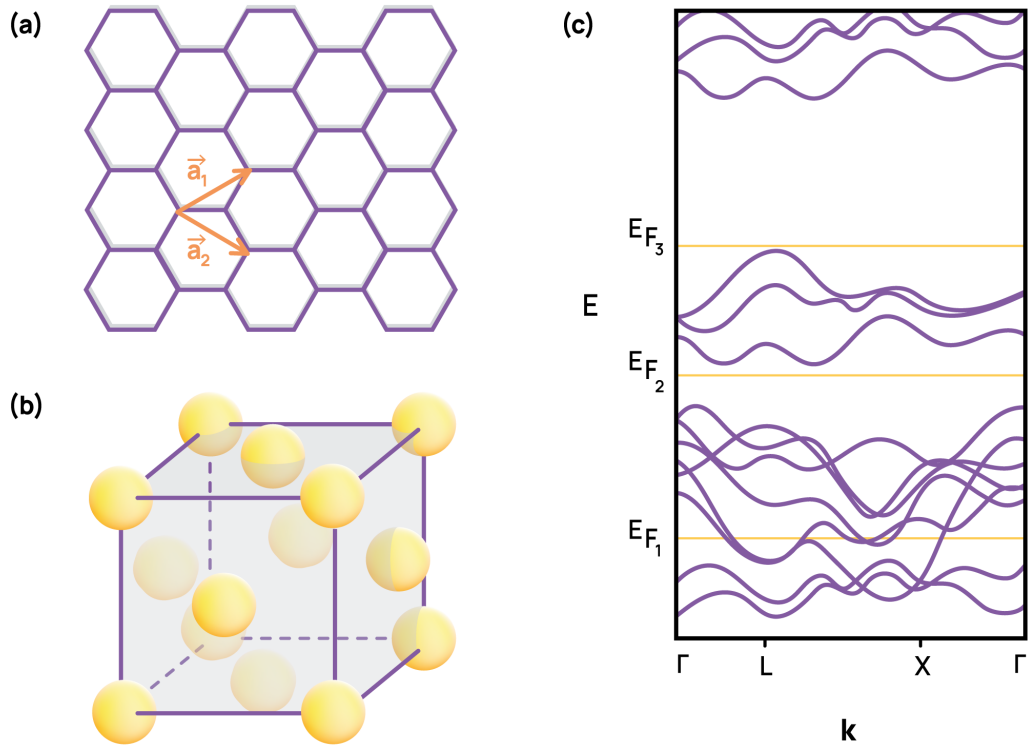

Figure 1 – Examples of crystal lattice: (a) a 2D hexagonal lattice with the base lattice vectors shown as $\mathbf{a_1}$ and $\mathbf{a_2}$; (b) a face-centered cubic (FCC) structure, an example of a 3D crystal. The lattice vectors are any vectors that obey Eq. (2.1). (c) Example of an electronic band structure. A solid can be categorized accordingly to its Fermi energy's position: E_{F1} would mean a metallic behaviour; E_{F2} a semiconductor behaviour; and E_{F3} an insulator.

2.2 Band Structure

The behaviour of electrons inside a solid determines the solid's electronic properties (is it a conductor or an insulator?), as well as its optical response. So, by finding the Hamiltonian of the electrons in a solid ($\hat{\mathbf{H}}_\mathbf{e}$), one may solve Schrödinger's equation to find the energetic bands available for (and occupied by) the electrons(KITTEL, 2018). The Hamiltonian is determined by all the interactions felt by the electrons, they are: electron-ions interactions ($\hat{\mathbf{H}}_{\mathbf{e-i}}$); electron-electron interactions ($\hat{\mathbf{H}}_{\mathbf{e-e}}$); and electrons-external field interactions ($\hat{\mathbf{H}}_{\mathbf{ext}}$):

$$\hat{\mathbf{H}}_\mathbf{e} = \hat{\mathbf{H}}_{\mathbf{e-i}} + \hat{\mathbf{H}}_{\mathbf{e-e}} + \hat{\mathbf{H}}_{\mathbf{ext}} \tag{2.3}$$

The most common approach to the very complex system of a crystal is the Born-Oppenheimer (BO) approximation. Given the much larger mass of the ions, electrons move through the solid much faster than the ions' oscillations, so it is reasonable to de-couple their interaction into the electron interacting with the stationary ions at their equilibrium position ($\hat{\mathbf{H}}_{\mathbf{e-i_0}}$); and the electrons interacting with the ionic oscillations, known as phonons in their particle treatment ($\hat{\mathbf{H}}_{\mathbf{e-phon.}}$). In the BO treatment, the problem is solved as if for a single

electron, once the single-electron band structure is known, we count the number (or density to be more precise) of electrons in the solid and fill the energy bands from bottom-up while respecting Fermi's exclusion principle - two fermions (electrons in our case) cannot occupy the same state at the same time. Any need to improve the system's model due to electron-electron interactions is treated as perturbations. At absolute zero temperature, the energy of the last electron placed in the bands is named Fermi energy (E_F), and the band structure around this area determines the electronic conductivity and the optical behaviour of the solid.

Given the translation symmetry in real **r** space (Eqs. 2.1 and 2.2), it is most convenient to treat crystals' Hamiltonians in the Fourier transform coordinates, known as the reciprocal or **k** space - just like the frequency (ω) is the Fourier transform of time. The symmetries governed by the lattice vectors $\mathbf{a_i}$, translate into symmetries of the reciprocal lattice governed by the reciprocal basis vectors $\mathbf{b_i}$ (Eq. 2.4), the reciprocal space unit cell is named Brillouin Zone (BZ) (a_i and b_i are linked by Eq. 2.4). The band structure of crystals is, thus, the available states of the system given in their energies as function of the **k** vectors inside the Brillouin Zone. The reciprocal space is not only a mathematical tool, the **k** coordinates are linearly related to the particle's momentum by Eq. 2.5.

$$\mathbf{b_i} \cdot \mathbf{a_j} = 2\pi\delta_{ij} \tag{2.4}$$

$$\mathbf{p} = \hbar\mathbf{k} \tag{2.5}$$

δ_{ij} is the Kronecker delta, **p** is the momentum and $\hbar$ is the reduced Planck constant. It is valuable to note that Eq. 2.5 is given for free-space. In a crystal, any reciprocal lattice vector ($\mathbf{G} = \sum n_i \mathbf{b_i}$, with integer n_i) may be added to **k** leading to the same wave function, due to the symmetry in reciprocal-space.

Looking at the electronic band structure we may classify the solid in relation to its conductivity: if E_F lies in the middle of a band, then the higher energy electrons may interact with any weak external electric field (**E**) occupying neighboring energy states, this comes with a displacement of the electron's momentum, leading to a current - this solid is said to be *conductive* or *metallic*. If E_F is such that one band is completely filled with electrons, while the next available band has much higher energy (we call this energy difference the energy-gap, or E_{gap}), then **E** cannot change the momentum of the electrons because there are no available states in its vicinity, thus the solid is said to be an *insulator* (typically $E_{gap} \geq 5$ eV). If E_{gap} is in the order of 100 meV up to 4 eV, then the solid is only conductive beyond a certain voltage (E_{gap}) and it is said to be a *semiconductor*. Figure 1(c) depicts this.

2.2.1 *Excitons*

In semiconductors, valence electrons can be excited into the conduction band by the absorption of visible photons ($E_{photon} \sim 2eV$), the vacancy left in the valence can be treated as a particle, namely *hole*, with an effective mass similar to the electron's, but with a positive charge. If the hole and the excited electron have the same group velocity, they may interact via Coulomb force in a similar way to the electron-proton interaction in the Hydrogen atom (Eq. 2.6), this leads to the formation of a composite electron-hole particle named *exciton*(KITTEL, 2018; YU PETER Y., 1996). The binding energy of the exciton is observed experimentally by the absorption of photons with energy lower than the bandgap ($E_{abs} = E_{gap} - E_{exciton}$). In the time between the formation of an exciton and its recombination (by emission of a photon) the exciton may move through the crystal and may interact with other particles, sometimes even forming excitonic complexes. The exciton's lifetime is much smaller in direct bandgap semiconductors, this is due to momentum conservation that demands excitons in indirect bandgap materials to interact with a moment carrying particle (namely, phonons), visible photons have too low momentum for this. The electron-hole interaction is given by (in CGS units):

$$U(r) = \frac{-e^2}{\varepsilon r} \tag{2.6}$$

where e is the elementary charge, ε is the dielectric function and r is the electron-hole distance. The excitonic behaviour described here is focused on weakly bound (Mott-Wannier) excitons, and a deeper describtion is available in the references (KITTEL, 2018; YU PETER Y., 1996).

2.3 Schottky contact theory[1]

When a metal is made to touch a semiconducting material we call it a a metal-semiconductor (M- SC) junction. Given the different energy of the uppermost electrons (E_F), the particles right at the M-SC surface will feel a force towards the lower energy. So the electrons (or holes) will flow from the semiconductor to the metal until the Fermi energies of both materials align. This charge transfer will leave the semiconductor with a lack (or excess) of electrons, i.e. the material will be charged in a depletion zone near the M-SC contact.

The potential barrier formed in a metal-semiconductor (M-SC) junction (due to surface charge transfer) is called the Schottky barrier. The thermionic electrical current through

[1] This section was published in the Supplementary Information of the paper: De Araujo *et al.* (2020). **Controlling the electronic bands of a 2D semiconductor by force microscopy**. *2D Materials*, 7(4), 045029. doi.org/10.1088/2053-1583/aba5cb. One of the products of this Thesis.

an ideal Schottky barrier can be calculated by the equations(TUNG, 1992; OHDOMARI; TU, 1980):

$$I = I_0 \exp\left(\frac{V}{V_T}\right)\left[1 - \exp\left(\frac{-V}{V_T}\right)\right] \tag{2.7}$$

where

$$I_0 = AcA^*T^2 \exp\left(\frac{-\varphi}{V_T}\right) \tag{2.8}$$

with V_T being the thermal voltage:

$$V_T = \frac{k_b T}{e} \tag{2.9}$$

Here, I_0 is the saturation current, e is the fundamental charge, V is the applied voltage, T is the temperature (300 K), k_b is Boltzmann's constant (8.617×10^5 eV/K), Ac is the contact area, A^* is the effective Richardson's constant (6.0087×10^5 A/m^{2}K^2, using $m^*/m_e = 0.5$), and φ is the Schottky's barrier potential height (SBH) in Volts.

2.3.1 Non-ideal Schottky contact

For the non-ideal case, it is common to add the empirical ideality factor n, such that the equation for the current is

$$I = I_0 \exp\left(\frac{V}{nV_T}\right)\left[1 - \exp\left(\frac{-V}{V_T}\right)\right]. \tag{2.10}$$

Note that the ideality factor is unity for the ideal contact and larger than 1 for non-ideal contacts.

2.3.2 Inhomogeneous barrier effect

Theoretical work has been done trying to shine some light on the nature and origin of the non-ideal behaviour of Schottky barriers and the physical meaning of the ideality factor(OHDOMARI; TU, 1980; TUNG, 1992). In one of such works, Tung discusses the non-ideal behaviour of contacts in terms of the non-homogeneity of the SBH along the contact surface(TUNG, 1992). By considering small regions with distinct SBH, Tung finds that the effective Schottky barrier for each small region (φ_i) is a function of the applied voltage across the M-SC junction. Within this model, the current through an M-SC junction is the sum of the current through all possible paths, each having a different effective SBH:

$$I(V) = A^*T^2\left[\exp\left(\frac{V}{V_T}\right) - 1\right]\sum_i Ac_i \exp\left(\frac{-\varphi_i}{V_T}\right) \tag{2.11}$$

in which the non-ideal behaviour is concentrated in the Ac_i and φ_i variables. As we will discuss later in this work (Sec. 4.4.1), we are dealing with one specific source of inhomogeneity, namely the one arising from the pressure and geometry of the metallic tip-semiconductor contact in Conductive Atomic Force Microscopy (CAFM) studies, but we do not want to rule out other possible sources. So we adapt Eq. 2.11 to include an ideality factor (n_0), which can differ from unity even with no applied pressure. The n_0 includes inhomogeneities that do not depend on the band bending caused by the applied force (this will be discussed in Sec. 4.4.1).

$$I(V) = A^* T^2 \exp\left(\frac{V}{n_0 V_T}\right)\left[1 - \exp\left(\frac{-V}{V_T}\right)\right] \times \sum_i Ac_i \exp\left(\frac{-\varphi_i}{V_T}\right) \tag{2.12}$$

in which Ac_i is the contact area for each region, and φ_i is the SBH for the respective region. It should be noted that in the original work, Ac_i is also considered a function of applied bias(TUNG, 1992), for simplicity, such dependence is ignored in the proposed model, discussed in Section 4.4.

2.4 Diode-resistor-diode model [2]

In chapter 4, we will analyse a CAFM experimental setup that consists of measuring the electric current of a metallic tip - thin MoS_2 - metallic substrate heterostructure. Such experiment has been reported before(QUEREDA *et al.*, 2017), where Quereda *et al.* proposed the Diode-Resistor-Diode (DRD) model presented here (QUEREDA *et al.*, 2017).

Each M-SC junction acts like a Schottky diode and, thus, we can build a model of the experiment as a circuit with two back-to-back diodes with a resistor in the middle (representing the internal resistance of the material as well as the contact resistances).

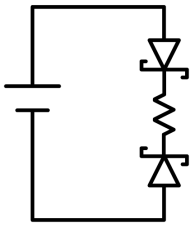

Figure 2 – Diode-Resistor-Diode circuit proposed by Ref. (QUEREDA *et al.*, 2017) to model CAFM measurements of thin MoS_2. The back-to-back diodes represent the metal-semiconductor interfaces of the tip-MoS_2-substrate heterostructure, while the resistor incorporates all the energy loss mechanisms of the system.

[2] This section was published in the same reference given in the previous footnote

The diode-resistor-diode circuit model obeys the following set of equations:

$$I_t(V_{tip}) = I_s(V_{sub}) = I(V) \tag{2.13}$$

$$V = V_{tip} + RI(V) + V_{sub}, \tag{2.14}$$

where I_t and I_s are the current in each diode (tip and substrate, respectively); V_{tip} and V_{sub} the voltages across each diode, R the electrical resistance of the system, I the total current, and V the total applied voltage.

With equations (2.8), (2.10), (2.13) and (2.14), it is possible to construct a numerical model and extract the I-V curve as a function of the contacts saturation currents (I_{tip}, I_{sub}), the contacts ideality factors (n_{tip}, n_{sub}), and the system resistance (R). By fitting the experimental curves with the model, we extract such parameters for each measurement.

2.5 Plasmonics

Applying an external electric field ($\mathbf{E}$) to a material leads to displacement of the charges of the materials in relation to their rest position. Inside a material the electric interaction is best described by the displacement field ($\mathbf{D}$) that is completely determined by $\mathbf{E}$ and the *dielectric function* (ε), through the equations 2.15 and 2.16. One simple enough way to visualize this is to picture an outermost electron of an atom being pushed by $\mathbf{E}$, thus, the pushed electron and its ion compose a dipole with its own electric field. Given the presence of a restoring Coulomb force between the displaced electron and its ion, the dipole oscillates, the collective movement of all the dipoles in a material is called *plasma oscillation* and it has an intrinsic frequency (ω_p), the quantum of a plasma oscillation is named *plasmon*(KITTEL, 2018; MAIER, 2007). The frequency dependent dielectric function ($\varepsilon(\omega)$) may be represented as a function of ω_p (Eq. 2.17, 2.18), and may be experimentally determined from reflectance measurements (Eq. 2.20, 2.19).

$$\mathbf{D}(t, \mathbf{r}) = \varepsilon \mathbf{E}(t, \mathbf{r}) \tag{2.15}$$

in frequency domain:

$$\mathbf{D}(\omega, \mathbf{k}) = \varepsilon(\omega, \mathbf{k})\mathbf{E}(\omega, \mathbf{k}) \tag{2.16}$$

where

$$\varepsilon(\omega) = 1 - \frac{\omega_p^2}{\omega^2 + i\gamma\omega} \tag{2.17}$$

with

$$\omega_p = \frac{4\pi n e^2}{m} \tag{2.18}$$

the equations are written in CGS units. ω is the light frequency, γ is the collision frequency, n is the electron concentration and m is the electron mass.

The measured reflectance (R) and the reflectivity coefficient (r) are:

$$R(\omega) = |r|^2 \tag{2.19}$$

$$r(\omega) = \frac{\sqrt{\varepsilon} - 1}{\sqrt{\varepsilon} + 1} \tag{2.20}$$

In metals, the plasmons come from the collective longitudinal excitations of the conduction electron gas, and may be excited by the reflection of photons. A more complete description of the dielectric function in metals (with *Au* in mind) includes the collision frequency (γ) that has a damping effect in the oscillations, and a residual polarization in the form of a background ε_∞(MAIER, 2007):

$$\varepsilon(\omega) = \varepsilon_\infty - \frac{\omega_p^2}{\omega^2 + i\gamma\omega} \tag{2.21}$$

Surface plasmons occur in metal-insulator interfaces, when applying an oscillating electro-magnetic field in sub-wavelength particles (nanoparticles, Sec. 3.2) a resonance may arise, we name this resonance *localized surface plasmon* (LSP), due to its non-propagating property. LSPs come with field amplification in the near-field area around the nanoparticle, this amplification has brought interest from the scientific community that finds application for metallic NPs as field-enhancing surfaces(MUELLER *et al.*, 2021). The external field (**E**) induces a dipole moment (**p**, not to be confused with the electron linear momentum given by Eq. 2.5) in a spherical metallic NP that is dependent on its radius (a), equations 2.22 and 2.23 show this relation explicitly.

$$\mathbf{p} = \varepsilon_m \alpha \mathbf{E} \tag{2.22}$$

$$\alpha = a^3 \frac{\varepsilon - \varepsilon_m}{\varepsilon + 2\varepsilon_m} \tag{2.23}$$

where α is the polarizability of the nanoparticle and ε_m is the dielectric function of the surrounding medium of the NP(MAIER, 2007).

Usual optically active materials have more than one plasmonic mode, due to the multiple possible oscillation modes of the induced dipoles. So, when modelling the dielectric

function, it is most convenient to be able to represent it as the sum of the effects of all the oscillation modes. The determination of the complex ε from Eq. 2.20 and 2.19 uses the Kramers-Kronig relations (Chap. 16(KITTEL, 2018)), so finding a form of ε that includes all the possible oscillations and that satisfies the Kramers-Kronig relations is desirable when one is trying to model the dielectric function of a material. Yilei Li proposes using the sum of Lorentzian oscillators in the form(LI, 2016):

$$\varepsilon(E) = 1 + \sum_{n=1}^{N} \frac{f_n}{E_n^2 - E^2 - iE\gamma_n} \tag{2.24}$$

where f_n is the strength, E_n the energy and γ_n is the linewidth of the n^{th} oscillator. E is the field energy, it may be converted into the light frequency using the identity:

$$E = \hbar\omega \tag{2.25}$$

2.5.1 Light-matter interaction

One very useful and important function of waves in a material is the *dispersion relation*, it is the relation between a wave's frequency and wavenumber ($\omega(\mathbf{k})$). From the dispersion relation one may obtain the phase and group velocities of a wave (ω/k and $d\omega/dk$ respectively), it gives an insight of the geometry and interactions of the system containing the wave and it explicitly shows the possible frequency values for a range of $\mathbf{k}$ (inside the Brillouin Zone of a crystal, for example). The dispersion relation for electromagnetic oscillations is given by Eq. 2.26, for photons ε is for the surrounding medium or the vaccuum permitivity ($\varepsilon_0 = 1$ in CGS units), for LSP in metallic nanoparticles ε is given in the form of Eq. 2.17.

$$\varepsilon\omega^2 = c^2k^2 \tag{2.26}$$

When matter waves such as plasmons interact with photons they may couple forming states that are a mixture of the two particles, namely *plasmon-polaritons*. This combination can be appreciated in the dispersion relation of the compound system that follows neither the isolated plasmon, nor the photon behaviour. One may measure the light-matter interaction through the Rabi frequency (Ω_R), that describes the periodic behaviour of a two-level system interacting with an oscillatory electro-magnetic field. In the plasmon-polariton dispersion relation, $2\Omega_R$ is the frequency distance between the two bands at the k-value where the isolated dispersions cross, see figure 3. Different light-matter coupling regimes may be determined by how the Rabi

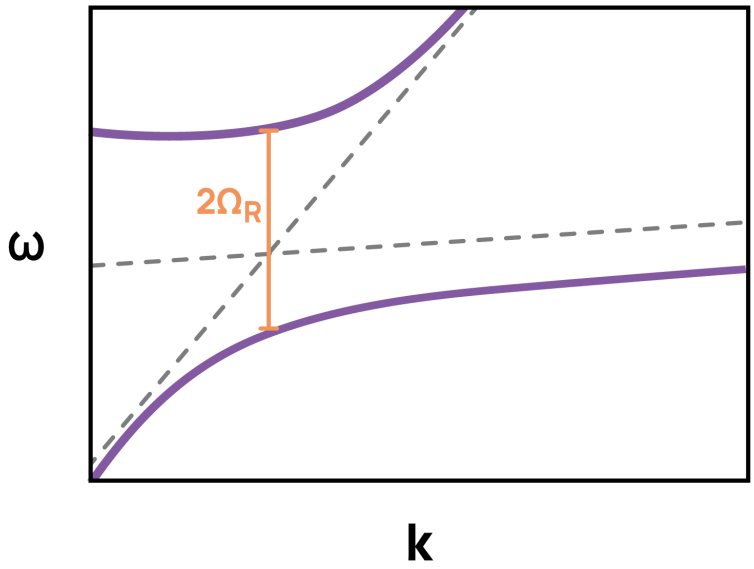

Figure 3 – Example of a dispersion relation for a plasmonic material with light-matter coupling. The dashed lines represent the dispersion relation for the photons (larger angle with the horizontal) and plasmons (smaller angle) when isolated. The coupled relation is the solid purple line. The Rabi splitting (Ω_R) is indicated.

frequency relates to the excitation frequency (ω_p in our case), so it is convenient to define η as the normalized coupling strength:

$$\eta = \frac{\Omega_R}{\omega_p} \tag{2.27}$$

with $\eta = 0$ for the uncoupled regime, $0.1 \leq \eta \leq 1.0$ defines the *ultrastrong coupling regime*, while $\eta \geq 1.0$ defines the *deepstrong coupling regime*.

3 MATERIALS AND METHODS

3.1 MoS_2: a benchmark 2D semiconductor

2D crystals have been studied theoretically since the 1940's (WALLACE, 1947), but it wasn't until the first half of the 2000's that the scientific community found the experimental value of these materials, when Novoselov *et al.*, in Nobel prize winning work(NOBELPRIZE.ORG, 2023), was able to separate monolayer graphene from mineral graphite through the technique of mechanical exfoliation(NOVOSELOV *et al.*, 2004) (see Sec. 3.1.1.1). This opened up the field of 2D crystals to experimental work, that soon found some favourite materials: graphene is the all-time favourite, with its semi-metal behaviour; hexagonal boron nitride (h-BN) quickly established itself as the go-to 2D insulator, broadly used as a protective cover for 2D devices(HOLLER *et al.*, 2019). During the exploration of new materials, the scientific community often takes advantage of having a consonance on which material to investigate first. Having a benchmark material is useful because this way the scientific community promptly generates literature used to understand a whole family of materials. The field of semiconductors also took advantage of this and quickly found Transition Metal Dichalcogenides (TMDCs) to be a great family of 2D semiconductors to explore, with MoS_2 being the most broadly reported on(MANZELI *et al.*, 2017).

Probably the greatest motivation behind the exploration of 2D semiconductors is the search for next generation electronic devices (present since the first experimental report(NOVOSELOV *et al.*, 2004)). With silicon-based transistors (the computers' building block) reaching their size limit of a few nanometers, 2D semiconductors gained momentum in the research community for the possibility of application in vertical heterojunction transistors beyond the Si industrial limit. Reports on this front have been published(GADELHA *et al.*, 2019; NOVOSELOV *et al.*, 2004). Other applications of these materials include sensors(MANZELI *et al.*, 2017) and light harvesting devices(JARIWALA *et al.*, 2017).

Transition Metal Dichalcogenides (TMDCs) are materials of the form MX_2 with M being a transition metal (typically W or Mo) and X being a chalcogenide (most commonly S, Se and Te). The metal is sandwiched between the two chalcogenides connected by covalent bonds (see Fig. 4). TMDCs in the layered crystal phase is easily found in nature, Molybdenite (MoS_2), for example, has been reported in all continents (including Antarctica!)(FOSSILIENATLAS,). This family of materials has a hexagonal crystalline lattice and a semiconducting behaviour, with electronic gap in the order of 1-2 eV, their monolayers have a direct bandgap (unlike their layered

counterparts)(MANZELI *et al.*, 2017; CHAVES *et al.*, 2020). MoS_2 has an indirect bandgap of 1.29 eV in bulk form, when in a single layer it transitions to a direct bandgap of 1.9 ev(MAK *et al.*, 2010) (Fig. 4).This family has also interesting optical properties, with absorption in the visible range and excitonic behaviour, making them even more interesting for the community because of their application in optoelectronic devices (such as phototransistors and photodetectors) promising(MANZELI *et al.*, 2017).

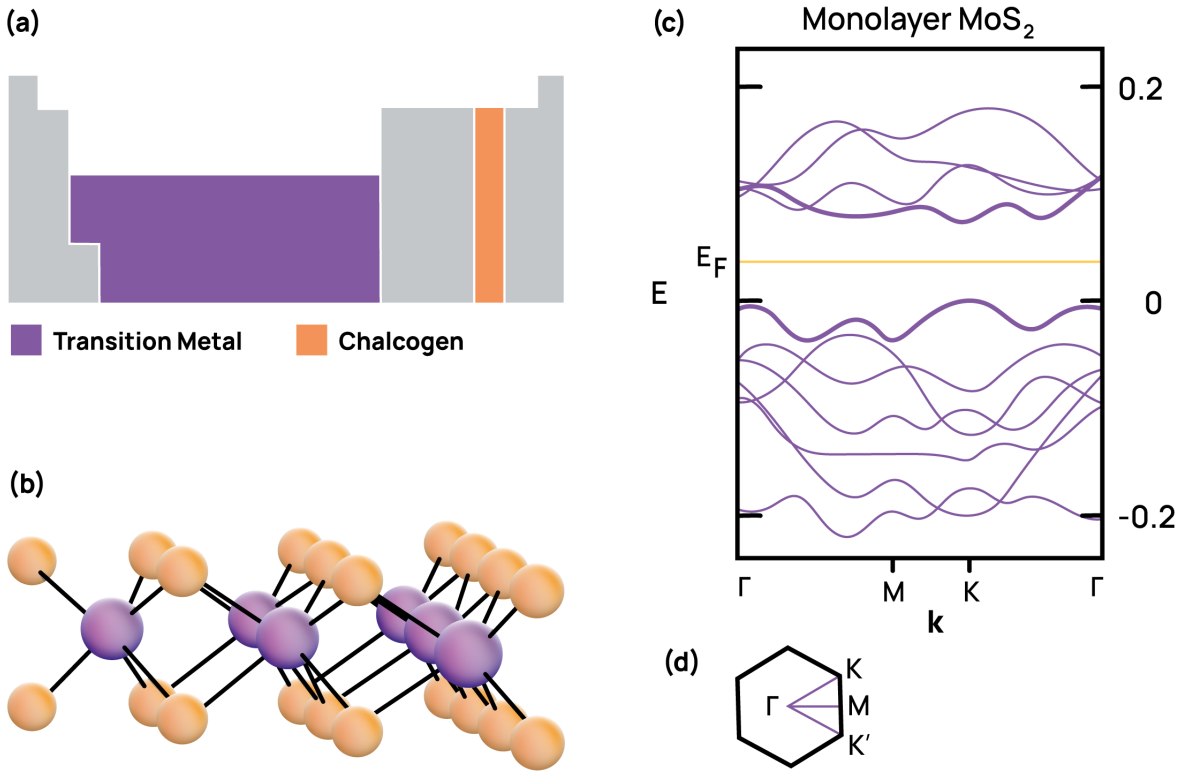

Figure 4 – (a) Shows a simplified representation of the periodic table indicating the composition of TMDCs, purple indicates the position of Transition Metals in the periodic table and orange indicates Chalcogens (group 16 elements). (b) The crystal structure of a single MoS_2 sheet, purple are the transition metal atoms (molybdenum) and orange the chalcogen (sulfur). (c) Electronic band structure from monolayer MoS_2, the vertical axis is the energy and the horizontal is the **k**-vector, with high symmetry points marked. The valence and conduction band extremes are represented by thick purple lines, notice the direct band gap at the K point. The Fermi energy is marked inside the band gap, indicating the semiconductor behaviour of the material. (d) Brillouin Zone (BZ) for the hexagonal lattice with high symmetry point marked.

For each specific application, semiconductors with specific properties (like electronic bandgap and Fermi energy values) are needed. In Si-based devices these properties are manipulated through doping mechanisms(COLLINS; CARLSON, 1957; GUO *et al.*, 1997). For 2D semiconductors a broad range of manipulation techniques have been applied in search for

practical ”knobs” to tune the electronic properties, including number of layers, doping, applied pressure and strain(CHAVES *et al.*, 2020; KIM *et al.*, 2021; PENG *et al.*, 2020; CONLEY *et al.*, 2013; JOHN *et al.*, 2020; QUEREDA *et al.*, 2017). For the work reported in this thesis, we explore two knobs: local uniaxial (vertical) pressure (Chap. 4); and plasmonic substrate interaction (Chap. 5).

3.1.1 Sample preparation: MoS_2

In 2004, Novoselov, Geim and collaborators used mechanical exfoliation to publish the first experimental observation of 2D crystals, namely monolayer graphene(NOVOSELOV *et al.*, 2004). The next year they published a paper named ”Two-dimensional atomic crystals”, where they used the previously reported technique to prepare multiple other few to monolayer crystals (including MoS_2)(NOVOSELOV *et al.*, 2005). With this, they established the experimental stepping-stones to isolate atomically thin samples from layered minerals. The importance of their work rendered them the Nobel Prize in Physics of 2010(NOBELPRIZE.ORG, 2023).

3.1.1.1 Exfoliation

To prepare 2D MoS_2, we attached a mineral flake of the bulk material (HQ Graphene) to a common Scotch Magic Tape, this tape was labelled “tape 0”. We then attached “tape 0” to a new piece of tape and peeled them, this new tape was labelled “tape 1” (see a picture in Fig. 5(a)). We repeated this step one more time with a new piece of tape, producing “tape 2” (Fig. 5(b,c)). A clean rectangular cut of Polydimethylsiloxane (PDMS) was made to contact “tape 2”, we used the backside of tweezers to gently apply pressure to the back of the PDMS (in an “up-and-down” motion, Fig. 5(d)), and finally the PDMS was removed from the tape with the MoS_2 flakes (Fig. 5(e)). The PDMS was placed under an optical microscope and we used x10, x20 and x50 objectives to scan it in search for few to monolayer MoS_2, taking notes on their positions (x and y mm from a chosen corner of the PDMS). After this step we have a rectangular PDMS with thin MoS_2 in known places.

It is important to note that, even though this is a well reproduced technique, there is a lot of art to it. The tape number (i.e. the number of times one glues a clean tape to the previous one with MoS_2) from which to extract the flakes may vary depending on the original mineral size and on the type of tape used. Also, the pressure on the back of the PDMS is an optional step, it was something I found to work better for me (based on trial and error), but the amount of pressure

and movement is very arbitrary, given that it is completely manual work. Also, finding few to monolayers in PDMS (even with 100x objective) is something that takes time (from 20 min to 2-3 hours!) and demands well trained eyes, given that the contrast is nearly none when compared to flakes on SiO_2 (see Fig. 5(f,g)). If someone is trying to reproduce the exfoliation for the first time, they might need many attempts to generate a good sample, experimenting themselves slight changes in the procedures - maybe there's no need to apply pressure to the PDMS, or the 1st flake is too thick and one will only get monolayers by using "tape 5", even the speed in which one removes the contact with the tape can change the final flakes. Taking detailed notes on every attempt made helped me establish the specifications presented here.

3.1.1.2 Transference: dry-stamp technique

Once we have a good MoS_2 flake (area of tens of μm^2 or larger and mono to few layers), we use the PDMS as a stamp to transfer the MoS_2 to the target substrate (either the pre-patterned gold pads for Chap. 4 or the gold nanoparticles supercrystal for Chap. 5), this is done in a similar way to the one reported by Castellano-Gomez in ref. (CASTELLANOS-GOMEZ *et al.*, 2014). The first sample was prepared by Dr. Andreij Gadelha, a collaborator from the group of Prof. Leonardo Campus at Universidade Federal de Minas Gerais (UFMG). The collaborating group was kind enough to host me for a couple of weeks in 2019, during which I was trained in the techniques described in this section, I used this knowledge to prepare the second sample.

The transfer stage is composed of two xyz micropositioners: one to hold a glass slide with the PDMS facing down and one to hold the heating plate and the target substrate. They are placed under an optical microscope and used to align the previously exfoliated flake (from Sec. 3.1.1.1) and the target substrate. A contact temperature ($T_0 = 85$ºC) is set, the PDMS with the MoS_2 and the substrate are approached and made to touch, we wait some time (15 min) to assure temperature equilibrium, then a new target temperature ($T_f = 50$ºC) is set, the contact is then lifted. Temperature expansion and/or contraction is used when very slow and precise z movements were desired. A vacuum pump is connected to the heating plate used as the substrate holder (with a small hole right underneath the target substrate), the vacuum assures there is no drift during the procedure and avoids the whole substrate being picked-up by the PDMS stamp. A scheme of this procedure is presented in Fig. 6 (c-e).

Like in the previous section, some expertise is required here. A scientist new to this technique may play around with some parameters to optimize the procedure, such parameters

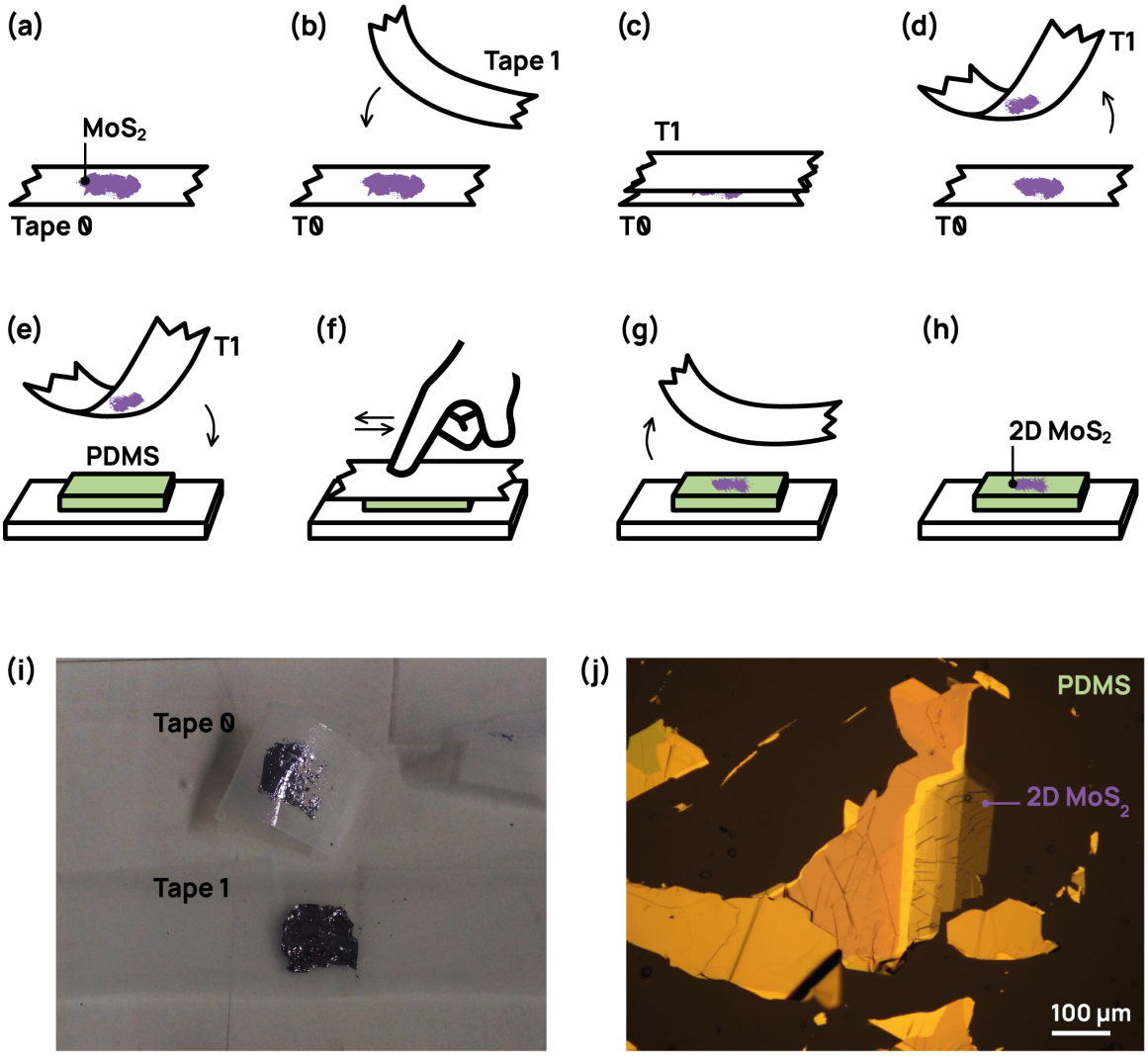

Figure 5 – Step-by-step of the exfoliation procedure: (a) shows the mineral MoS_2 in a scotch tape (T0); (b) and (c) a clean second tape (T1) is made to contact (T0); (d) when the contact between the two tapes is removed some of the material is tranfered to T1; (e) T1 is then made to contact a clean slab of PDMS polymer; (f) pressure is delicately applied to the back of the tape with the finger (in Nitrile glove); (g) tape 1 is removed from the PDMS; and (h) thin 2D MoS_2 stays in the polymer. (i) A picture of Tape 0 and Tape 1. (j) Microscopic reflectance image of MoS_2 in PDMS with a thin region (three-layers) marked.

include: the temperature values (we had successful transference with T_0 from 80 up to 97ºC, and T_f from 39 to 50ºC), the time the contact is kept (we used from 10 to 17 min), the velocity in which the contact is made and removed can also affect the outcome.

3.2 Metallic nanoparticles (NPs)

Particles that have all three dimensions falling bellow the hundreds of nanometers scale (typically <100 nm) are named NPs. They can be naturally occurring, and long before

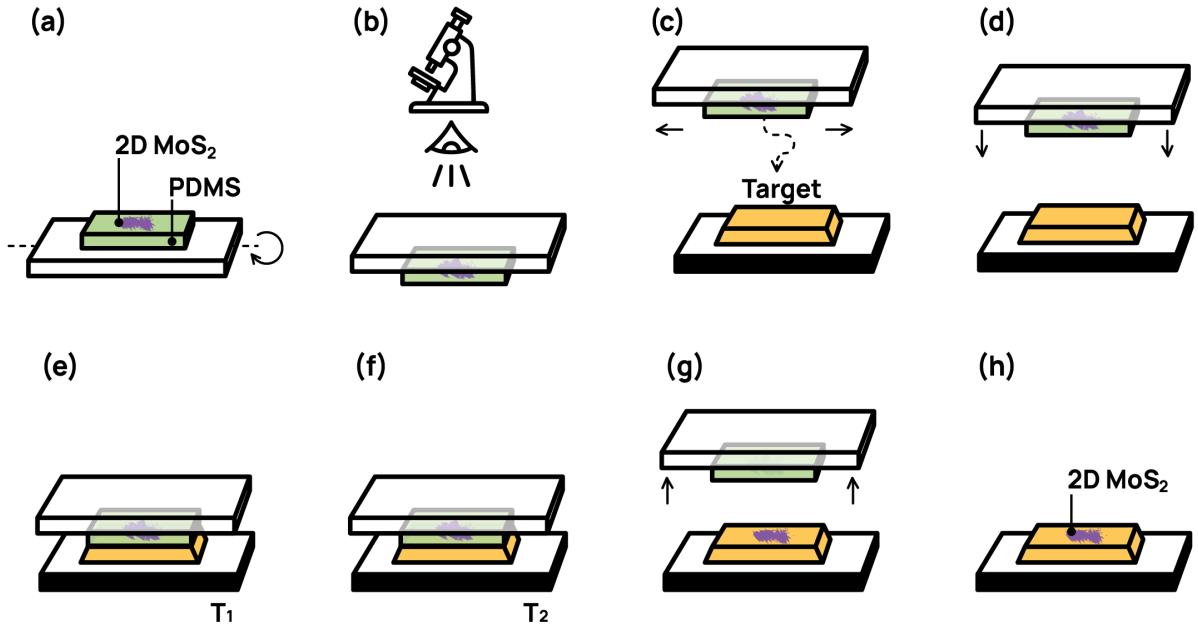

Figure 6 – Step-by-step of the transference procedure: (a) shows the thin MoS_2 on PDMS (see figure 5(h)); (b) the slide is flipped and positioned in the transfer stage, where the optical microscope allows us to see the sample trough the glass and PDMS; (c) with the target substrate placed in the bottom of the transfer stage, micropositioners are used to align and aproximate the MoS_2 and the substrate; (d) once aligned the PDMS stamp contacts the target substrate with (e) temperature T1; (f) temperature is changed to T2 and contact is maintained for thermal equilibrium to take place; (g) the PDMS stamp is lifted and (h) the thin MoS_2 is left in the target substrate.

the advance of modern science (400 years B.C. and earlier) nanoparticles were already used by humans as pigments for porcelain and glass in ancient China, Egypt and in the Roman empire (as in the famous Lycurgus cup for example, with red transmitted colour and green reflected), soluble Au NPs were also used in medicine in the middle ages (for the diagnoses of syphilis, for example)(DANIEL; ASTRUC, 2003). In modern times, the number of ways to use NPs - specially the most stable Au NPs - is still growing, with recent applications in cancer treatment, biosensing, solar energy conversion, catalysis, field enhancing substrates and more(ABERASTURI *et al.*, 2015; MUELLER *et al.*, 2021). In our work, we explore the plasmonic properties of Au NPs (see Sec. 2.5), specially using supercrystals as optically active substrates.

3.2.1 Sample preparation: Supercrystals

In 2020, the group of Prof. Reich published a paper entitled “Deep strong light–matter coupling in plasmonic nanoparticle crystals”(MUELLER *et al.*, 2020), where they showed experimentally that supercrystals of Au NPs (≥30 nm) have the largest ever recorded light-matter

interaction, all on ambient conditions. In September 2021, I started my sandwich experience with the above-mentioned group hosting me at Freie Universität Berlin. While abroad, I was lucky to be trained (alongside MSc. Arseniy Epshin) in first-hand by Dr. Florian Shulz, the researcher at Universität Hamburg responsible for producing the samples in the mentioned paper (further Ref. (SCHULZ *et al.*, 2017)). In this section, I will explain the step-by-step of this procedure, with the intent of having a guide for the researchers who wants to produce their own gold nanoparticle supercrystals. Bringing this technique back to my home Brazil is not only a demand from the CAPES grant that took me abroad, but is also my scientific duty of spreading knowledge - with that in mind, **I added a version of the procedures in PORTUGUESE in the appendix B**.

For this procedure we use: ultra pure Milli-Q water ($18.2 M\Omega.cm$), Tetrachloroauric(III) acid ($HAuCl_4 \cdot 3H_2O$) (≥99.9%), cetrimonium bromide (CTAB) (≥98%), sodium borohydride ($NaBH_4$) (≥98%), Cetrimonium chloride (CTAC) (≥ 98%), L-ascorbic acid (AA) (≥99.0%), thiol-terminated polystyrene (PSSH) (with a variety of molar masses, all from Polymer Source - Canada), tetrahydrofuran (THF) (≥99.5%), toluene (≥99.5%), ethanol (≥96%), diethylene glycol (DEG), nitric acid (HNO_3) and hydrochloric acid (HCl).

It is important to note that any impurity in the growth may lead to the irregular formation of clusters and nanoparticles, so it is essential to use Milli-Q water throughout the whole procedure. The glassware used to handle the gold solutions should be used only for this, and cleaned with Aqua Regia between consecutive uses. To prepare Aqua Regia, the safety coordinator of the chemistry lab, Dr. Katayoun Hubmann, mixed nitric acid and hydrochloric acid in the ratio of 1:3 - one must be careful with this substance for it has very strong corrosive power - it was always handled with protective gear inside a fumehood given the liberation of toxic gases(PRINCETON, 2023). To estimate the size of the particles in the intermediary solutions, one may use absorbance (UV/Vis) at 450 nm, as described by Haiss *et al.*(HAISS *et al.*, 2007).

In order to facilitate most of the procedures, we prepared the robust aqueous solutions beforehand, in their most concentrated form, with proper storage - $HAuCl_4$ (0.5 mM, 500 mL), stored in dark, closed container in the refrigerator; CTAB (200 mM, 50 mL, 3.64 g), stored in closed container in the shelf; CTAC (200 mM, 100 mL, 6.39 g), stored in closed container in the shelf. If the CTAB (or CTAC) solution appeared to have crystallized we would sonicate it with a bath sonicator until it was completely solved again. This way, the only solutions we had to worry about during the NPs growth were the less concentrated ones (that were easily produced by dilution) and the unstable solutions ($NaBH_4$, AA).

3.2.1.1 Au Clusters

In this step, we produce small (∼2 nm) gold clusters by reducing (with $NaBH_4$) the gold in $HAuCl_4$ in a CTAB-rich environment. The CTAB molecules encapsulate and stabilize the metallic gold.

Using a magnetic stir at 800 rpm, we mixed CTAB (200 mM, 5 mL) and $HAuCl_4$ (0.5 mM, 5 mL). Freshly prepared aqueous $NaBH_4$ (10 mM, 0.6 mL from 4 mg in 10.5 mL) was added with a pipette via one-shot injection in the stirring (800 rpm) gold-CTAB solution (Fig. 7(a)), the solution turned brown. After two minutes, the stir was turned off and the solution was kept open and undisturbed for 3 hours in the hood to assure the conversion of the sodium barohydride (there's H_2 forming). The mixture was done in a water bath at 27ºC. With this, we produced CTAB capped Au clusters (<5 nm). This solution can be kept in the refrigerator for future use, but long term storage (longer than a couple of months) is not recommended.

3.2.1.2 First generation nanospheres (∼ 10nm)

In this step, we change the capping agent to CTAC and we enlarge the Au clusters by reducing $HAuCl_4$ (this time with the mild agent AA) onto the surface of the previously formed Au clusters. If the nanoparticles were left to be enlarged in CTAB solution, they would evolve into nanorods, CTAC ensures the spherical shape. The excess CTAB is washed.

In a volumetric cylinder, we mixed 20 mL of CTAC (200 mM) with 15 mL of AA (100 mM, from 0.89 g in 50 mL), 500 µL of the cluster solution from Sec. 3.2.1.1 was added and the mixture was bath-sonicated for 5 minutes, the solution was put in a beaker and stirred at 600 rpm. 20 mL of $HAuCl_4$ (0.5 mM) was added to the stirring (600 rpm) mixture via one-shot injection from a volumetric pipette while pressing the balloon, Fig. 7(b). The solution turned red promptly. The stir was turned off and the solution was kept undisturbed for 20 min. To tune the NPs' size, one may reduce the volume of the cluster solution used here leading to larger first generation nanoparticles.

To clean the solution from CTAB and to make the nanoparticles' size distribution narrower, we placed the solution in eppendorfs (24x2 mL - larger eppendorfs can be used if one has access to a large centrifuge) and centrifuged it for 30 min at 20.000 g (15ºC). If the solution is still homogeneously coloured afterwards, centrifuge it for longer periods. The supernatant was removed from the eppendorfs (the solution placed in only two 2 mL eppendorfs now) and

Milli-Q water (2 mL, 1 mL per eppendorf) was added. A second and a third centrifugation took place (20 min, 20.000 g), with the supernatant being removed and replaced with CTAC (20 mM, 2 mL) two times. Extra washing steps will only improve the quality of the final concentrated solution. The solution was diluted in 10 mL CTAC (20 mM) and stored in the refrigerator (it can be stored like this for up to 6 months).

3.2.1.3 Second generation nanospheres (> 20nm)

First generation nanoparticles are used as seeds and the slow reduction of $HAuCl_4$ is used to homogeneously grow the particles, with CTAC as capping agent. Centrifugation is used to clean the solution, assuring a narrow distribution of the nanospheres' diameters. Further enlargement of the particles is possible by using second (or higher) generation particles as seeds.

A clean beaker was placed in water bath at 27ºC with a magnetic stir at 400 rpm. In it we added 20 mL of CTAC (100 mM), 500 µL of seeds (1st generation nanospheres from Sec. 3.2.1.2) and 130 µL of fresh AA (100 mM). Reducing the volume of seeds reduces the number of NPs and increases the size of the next generation nanospheres. We used a syringe pump (in a 20 mL/h flow) to add 20 mL of $HAuCl_4$ (0.5 mM) in a drop-wise manner to the stirring (400 rpm) mixture, for this we used a clean plastic syringe with a teflon extension - the use of metallic parts to manipulate $HAuCl_4$ is not recommended, given that they will reduce the gold that should only be reduced in the surface of the seeds.

The solution was cleaned by being placed in eppendorfs and centrifugated (see table 4) three times, with the supernatant replaced by 2 mL of Milli-Q water on each step - the concentration of CTAC should not fall below 5 mM, if needed add 2 mL of CTAC (20 mM) instead of water. Extra washing steps can be done depending on the quality of the solution and on the care of the researcher. The specifics for the centrifugation (table 4) are dependent on the particle size, this can be an educated guess by the experienced researcher or estimated from the UV/Vis spectrum of the solution(HAISS *et al.*, 2007). To store this solution, dissolve the final pellet in 10 mL CTAC (20 mM) and keep it in a refrigerator, concentrate it (by centrifugation) before continuing the procedures.

3.2.1.4 Polymer functionalization of nanoparticles

In this section, the thiol end of the PSSH reacts with the Au surface functionalizing it with a polymer, this stabilizes the particles, preventing any contact with their metallic surfaces

Table 1 – Centrifugation and PSSH parameters for each NP size

Size Generation (nm)	Acceleration (g)	T1 (min)	T2 (min)	PSSH size
<20	20.000	45	30	2k-PSSH
20	10.000	30	20	2k-PSSH
30	7.000	30	15	2k-PSSH
40	5.000	30	12	5k-PSSH
50	2.500	30	10	12k-PSSH
70	2.500	30	10	12k-PSSH

Specifications for centrifugation of Au NPs in solution in relation to approximate NP diameter (Sec. 3.2.1.3), for each size generation the acceleration should be used for T1 in the first centrifugation and for T2 for any further centrifugation. Recommended PSSH size (according to the average molar weight - Wn) to functionalize NPs for each diameter value (Sec. 3.2.1.4)

(see Fig. 7(c)). The new solution is toluene-based, we clean it by centrifugation with supernatant replacement and by phase separation with water and ethanol - removing all excess PSSH and any water or alcohol soluble impurities. The product is a concentrated, stable toluene solution of polymer-capped Au NPs.

We chose the size of PSSH (2k, 5k or 12k, in reference to their average molar weight, Mn) according to table 4, a THF solution of PSSH (6 mL, 0.5 mM) was prepared in a clean round-bottomed flask with a magnetic stirrer at 700 rpm. The Au NPs from Sec. 3.2.1.3 (concentrated to $\sim$ 500 µL) were added from a precision pipette in a drop-wise manner directly into the stirring liquid. The mixture was left with 700 rpm overnight. The next morning, the stirring was stopped, the magnetic stir was removed from the round bottom flask, and it was taken to the rotary evaporator to remove the THF and water, Fig. 7(e). The rotary evaporator was set to 250 rpm, 40ºC, reaching 11 mbar in a step-wise manner, it was left for 30 minutes (it may be necessary to leave it for longer). The solvents were cleaned from the evaporator's condensation chamber. The nanoparticles left in the glass of the flask were dissolved in 1 mL toluene and placed in an eppendorf, extra 500 µL of toluene were used to clean the traces of NPs left in the round-bottomed flask and it was placed in the same eppendorf.

The NP-toluene solution was centrifuged following the strength and time (T1) in table 4 for 4 times, each time the supernatant was replaced by 1 mL toluene - this removes excess PSSH and narrows the NPs size distribution. In a clean, thin, glass cylinder with a lid we mixed the Au NP toluene solution with 1 mL of Milli-Q and 1 mL of ethanol. The cylinder was closed and shaken by hand, it was then left on the counter until the phases separated, Fig. 7(f). We then used a clean, thin, long nozzle glass pipette to remove the transparent water and ethanol based phase. This phase separation was repeated three more times (for a total of 4 times, adding more

water and ethanol before each separation). A final centrifugation step can be done to increase the concentration of the (pink to brown coloured) toluene-based PSSH-capped gold nanospheres. The solution is stable and can be stored indefinitely in a glass with toluene resistant lid and parafilm, in a refrigerator.

3.2.1.5 Superstructure crystallization

Now, we slowly evaporate the toluene on top of a (DEG) liquid interface, generating by self-assembly a crystalline structure made out of the nanoparticles, the supercrystals. When the toluene is evaporated, the supercrystals are left floating in DEG, the liquid DEG subphase is drained until the supercrystals are exposed to a glass substrate that was previously submerged. The supercrystals are attached to the glass slide, residual toluene and DEG are removed from the sample by evaporation in vacuum.

A small piece of clean glass slide (the target substrate) was placed in the bottom of a Teflon well (∼1 cm in diameter), the substrate was submerged in DEG (300 µL), the liquid covered ∼60% of the well (careful not to leave any bubles under the substrate). A 1:3 mixture of Au NPs (from Sec. 3.2.1.4) and toluene was pipetted on top of the DEG and the well was covered with a thin glass slide. The well was left undisturbed in the fumehood for two days for the complete evaporation of toluene, a thin reflective film could be seen on the surface of the DEG subphase. The DEG was drained with a syringe through a 1 mM thick hole in the bottom of the Teflon well, leaving the supercrystals attached to the target substrate. The surfaces of the glass were delicately dried with paper (careful not to touch the supercrystals), then the substrate with the supercrystals was taken to a vacuum chamber of 1 mbar for 3 hours to completely dry the sample from toluene and DEG. A scheme of the well is represented in figure 7(f), the supercrystals are depicted in Fig. 15.

One can control the speed of the toluene evaporation by changing the volume of air in the well (using more DEG), more air equals faster evaporation; and/or by adding a weight on top of the cover slid (slower evaporation) or not completely covering the well (faster evaporation). Fast evaporation leads to thinner supercrystal samples. Increasing the volume of the NPs-toluene solution increases the average thickness of the generated supercrystals. Different substrates may be submerged in DEG, and it is also possible to fish the floating supercrystals before draining the subphase (this “fishing” was used for small TEM grids), one could also use a pipette to drain the DEG.

3.3 Atomic Force Microscopy (AFM) and Conductive-AFM (CAFM)

AFM consists of using a sharp tip (radius $\leq$ 30nm) interacting with the sample's surface to map it, generating a topography image. The tip is placed in a tip-holder and a piezo-stage controls the xyz position of the sample under the tip, the stage approaches the sample until the set-point interaction with the tip (measured by the tip bending), a feedback loop adjusts the sample height while the image is being generated. To generate the image, a scanning process of the sample takes place with measurements being taken point-by-point and joint by the computer at the end of the scan. The most important and precise measurement acquired by this technique is the topography image, with height precision in the order of one Angstrom (Å $= 10^{-10}$m). The topography measurements presented here were made in the "tapping" (or "alternate-contact") mode, the AFM oscillates the tip near its resonance and measures the tip-sample interaction via variations in the oscillation amplitude, this avoids the risk of damaging the sample and the tip during the scanning process. AFM is a well established technique and it's the most reliable way of determining the number of layers in 2D crystals together with Raman spectroscopy(OTTAVIANO *et al.*, 2017). By a standard calibration procedure, the AFM can calculate the cantilever's force constant, this can be used to have very precise control over the force exerted by the tip. In this chapter we used the AFM MFP-3D from Asylum Research, from the Advanced Microscopy Laboratory (Laboratório de Microscopia Avançada - LMA) at the physics department of Universidade Federal do Ceará (UFC).

The AFM technique has many modifications that allow different kinds of interaction with the sample, one interesting modification that allows the investigation of the sample via electrical current measurements is the *Conductive Atomic Force Microscopy (CAFM)*(QUEREDA *et al.*, 2017). In CAFM, a metallic tip (Si covered with PtIr, NanoWorld EFM tips for our experimental setup) with a special tip holder is used (ORCA in our case), this tip holder allows the microscope to apply a voltage difference between the tip and the sample holder (that makes an electrical contact with the sample substrate via a gold clamp), the instrument is able to measure the current passed through the sample (up to 20nA for the ORCA used in our experiment). This complex way of measuring I-V curves is justified by its precision and the local nature of the tip-sample contact, not present in more common techniques, allowing the vertical measurements of 2D MoS_2 conductivity in positions of different layer numbers. Measuring the I-V curves with an AFM also has the advantage of being able to precisely control the contact force between the tip and the sample, making it possible to investigate the effect of local strain in vertical

metal-sample-metal devices.

3.4 Micro-absorbance setup

To measure reflectance, transmittance and, thus, absorbance we used the optical setup from AG Reich group at Freie Universität Berlin (FU-Berlin). The setup consists of: a white source super-continuum laser (NKT Photonics - FIU15); an ND filter (Thor Labs) that dims the beam; a light collector for safety; two beam splitters (Thor Labs), one for reflectance measurements and one for the camera; an optical microscope (Olympus, IX71) with a 100x objective lens (Leica HCX PL Fluotar); a white light source was used for sample illumination during the positioning; a motorized xy stage with a joystick controller to change the positions of interest in the sample; the transmitted light was capture by another 100x objective lens (Olympus MPlan FL N BD); two detectors, one for IR light (Avantes AvaSpec NIR512) and one for visible light (Avantes AvaSpec 3648); optical fiber cables guided the light beam from the laser source to the optical path, and guided the reflected (or transmitted) beam to the detectors; a computer with the Avantes and the camera softwares was used to produce the images and spectra; the whole apparatus was set on top of an optical table with pressurized air used to damp oscillations.

The beam started as a bright white light that left the super-continuum laser via an optical cable, it left the optical cable and met the ND filter that dims its power and prevents the burning of the sample. The portion of the light that was reflected by the ND filter went in the properly positioned light collector to avoid damage to people and other equipment in the lab. After passing through the filter, the beam went through the first beam splitter and reflected on the second beam splitter, it then entered the microscope and the first objective 100x lens, hitting the properly focused sample at the precise location to be measured. After interacting with the sample the beam had two possible paths: the reflected and the transmitted. The transmitted light went through the second 100x objective, inside an optical cable that was directly connected to one of the detectors. The reflected light went back in the first objective, reflected on the second beam splitter and reflected again in the first beam splitter, the beam then entered an optical cable that was directly connected to one of the detectors. The light from the microscope's illumination and a portion of the beam were reflected by the sample, went in the reflectance objective, through the second beam splitter and into the camera. A scheme of the micro-absorbance setup is given in figure 8 (a).

To get the experimental reflectance spectra, we first had to do the calibration procedure

by measuring the dark spectra (measurement with the illumination and laser beam turned off) and the reference spectra of the beam reflected by a silver mirror (Thor Labs, PF10-03-P01) with the Avantes software, this was done for both the spectrometers, one at a time. We then placed our sample in the microscope with its illumination and the camera turned on, and used the microscope's z micropositioner to focus. With the joystick controller, we used the motorized xy stage to look for the region in the sample that we wanted to measure, once we had the region we turned on the super-continuum laser, turned off the microscope's illumination, and focused the beam (slightly different than the image focus). We then connected the optical cable with the reflected beam to the spectrometer and measured the reflectance spectra for visible light, followed by the spectra in infra-red (IR) radiation, each with the corresponding detector. We would afterwards turn the illumination back on, change to a different point of interest in the sample and take new measurements.

Once we had the reflectance spectra it was time to measure the transmittance. For this, procedures very similar to the ones described above were followed, with the difference that the calibration was done with the reference being a region with only the glass substrate (without any samples on top) and the optical cable connected to the spectrometer was the cable with the transmitted beam. For the transmittance calibrations, we used glass regions near the spots to be measured, with multiple calibrations in the same sample - due to the different focal planes for different spots interfering in the reference spectra. The reflectance (R) and transmittance (T) spectra were calculated by the software by the equation 3.1. Having the reflectance and transmittance spectra, we could calculate the absorption (A) spectra using the formula $A = 100\% - T - R$. Examples of R, T and A are given in figure 8 (b).

$$M = 100\% \times \frac{Counts_{measurement} - Counts_{dark}}{Counts_{reference} - Counts_{dark}} \tag{3.1}$$

with M being the measured spectra (R or T), and $Counts$ being the spectrometer's counts for each specified purpose.

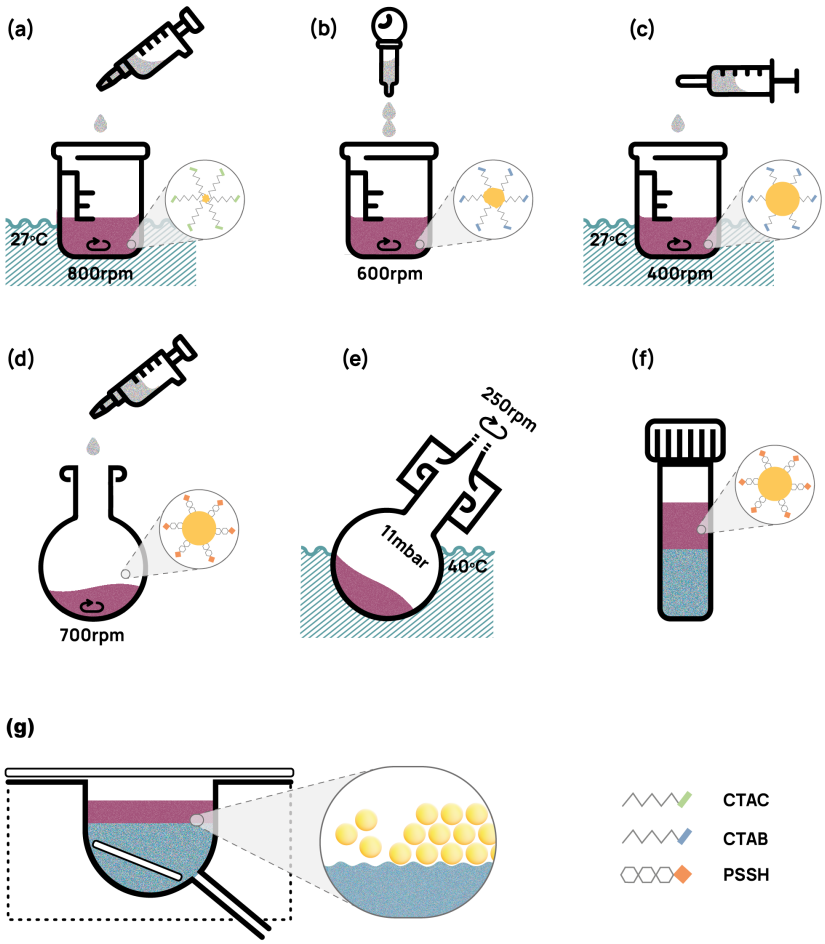

Figure 7 – Key steps in the NP growth and supercrystal formation, with zoomed representation of the particle's configuration after each represented step, note the simplistic representations of the encapsulating molecules CTAB, CTAC and PSSH in the bottom-right corner of the figure. (a) Formation of Au clusters capped with CTAB via pipette one-shot injection of $NaBH_4$ in $HAuCl_4$-CTAB solution in water bath at 27ºC and with a magnetic stir rotating at 800 rpm (Sec. 3.2.1.1). (b) Generation of first generation Au spherical nanoparticles (NPs) by pressing the balloon attached to the volumetric pipette and rapidly injecting 20 mL of $HAuCl_4$ into the clusters in CTAC solution, the magnetic stir is at 600 rpm (Sec. 3.2.1.2). (c) Second generation NPs are formed by using a syringe-pump for the dropwise addition of 20 mL $HAuCl_4$ (during 1 hour) to the 1st generation NPs in CTAC, done in a water bath at 27ºC and with the magnetic stir at 400 rpm (Sec. 3.2.1.3). Step (c) may be repeated to grow larger nanoparticles. (d) The particles are functionalized with the specific PSSH cover (check table 4) by using a pipette to dropwise add 0.5 mL of concentrated NPs in CTAC to a THF and PSSH solution stirred at 700 rpm. (e) THF and water are evaporated from the solution in a rotary evaporator at 250 rpm with a water bath of 40ºC, leaving the dry nanoparticles in the wall of the round-bottomed flask to be latter dissolved in toluene (Sec. 3.2.1.4). (f) With the PSSH functionalized NPs now dissolved in toluene, a phase separation procedure is made by mixing and shaking water and ethanol in a flask with cap, any residual molecules soluble in water or ethanol are then removed by separating the phases in the flask. (g) The final solution of PSSH capped NPs is placed on top of DEG in a Teflon well. As the toluene slowly evaporates the nanoparticles gradually self-assemble into the supercrystal in the liquid sub-phase (visible in the zoomed representation). The substrate onto which the supercrystals will attach is visible inside the DEG sub-phase, a thin glass slide is placed on top of the Teflon well to assure slow evaporation of the toluene. A thin hole (1 mM) is visible in the bottom of the well, once the toluene is completely evaporated and the supercrystals are left floating on the DEG surface a syringe is placed in the hole and the DEG is carefully removed from the bottom of the well, leaving the supercrystals in the surface of the substrate.

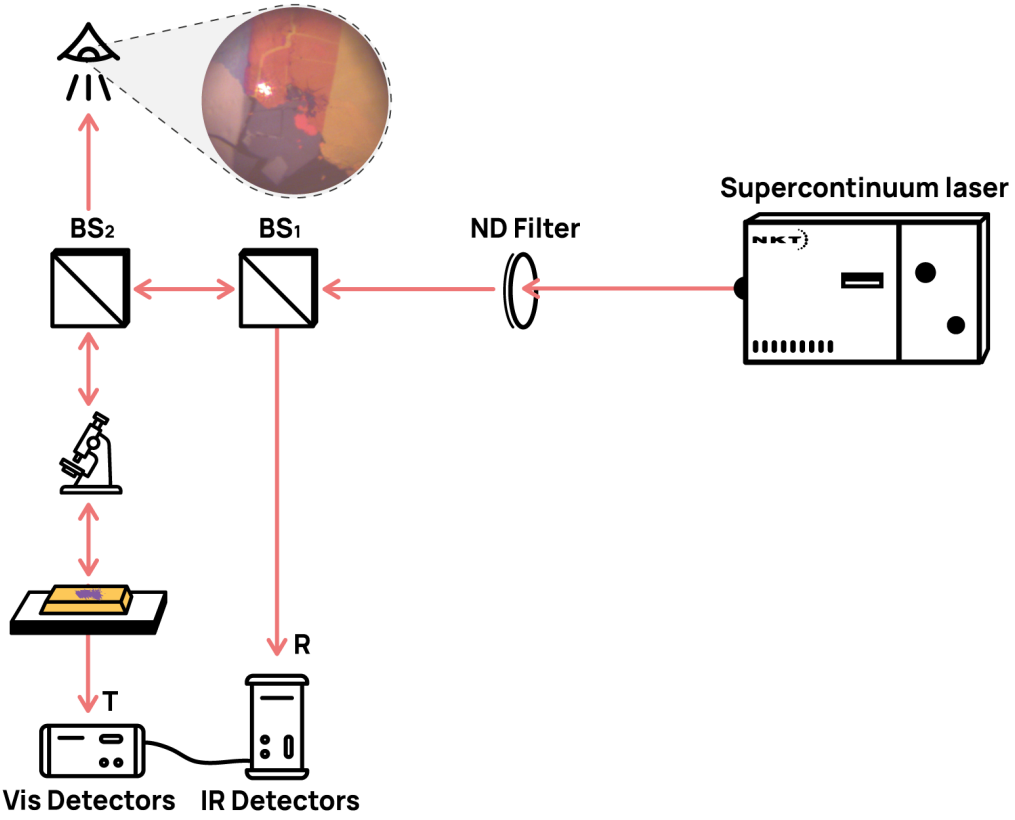

Figure 8 – The setup with the beam line and the components: super-continuum white laser, ND filter, two beam splitters (BS), the camera and the detectors. T and R indicate the final path for the reflected and transmitted beam, respectively. The inset of shows an example of the image shown by the camera (spot #3) with the illumination and the laser turned on.

4 VERTICAL POINT FORCE IN 2D MOS_2

The search for 2D materials with tunable quantum properties is been widely investigated (NOVOSELOV *et al.*, 2004; NOVOSELOV *et al.*, 2005; MANZELI *et al.*, 2017; NOVOSELOV *et al.*, 2016; CHHOWALLA *et al.*, 2013; WANG *et al.*, 2012; CHOI *et al.*, 2017; SMYTH *et al.*, 2016; TIU *et al.*, 2019; WILSON; YOFFE, 1969; DICKINSON; PAULING, 1923; HAN *et al.*, 2018; HSU *et al.*, 2017; LI *et al.*, 2018; MUELLER; MALIC, 2018; ZIBOUCHE *et al.*, 2014; SPLENDIANI *et al.*, 2010; MAK *et al.*, 2010; JIN *et al.*, 2013), as mentioned in Sec. 3.1. In 2D systems, mechanical interactions bend, strain, and apply pressure to the material, this may be used as a knob to change its physical properties (CASTRO-VILLARREAL; RUIZ-SÁNCHEZ, 2017; LEVY *et al.*, 2010; POSTORINO *et al.*, 2020; LIU *et al.*, 2018; NAYAK *et al.*, 2014; QUEREDA *et al.*, 2017; YUE *et al.*, 2012; SHI *et al.*, 2013; JOHARI; SHENOY, 2012; JOHN *et al.*, 2020; CONLEY *et al.*, 2013; HE *et al.*, 2013; ZHU *et al.*, 2013; FENG *et al.*, 2012; MANZELI *et al.*, 2015; SONG *et al.*, 2015; YANG *et al.*, 2015; QI *et al.*, 2015; WU *et al.*, 2014; SHEN *et al.*, 2016; NERI; LÓPEZ-SUÁREZ, 2018)(ZHANG *et al.*, 2017; LIU *et al.*, 2015). A semiconductor to metal transition has been observed on multilayered TMDCs under pressure (NAYAK *et al.*, 2014; SONG *et al.*, 2015). Theoretical simulations published find this change of behaviour MoS_2 to be between 10 and 15 GPa(BHATTACHARYYA; SINGH, 2012). For 1 - 8 layers MoS_2, Quereda *et al.* showed experimentally that the conductivity of vertical devices (metallic AFM tip - MoS_2 - conductive indium tin oxide (ITO) substrate) increases exponentially as the applied tip force increases(QUEREDA *et al.*, 2017), providing experimental evidence that the pressure changes the energy bandgap in MoS_2. The work described in this chapter (and published in (ARAÚJO *et al.*, 2020)) tackles the lack of quantitative information regarding how the band structure of thin MoS_2 evolves under vertically applied pressure.[1]

4.1 Objectives

The general objective of the work presented in this chapter is to **quantitatively verify the local force (strain) engineering of the bandstructure of 2D MoS_2 in vertical devices**. This is done with the specific objectives:

– Use current-voltage (I-V) measurements to understand the electric contacts in vertical

[1] The work presented in this chapter was published in: De Araujo, D. B., De Almeida, R. F., Gadelha, A. C., Rezende, N. P., Salomão, F. C. C. S., Silva, F., Campos, L. C., &Barros, E. B. (2020). **Controlling the electronic bands of a 2D semiconductor by force microscopy**. *2D Materials*, 7(4), 045029. doi.org/10.1088/2053-1583/aba5cb. The text presented here is heavily based on the published text, with some exact reproductions.

devices under different local force loads;

– Build a model that describes the devices; and
– Use the model and the I-V measurements to quantify the changes in the band energies of MoS_2 under locally applied force.

4.2 Methods

Check the Materials and Methods chapter (Chap. 3) for information on the material used and sample preparation procedures.

The thin MoS_2 (Sec. 3.1) was obtained by mechanical exfoliation (Sec. 3.1.1.1) and dry stamp technique (Sec. 3.1.1.2) was used to transfer the MoS_2 on top of the Au contacts, which was produced by electron beam lithography (EBL) and thermal metal deposition of Cr-Au (1 nm/50 nm). The sample was prepared by collaborators in Universidade Federal de Minas Gerais (UFMG).

Alternate-contact AFM topography (Sec. 3.3) is used together with Raman spectroscopy (Witec alpha 300—in Central Analítica UFC) to characterize the different regions of the MoS_2.

In Universidade Federal do Ceará (UFC) CAFM measurements of the sample were taken as described in Sec. 3.3. Thermal tuning was performed to determine the force constant of the tip before each experiment. We swept the voltage, while measuring the current, for a fixed contact force, the value of the force was changed without laterally moving the tip, and the next measurements were taken. Each I-V curve presented (figure 10) is the mean result of 10 voltage sweeps. The experimental configuration is depicted in Fig. 10(a).

We used CAFM (MFP-3D AFM from Asylum Research with ORCA tip holder) to measure the current-voltage dependence in *PtIr tip - MoS_2 - Au substrate* for different thickness of MoS_2 (from 0.9 nm 1-Layer up to 4.6 nm Few-Layers) under a wide range of force (up to 980nN).

4.3 Results and Discussion

An optical image of the sample studied is presented in figure 9(a) with a zoom showing the thin studied area. It shows a single flake of nearly 30 by 40µm with multiple regions with different number of layers on top of the gold contact.

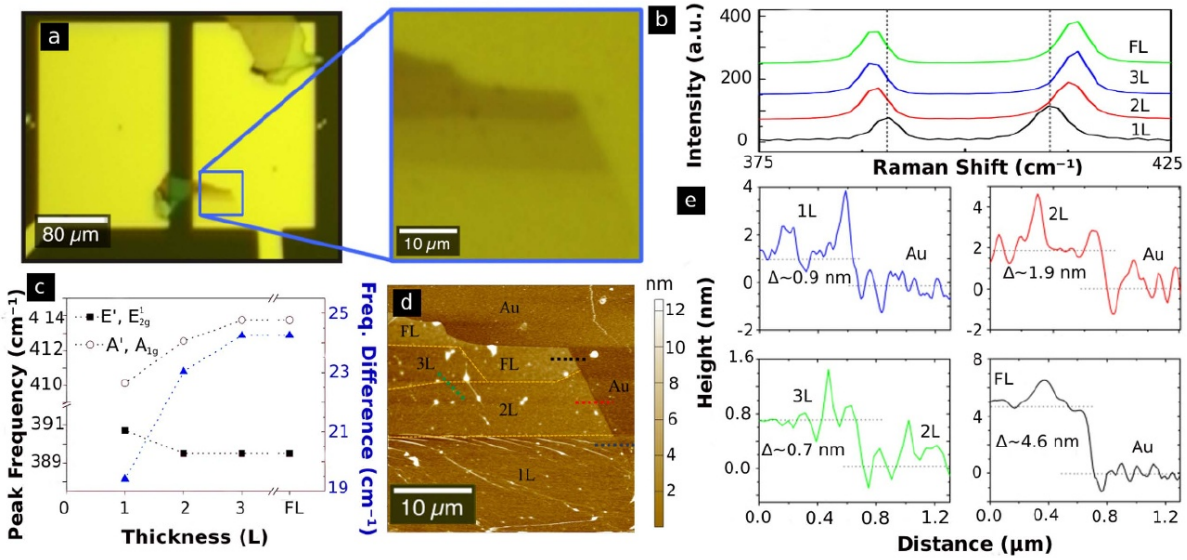

Figure 9 – (a) Optical image of the MoS_2 flake over the Au electrodes with a zoom in the studied area. (b) Raman spectrum for different thicknesses in different regions of the MoS_2 flake. (c) The A', $A_{1\,g}$ and E', $E^1{}_{2\,g}$ modes and their frequency difference as a function of layer thickness. (d) Topography image by AFM in tapping mode. (e) The topography height profiles from the line-scan (coloured dashed lines in (d)).

Raman Mapping and AFM topography determine the number of layers in each region of the MoS_2 flake, in good agreement with previously reported values(LEE *et al.*, 2010). The number of MoS_2 layers is determined by the difference in Raman frequency of the $A_{1\,g}$ and $E^1{}_{2\,g}$ (A' and E' for one-layer) peaks. Figures 9(b) and 9(c) show the Raman measurements and a plot of the peaks and their differences (from ∼19 cm^{-1} in one-layer to over 24 cm^{-1} in few-layers). AFM is used to map the topography of the sample and to confirm the number of layers in each area of the flake, figure 9(d). Figure 9(e) shows the height steps, approximately 0.9 nm per layer.

The experiment is represented in figure 10(a), the grounded tip touches the MoS_2 from the top, and a voltage is applied between the Au substrate and the ground. The tip-ground current is measured. Figures 10(b–e) show the experimental current-voltage for the different number of layers and for different applied forces. A metallic PtIr AFM tip presses the MoS_2 from the top, with the gold contact below the flake, forming the metal tip-MoS_2-Au heterostructure.

The vertical electric transport of the tip-MoS_2-Au heterostructure depends heavily on the number of layers of the thin semiconductor and the regime of applied force. For the low-force regime (not present in the one-layer MoS_2) the systems show an exponentially increasing current for positive applied bias and a saturation of the current is present in high negative bias. For MoS_2 with two-layers (2L), three-layers (3L), and few-layers (FL), when the loading force is

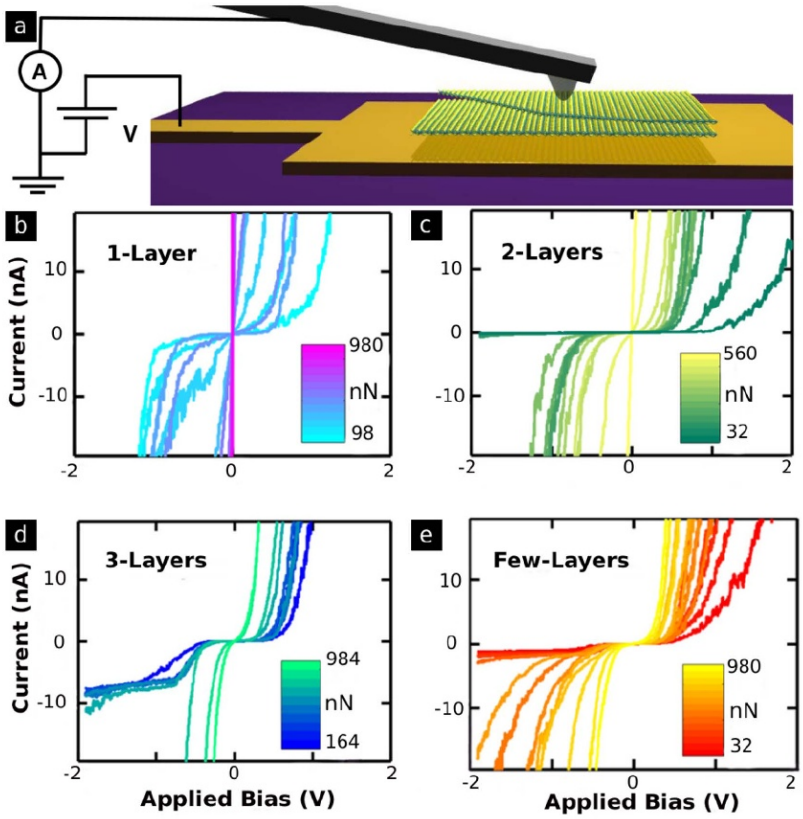

Figure 10 – a) A 3D model of the Conductive AFM (CAFM) experimental setup with a simple schematics of the CAFM, making explicit the grounded tip and the controlled voltage applied to the gold substrate below the MoS_2 flake. Current versus voltage for different forces in: (b) one-layer MoS_2; (c) two-layers MoS_2 ; (d) three-layers MoS_2; and (e) few-layers MoS_2.

low, the current saturates for voltages below -1 V (see figures 10(c–e)). A reliable contact was not obtained for applied forces below 98 nN on 1L MoS_2 . In the 3L sample, the electronic contact was not well established for forces lower than 160 nN, and the low-force saturation regime was not observed. However, such saturation regime for one-layer MoS_2 has been reported elsewhere(QUEREDA *et al.*, 2017). To understand the low-force regime, we can picture the system with a Schottky Barrier (SB) (see Sec. 2.3) formed in each semiconductor-metal interface of the tip-MoS_2-Au heterostructure. One SB at the top heterojunction (tip-MoS_2) and one SB at the bottom (MoS_2 -Au). Given the rectifying behaviour of the SBs, I-V characteristic curves of the heterostructures in the low-force regime are very non-linear and well described by the theory as two Schottky diodes connected in a back-to-back geometry, this was previously proposed by Quereda *et al.* (QUEREDA *et al.*, 2017). The saturation regime present in the negative bias region is described as a nearly-ideal Schottky contact formed in the MoS_2 -Au interface, that behaves as a diode. On the other hand, for the tip-MoS_2 contact, a highly non-ideal behaviour is observed, as frequently reported in CAFM experiments (QUEREDA *et al.*, 2017; DEB *et*

al., 2006; PATHAK *et al.*, 2018). It is important to mention that these low-force results are in good qualitative agreement with the measurements obtained in the literature using a conductive diamond tip and an ITO substrate (QUEREDA *et al.*, 2017). With increasing applied force, the I-V characteristic of the flake-substrate contact changes from a nearly-ideal Schottky diode, with well-defined current saturation, to a non-ideal SB, losing the saturation behaviour for an exponentially growing current for increasing negative voltages.

To better understand the results, we fit the experimental data to the back-to-back diode (diode resistor diode) model from the reference (QUEREDA *et al.*, 2017) and fully described in section 2.4. In figures 11(a) and (b), we describe (for the few-layers and two-layers MoS_2 heterostructures) the parameters: saturation currents for the contacts with the substrate (I_{sub}) and tip (I_{tip}), the inverse of the ideality factors for the contacts ($1/n_{tip}$, $1/n_{sub}$), and the system resistance (R) in function of the applied forces. Our results are in good agreement with previous reports for low-force setups (up to $\sim$ 100 nN for the two-layers sample, and $\sim$ 250 nN in the few-layers)(QUEREDA *et al.*, 2017). The internal resistance decreases with increasing applied force load, while the saturation current in the tip-MoS_2 heterojunction increases exponentially. Also, in the low-force domain, we verify the near ideal behaviour of the flake-substrate contact, i.e. the saturation current and ideality factor for the MoS_2-Au contact are nearly constant ($I_{sub} \approx$ 1.0 nA, $n_{sub} = 1.01$ for the few-layers sample). The ideality factor for the tip-flake heterojunction is also constant but near 2.0 ($1/n_{tip} \approx 0.5$) for the few-layers, while its inverse ($1/n_{tip}$) linearly decreases for the two-layers MoS_2, showing the non-ideal behaviour of the tip-flake interface. This behaviour changes from a specific force upwards (250 nN for few-layers and 100 nN for two-layers), in this high-force domain, the resistance of the system decreases with a different exponential rate, the saturation current in the tip-MoS_2 junction increases at a lower exponential rate, the saturation current for the MoS_2-substrate heterojunction is approximately constant (although more unstable than in the low-force regime), the ideality factor for the tip-MoS_2 contact is constant ($n_{tip} \approx 2.0$). Also, n_{sub} starts to increase ($1/n_{sub}$ decreases) with increasing applied force load, this causes the back current to also increase exponentially as the negative bias increases (detaching physical meaning from the I_{sub} parameter), as can be observed in figures 10(c) and (e) for both the two and few-layers samples.

To obtain the best fit values shown in Fig. 11, we start by first fitting the I-V curve for the lowest force value in each of the regions. The best fit values obtained for this force are used as starting points to fit the curve for the next value of force, in increasing steps. This procedure

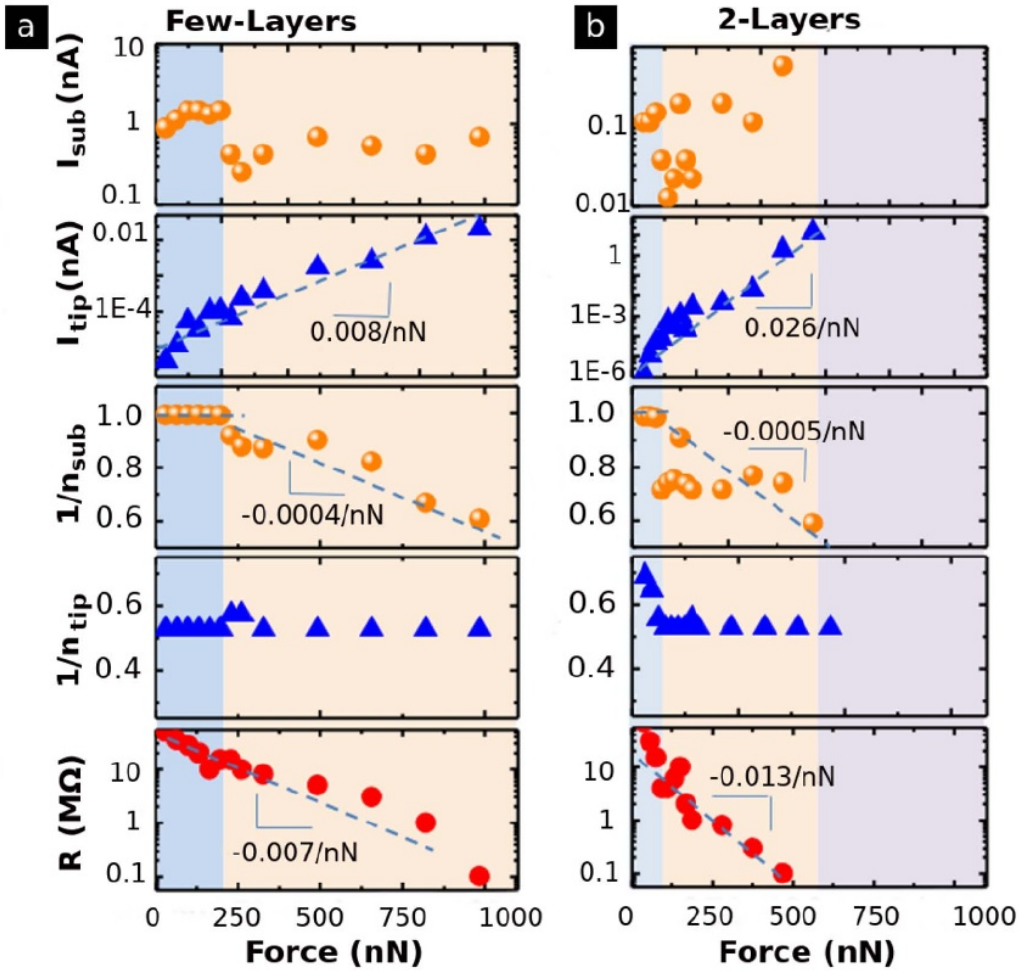

Figure 11 – Parameters that fit the measurements, figures 10(e) and (c), with the diode-resistor-diode (DRD) model (Sec. 2.4) for (a) few-layers and (b) two-layers MoS_2. The different colors indicate the change of force regime. For forces higher than 600 nN, the I-V measurements for the two-layers flake, (b), quickly reach our experimental current limit (20 nA), and the model cannot be further tested.

has the advantage of providing a more continuous evolution for the parameters, avoiding sudden jumps. On the other hand, it might also decrease the sensitivity of some of the fitting parameters to the evolution of the curves. For instance, we believe that the abruptness in the transition between the two behaviours observed in the fitted data (Fig. 11), but not captured by the proposed 3-diode model (see the next section - 4.4), might be an artifact of this chosen methodology. In principle, when the force is within the transition region, the small changes in the I-V curves are compensated by the more sensitive parameters until the change is large enough that these parameters, alone, can no longer compensate for the evolution of the curve. This generates a new set of parameters which will now evolve with the curve.

4.4 3-diode model

To better understand the physical process underlying the observed results, we recall that in an inhomogeneous Schottky barrier, the effective potential height becomes a function of the applied voltage(RT, 2014; DEY *et al.*, 2018), leading to a non-ideal behaviour of the Schottky contact (semiconductor-metal contact, see section 2.3 for a complete discussion on Schottky contact theory).

Several different possible effects can contribute to the loss of contact ideality(MANZELI *et al.*, 2017; JIANG *et al.*, 2019; KLYUKANOV *et al.*, 2012), but we argue that in our experimental CAFM setup, the intrinsic spatial inhomogeneity of the Schottky barrier is the dominant factor. The sharp geometry of the probe modifies the effective work function along the tip(KAUR; KANT, 2015), at the same time, there is an intrinsic inhomogeneity effect of the Schottky Barrier Height (SBH) due to the small contact area between the tip and the flake(RT, 2014; DEY *et al.*, 2018). With these reasons in mind, one should expect that the barrier height is much lower exactly under the tip and rapidly increases near the edges of the contact area, explaining the large value of the ideality factor for the tip-MoS_2 heterojunction (in accordance with Tung(TUNG, 1992)).

For the flake-substrate contact, we argue that, at low loading forces, the effective contact area between the MoS_2 and the substrate is much larger than the tip area. Thus, changes in the MoS_2 electronic band structure (and consequently on the Schottky Barrier Height) for the region under the tip has little effect on the flake-substrate saturation current, given the small portion suffering the band bending. In this way, the flake-substrate contact is rather homogeneous, leading to a nearly-ideal Schottky contact (ideality factor close to unity), in accordance with previous experiments(LIU *et al.*, 2018). However, as the force load increases, the strain causes the bandgap to close in the local region under the tip, lowering the SBH in this area - see section 4.4.1 for a discussion on band bending. Furthermore, as the bandgap closes (and the MoS_2 conduction band lowers), more electronic charges are transferred from the substrate to the flake, causing a decrease in the effective internal resistance. In this situation, there are two possible pathways for the charge carriers: they can either go through the broader unstrained surrounding area (A) with a pristine SBH (φ_0) or flow directly downwards from the tip through the small local region (area A_{local}) with reduced effective SBH ($\varphi_{eff} = \varphi_0 + \Delta\varphi$, with $\Delta\varphi < 0$). The dependence of barrier height change ($\Delta\varphi$) on the applied voltage arises from the spatial inhomogeneity of the Schottky Barrier created by this local strained area (Sec. 2.3.2). In the low-force regime, most of

the current flows to the substrate through the broad area A ($I_A >> I_{A_{local}}$) and the effect of the spatial inhomogeneity is negligible. However, as higher forces are applied, most of the current starts to funnel through the much smaller area A_{local}, and the ideality factor starts to increase. This idea is illustrated in figure 12(a).

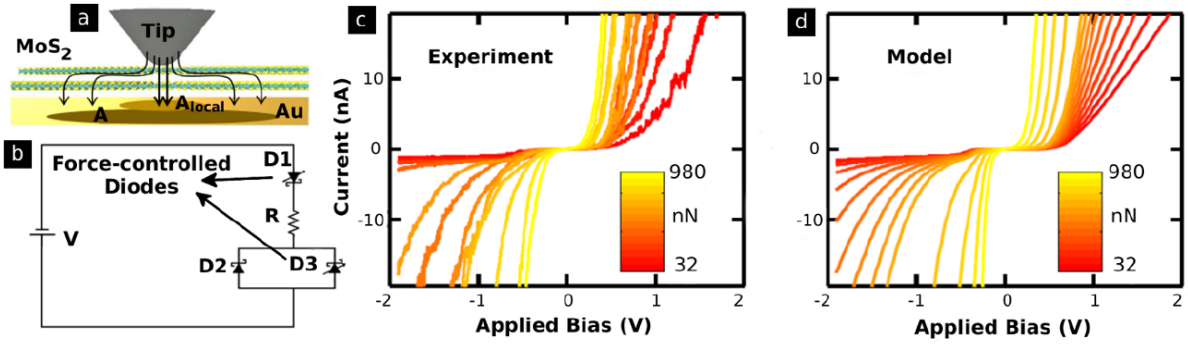

Figure 12 – (a) Illustration of the possible electronic transport pathways between the metallic tip and substrate. The current underneath the local pressured area A_{local} is controlled by the lower SBH determined by the valence band maximum of the strained MoS_2 in our experimental setup (for n-type barriers the conduction band minimum should be used). The current can also go through a broader surrounding unstrained region A with unperturbed SBH. (b) 3-diode circuit model for the analysed sample of grounded PtIr tip in contact with 2D MoS_2 deposited on an Au substrate with applied voltage. The diode D1 models the tip-flake contact; D2 models the flake-substrate contact for the broad surrounding area A; D3 models the flake-substrate contact for the strained area A_{local}, an arrow in the diode indicates its behaviour is dependent on the applied force. The resistor models the various mechanisms present in the sample that cause energy loss to the passing charges. (c) Experimental I-V curves for different applied loads in the few-layers region. (d) Calculated I-V curves for different loads using the model present in (b). The parameters that generate (d) are obtained from the results in figure 10, and by fitting the experimental data for selected values of the applied load F (further explanation in section 4.4.2).

Based on the physical understanding presented, we propose a model to describe the flake-substrate and tip-flake effective currents: each metal-semiconductor contact acts as a diode. Given that the substrate-MoS_2 contact allows for two different pathways, we model its effective behaviour as a combination of two parallel diodes: one (D2 in figure 12(b)) is nearly-ideal and force independent, corresponding to the current going through the large surrounding area A; and one force-tunable diode (D3) corresponding to the conduction through the local strained area A_{local}. The tip-flake diode (D1) is also assumed to be force-tunable with similar dependence as D3. The electrical resistance of the whole system is modelled as a resistor in the middle of the circuit. The circuit schematics of the proposed model is present in figure 12(b). Our proposed 3-diode model incorporates further physical information, reducing the total number of free parameters,

for experiments with force variation, in respect to the previous DRD model(QUEREDA *et al.*, 2017) (that does not include force dependent behaviour - Sec. 2.4). The mathematical equations for the 3-diode model are given in Sec. 4.4.2.

Underneath this model, there is a set of relevant assumptions. First of all, it is assumed that the tip-flake and flake-substrate Schottky Barriers are of the same type. According to published research, our experimental setup is consistent with the SBHs closely following the Schottky–Mott rule(LIU *et al.*, 2018)], and thus both being p-typed barriers. In this sense, as a loading force is applied to the MoS_2, causing the bandgap to close, the MoS_2 valence band moves up in energy, causing a decrease in both the tip-flake and flake-substrate barrier heights. An exponentially changing internal resistance that can be empirically modelled is assumed, as a result of charge transfer from the substrate caused by the MoS_2 conduction band decrease. Also, the inhomogeneous effect leading to the dependence of the SBH with applied voltage is assumed to be of the first order.

4.4.1 MoS_2 band bending through applied force[2]

It is known that applying pressure/strain causes the bandgap of MoS_2 to close with increasing applied force. In our atomic force microscope experiment, the force is applied via a nanometric tip (namely 25 nm radius) locally varying the bandgap of the few-layer MoS_2. Within the Schottky-Mott model, the SBH depends on either the conduction band minimum (electron affinity E_c) or the valence band maximum (binding energy E_v). Therefore, the pressure-induced closing of the energy gap reduces the SBH formed in the strained MoS_2 area.

In a publication, Liu *et al.* observe that, when MoS_2 is deposited on clean pre-patterned metallic substrates, the SBH follows the Schottky-Mott rule closely(LIU *et al.*, 2018):

$$e.\varphi = W_M - E_v \tag{4.1}$$

This means that for our sample, we should expect the MoS_2-substrate contact to behave as a p-barrier with a barrier height of about 0.3 V. Similarly, the MoS_2-PtIr tip hetero-junction should also behave as a p-barrier but with a much larger SBH (4.5-5.5 V). Therefore, the barrier height (φ) should depend on the difference between the work function of either of the metallic contacts (W_M) and the valence band edge of the semiconductor (E_v):

[2] This section was published in the Supplementary Information of the paper: De Araujo *et al.* (2020). **Controlling the electronic bands of a 2D semiconductor by force microscopy**. *2D Materials*, 7(4), 045029. doi.org/10.1088/2053-1583/aba5cb. One of the products of this Thesis.

As pressure is applied by the nanometric sized tip, the bandgap of MoS_2 in the region underneath the tip decreases with increasing applied force. This indicates that the valence band edge of the semiconductor should change. In this work, we assume that this change is linear (with coefficient γ) with the applied force (F), such that we have:

$$E_v = E_v^0 + e\delta, \tag{4.2}$$

with E_v^0 being the pristine valence band energy (at zero load force) and

$$\delta = \gamma F. \tag{4.3}$$

4.4.1.1 Flake-Substrate contact

For the flake-substrate barrier, the change in the MoS_2 valence band edge in the region near the physical contact area has two effects. First of all, it changes the nominal barrier height, which is obtained directly from the Schottky-Mott rule (equation 4.1). However, the fact that this change is only happening on this nanometric sized region where the tip and the flake are in physical contact introduces a geometric inhomogeneity in the SBH distribution along the contact surface between the MoS_2 and the underlying metal. When the SBH varies in the nanometric scale, the applied voltage affects the effective barrier height, being that in an inhomogeneous Schottky junction, the effective potential barrier height is a function of V (Sec. 2.3.2). In fact, in their original work, Tung *et al.* calculate the behaviour of the thermionic electrical current analytically considering a circular patch with a lower barrier height than the surrounding region(TUNG, 1992).

As discussed above, previous work shows that the electrical transport results can be written in terms of an effective barrier height, which is a function of: the SBH difference between the patch and the surrounding area, the radius of the patch, and the applied bias voltage(TUNG, 1992). Whereas there are many similarities between the studied experimental system and the model proposed by Tung *et al.*, there are also many important differences, one of these being the minimal width of the studied semiconductor flake, which in the mentioned work is assumed to be infinite. Therefore, instead of directly using the analytically calculated results, we propose only that the effective SBH can be expressed as a two-variable function $\varphi_{\text{eff}}(\delta, V)$, and approximate the behaviour using a Taylor expansion around the $\delta = 0; V = 0$ point. With this, we have:

$$\varphi_{\text{eff}}(\delta, V) = \varphi_{\text{eff}}(0,0) + \frac{\partial \varphi_{\text{eff}}}{\partial V}\Big|_{\delta=V=0} V + \frac{\partial \varphi_{\text{eff}}}{\partial \delta}\Big|_{\delta=V=0} \delta + + \frac{\partial^2 \varphi_{\text{eff}}}{\partial V \partial \delta}\Big|_{(\delta=V=0} V\delta + \ldots \tag{4.4}$$

The first term on the right-hand side is the pristine SBH (φ_0); the second term is null since the effective SBH does not depend on V when there is no inhomogeneity (for $\delta = 0$); from the Schottky-Mott rule (Eq. 4.1), we see that the derivative in the third term equals -1 at $V = 0$. Other non-crossed terms will either be null (since $\frac{\partial^n \varphi_{\text{eff}}}{\partial V^n}|_{\delta=0} = 0$), or neglected, considering small δ (i.e. $\delta^2 \approx 0$). With these considerations, we derive the expression:

$$\varphi_{\text{eff}}(\delta, V) = \varphi_{\text{eff}}(0,0) - \delta + \alpha V \delta, \tag{4.5}$$

in which we have defined $\alpha = \partial^2 \varphi_{\text{eff}} / \partial V \partial \delta$ taken at $V = \delta = 0$.

With such considerations, and introducing α (units of V^{-1}) and γ (units of V/N) as constants, we can finally give an expression for our effective Schottky barrier height for the locally strained region and its variation under applied force and bias.

$$\varphi_{\text{eff}} = \varphi_0 + \gamma F(\alpha V - 1) \tag{4.6}$$

$$\Delta\varphi = \gamma F(\alpha V - 1) \tag{4.7}$$

It is important to note here that while our analysis focuses on the force-dependent inhomogeneity caused by the variation of the MoS_2 bandgap in the strained region (varying thus the SBH), we cannot rule out other possible contributions to the ideality factor. For this reason, we include a force independent factor n_0, which encompasses all such possible contributions. With this, we can propose that the ideality factor for the locally strained region should follow the relation

$$\frac{1}{n} = \frac{1}{n_0} - \alpha\delta, \tag{4.8}$$

in which n_0 should be approximately constant along the semiconductor-substrate contact surface.

4.4.1.2 Tip-Flake contact

For the tip-flake electric contact, the expected SBH in the region under the tip, where there is physical contact, is given by:

$$\varphi_{tip} = \varphi^0_{tip} - \delta = \varphi^0_{tip} - \gamma F \tag{4.9}$$

in which $e.\varphi^0_{tip} = W_{tip} - E^0_v$ is the pristine SBH for the PtIr tip and MoS_2.

Away from the physical contact area, the effective barrier height increases exponentially fast (as the distance between the semiconductor and the metallic tip increases). This

variation also introduces a spatial inhomogeneity, which, in turn, should also give rise to a non-ideal Schottky contact. Since the SBH difference between the area underneath the tip and the area away from the tip is very large (virtually infinite), the ideality factor should be insensitive to small force-dependent variations of the semiconductor valence band edge and, thus, deemed constant and higher than unity. Therefore, in the case of the tip-flake contact, it is not possible to directly separate the contribution of the inhomogeneity to the ideality factor from other contributions.

4.4.2 Mathematical description of the model[3]

Our model aims to capture the behaviour of the electrical transport occurring in the tip-flake-substrate heterostructure (narrow metal–2D semiconductor–metal), including the influence of the force in the system.

The diode representing the tip-flake junction acts as a non-ideal Schottky diode. The SBH of this junction is governed by the properties of the locally strained MoS_2, and thus should be strongly dependent on the applied force. However, its far from ideal behaviour is expected to be approximately independent of the applied force. Therefore, for the tip-flake junction, we propose that the SBH varies simply as:

$$\Delta\varphi_{tip} = -\gamma F, \tag{4.10}$$

and that the non-ideality n_{tip} for this junction is constant.

For the internal resistance, we use the exponential decay observed in the fitting as:

$$R = R_0 \exp(-\beta F). \tag{4.11}$$

where R_0 is the resistance of the system at zero force and β is the exponential resistance lowering coefficient.

Now, for the flake-substrate junction, we have to consider that the carriers can either flow straight down from the locally strained MoS_2 area or spread to unstrained surrounding areas of the semiconductor and only then flow to the gold substrate through a pristine Schottky barrier. Since the two possible paths have different behaviours, we model this junction as two parallel diodes. The local area contact acts as a non-ideal force-dependent diode, and the surrounding contact acts as a nearly ideal, force independent Schottky diode with pristine SBH φ_0 and ideality factor n_0. The junction for the strained area is assumed to follow the behaviour discussed in Sec. 2.3.1, with effective SBH given by Eq. 4.6 and ideality factor following Eq. 4.8.

[3] This section has been published in the same Supplementary Information mentioned in the previous footnote.

Using these considerations, we model the flake-substrate junction as two parallel diodes: one ideal formed at the unstrained surrounding area, and one force-dependent formed at the local strained area. The total current through this junction is the sum of both possible paths, as presented in section 2.3.2. The effective contact areas (Ac_i in Eq. 2.11) are not directly measurable. Thus the ratio between both areas ($r = A_{local}/A$) is introduced as a parameter. The current passing through the two parallel diodes obey equation 2.11 with the considerations present in section 2.3.2 and the ratio of the areas (r) as a parameter. The expression for the total current in this junction is:

$$I_{sub} = A^* A T^2 \exp\left(\frac{V}{n_0 V_T}\right)\left[1-\exp\left(\frac{-V}{V_T}\right)\right] \times \left[r\exp\left(\frac{-\varphi_{eff}}{V_T}\right)+\exp\left(\frac{-\varphi_0}{V_T}\right)\right] \tag{4.12}$$

Figure 12(b) shows a schematic picture os this model. The force-controlled diode formed at the tip obeys equation 2.10 with n_{tip} as the ideality factor. The resistance of the system obeys Eq. 4.11. The parallel diodes formed at the surface junction obey Eq. 4.12. The circuit has the constraints of current conservation and the applied voltage is the sum of each component's voltage (Eqs. 2.13 and 2.14), but the substrate current I_s is the sum of the current through both diodes (figure 12(b)).

With the equations mentioned above, we can relate the parameters used in the modelling of each sample (β, γ, and α) with the fittings shown in figure 11 (I_{sub}, I_{tip}, n_{sub}, and n_{tip}). The explicit mathematical expressions for this are shown below:

$$\beta = -\frac{\partial}{\partial F} ln\left(\frac{R}{M\Omega}\right) \tag{4.13}$$

$$\gamma^* = \frac{\gamma}{V_T} = \frac{\partial}{\partial F} ln\left(\frac{I_{tip}}{nA}\right) \tag{4.14}$$

$$\alpha^* = V_T.\alpha = -\frac{V_T}{\gamma}\frac{\partial}{\partial F}\left(\frac{1}{n_{sub}}\right) \tag{4.15}$$

Using the equations above (Eq. 4.13, 4.14, 4.15) and the DRD fitting, we can extract most of the parameters for our 3-diode model. The remaining free parameter, namely the ratio between the locally strained and the total area (r), can be estimated by finding the value which best reproduces the evolution of the experimental results as the applied force is increased. The results, by layer thickness, are presented in table 2.

The fact that we capture the main physics of the experimental results by using this 3-diode model validates the assumption that the change of both the tip-flake and the flake-substrate SBH with applied force is mainly governed by the pressure-induced shift of the valence band

	I^0_{sub}(nA)	I^0_{tip}(pA)	r	n_0	n_{tip}	R_0(MΩ)	β(nN^{-1})	γ^*(nN^{-1})	α^*
Few-layers	0.6	0.04	0.04	1.01	1.8	62	0.007	0.008	0.002
3-layers	3.7	0.01	0.01	1.01	1.8	38	0.008	0.009	0.007
2-layers	0.04	0.0004	0.3	1.01	1.8	115	0.02	0.03	0.033

Table 2 – Table of obtained parameters from the proposed 3-diode model. I^0 indicates the saturation current in the "zero" force regime. r is the ratio between the local area and the surrounding area in the flake-substrate contact. n_0 is the ideality factor for this junction that is not connected to force-induced inhomogeneity in SBH. The resistance of the system without applied force is R_0. The equations defining the parameters β, γ^*, and α^* are Eqs. 4.13, 4.14, and 4.15.

edge, given the p-type nature of the Schottky contact (for an n-type contact the SBH change would be governed by the shift of the conduction band minimum). With this, we can use the fitted value of γ^* to estimate the rate with which the MoS_2 valence band edge changes with applied force ($\partial E_v/\partial F$). For $k_bT = 25.85$ eV (300 K) we estimate that $\partial E_v/\partial F$ is approximately 0.21, 0.23, and 0.78 meV/nN for the few-layers, three-layers, and two-layers MoS_2 respectively.

It should be noted that the proposed 3-diode model is built based on the previous DRD model(QUEREDA *et al.*, 2017) (Sec. 2.4) . The fact that our 3-diode model takes the force into account (F becomes a variable) shows an improvement on reproducing experiments with force variation.

4.4.3 Dependence on pressure and strain: a rough approximation[4]

We use force (in nN) because it is precisely measured by our AFM setup (Asylum AFM MFP-3D). Although pressure (in GPa) and strain are desirable units, we show below that a fare conversion is not a straightforward task. First of all, pristine AFM tips are usually considered to be nearly spherical, making the relation between force and pressure non-linear. To estimate pressure, we argue that the Hertzian model of contact between a sphere and a plane is the best option, but also, there are a few difficulties, as we discuss below.

1- The Hertzian model of contact gives us non-linear relations dependent on the radius of the tip. Even though the manufacturer provides an expected value (25 nm for Nanoworld EFM tip(NANOWORLD, 2020)), this is not individually determined, and deviations from the given value would result in increased uncertainty in the units.

2- We use the tips multiple times, and very likely, the tips deform. Each measurement includes a strong interaction between the tip and the substrate. The contact interactions deform the geometry of the tip, making the spherical approximation far from reality in non-pristine tips.

[4] This section was also published in the same Supplementary Information mentioned in previous footnotes.

3- The contact area is not directly measured, and the estimated value can add considerable uncertainty.

To overcome these difficulties, we use a combination of methods and approximations. First, we assume the pristine tip to be a sphere of radius 25 nm. Then we use the Hertzian model with the PtIr spherical tip (Young's modulus of 161 GPa and Poisson ratio of 0.15(DATABASE, 2020)) and Au plane substrate (Young's modulus of 79 GPa and Poisson ratio of 0.4(KELLY, 2014)) to calculate the radius of contact (a) at the maximum measured force ($a = 6.8$ nm at $F = 1000$ nN). We used the isotropic relations to find the Poisson ratios, given the information in the references(DATABASE, 2020; KELLY, 2014):

$$E = 2G(1+\nu) = 3K(1-2\nu) \tag{4.16}$$

in which E is the Young's modulus, G is the shear modulus (or modulus of rigidity), and ν is the Poisson ratio. We then assume the tip to be deformed in a way that the contact area is a flat circle with a radius of 6.8 nm, providing a contact area of $A_c = 145$ nm^2. With this more precise estimation, we use the linear relation to find the pressure as a function of measured force ($P = F/A_c$).

Many similar works available in the literature use measurements of strain, and it would also be interesting if we could transform our unity of force into strain, for comparison with those works(JOHN *et al.*, 2020; CONLEY *et al.*, 2013; HE *et al.*, 2013; ZHU *et al.*, 2013). Beyond the difficulties already presented, there is one more challenge to be considered in this unity change:

4- Related works usually apply uniform strain in the 2D crystal plane (xx and yy directions), while our work locally strains the crystal in the transverse direction (zz).

The 4th mentioned challenge is a fundamental difference between our work (inhomogeneous and vertical strain) and most published papers on the subject, meaning a different approach to the strain effect. Possible divergences could be the result of different material response to different kinds of strain.

To model the deformation of the flake in our vertical compression experiment, we must pay attention to the meaning of Young's modulus applied to thin films. In this context, Young's modulus is the constant of elasticity of the film for the in-plane strain (in xx and yy directions). Because of the anisotropy of the MoS_2 in the z-direction, its out-of-plane modulus of elasticity is different from the in-plane Young's modulus. In-plane elasticity is ruled by intra-layer chemical bonds, while the zz deformation is governed by inter-layer Van der Waals interactions.

This vertical elasticity study has been done experimentally and theoretically confirmed by molecular dynamics calculations. For few-layers MoS_2 its value is $C_{33} = 52$ GPa(ZHAO *et al.*, 2013; GHOBADI, 2017).

We define the vertical strain (ϵ) as the ratio between the flake's thickness variation (Δl) and the flake's thickness at "zero" force (l_0 as measured by AFM in tapping mode, Fig. 9(e)). Making use of the relations:

$$\Delta l = \frac{F \times l_0}{C_{33} \times A_c} \tag{4.17}$$

$$\epsilon = \Delta l / l_0 \tag{4.18}$$

With the mentioned approximations and estimates, we find the maximum applied force of 1000 nN to be equivalent to a pressure of 6.9 GPa, and a vertical strain of 13%. We are also able to find the rate of change for the Schottky Barrier Height (SBH). **It is important to notice the transformed unities are very dependent on our approximations, and they are given as a way to compare the order of magnitude of our data with data from different works available in the literature.**

From our estimates, the rates of change for the SBH become 31, 33, and 110 meV/GPa (16, 17, and 59 meV/% of strain) for few-layers, three-layers, and two-layers MoS_2, respectively. Some papers in the literature use different or multiple methods to determine the energy gap or SBH rate of change. In some cases, to compare with the rate of change of the energy gap, we have assumed, naively, the band gap closing to be uniform in relation to the variations of the electronic bands, leading to the SBH change rate being half of that of the band gap. For others, the SBH was directly measured or calculated. We see that our approach leads to values in the same order of magnitude as the change rates available in the literature. For instance, a linear regression from the data presented by Nayak et al. shows the E_{Gap} change rate to be on the order of 50 meV/GPa for the single-layer MoS_2(NAYAK *et al.*, 2014), which should lead to a SBH change of about 25 meV/GPa. John et al. measured the SBH of bi and multilayer MoS_2 to change by approximately 55 and 40 meV/% strain(JOHN *et al.*, 2020), for strain applied along the MoS_2 plane. We could also estimate the SBH change rates from other works to be on the order of 23 to 60 meV/% strain(CONLEY *et al.*, 2013; HE *et al.*, 2013; ZHU *et al.*, 2013).

4.5 Conclusions

With this work we used CAFM to measure the I-V curves of the metallic tip-MoS_2-metallic substrate devices under different local load forces (Fig. 10). With physical insights from the measurements, we were able to propose the 3-diode model described in Sec. 4.4 and generate a good quantitative estimate of Schottky barrier height change rate in respect to applied force.

[model-validation-SBH change rate*]Figures 12(c) and (d) respectively show the experimental and calculated I-V curves for the few-layers sample with different applied forces. As can be seen, the model captures extremely well the main features of the experimental results, validating the assumptions made in the model and thus allowing us to directly probe a set of useful information about the force-dependent electronic properties of the studied few-layers semiconductor. In this way, our results indicate that the change in the saturation current of the tip-flake contact can be used to estimate that **the rate at which the MoS_2 valence band shifts with the applied force is on the order of 0.21, 0.23, and 0.78 meV/nN for the few-layers, three-layers, and two-layers MoS_2, respectively** (for details see the Sec. 4.4).

[from force to strain*]It is interesting to represent the variation of the SBH concerning pressure or strain, it makes it easier to compare to other research. However, to evaluate the effective pressure or strain applied to the sample is not a straightforward task. By considering a constant contact area, which is a rather poor assumption, we can obtain a rough estimate of the SBH dependence on applied pressure and strain. To estimate the contact area, we assume the tip deforms from the multiple measurements, with its extremity taking the form of a flat circle. Find a detailed explanation in section 4.4.3. By taking the constant area to be of 145 nm^2 and the vertical modulus of elasticity of 52 GPa for thin MoS_2(ZHAO *et al.*, 2013; GHOBADI, 2017), the SBH change rate is found to be on the order of 31, 33, and 110 meV/GPa (16, 17, and 59 meV/% of strain), for FL, 3L, and 2L MoS_2 , respectively. Our approach leads to the SBH rate of change in the same magnitude as the literature, on the order of 23 to 60 meV/% of strain in few-layers MoS_2 (SHI *et al.*, 2013; JOHARI; SHENOY, 2012; JOHN *et al.*, 2020; CONLEY *et al.*, 2013; HE *et al.*, 2013; ZHU *et al.*, 2013) and 25 meV/GPa (NAYAK *et al.*, 2014) for pressure applied to monolayer MoS_2. With these assumptions, we find that the maximum measured force of 1000 nN leads to a pressure of 6.9 GPa, and a local vertical strain of 13% of the MoS_2 flakes.

[physical insights from model**]Furthermore, our model expands the knowledge of the research field by explaining why the saturation current of the flake-substrate contact is insensitive to the applied forces for weak loads, and also gives a good insight as to why the

tip-flake Schottky contact is far from ideal even at low forces, a previously untackled problem in CAFM applied to semiconductors.

4.6 Acknowledgments

The work presented here would not have been possible without my advisor Prof. Dr. E B Barros, nor without the hard experimental effort of my colleague and lab partner (at the time) Prof. Dr. Rodrigo Q Almeida. Prof. Dr. F C C S Salomão and Dr. F W N Silva also contributed directly for this experimental and intellectual endeavour.

The author wants to thank the collaborators from UFMG for the sample production and the insightful discussions, namely: Dr. Andreij C. Gadelha, Dr. Natália P Rezende, and Prof. Dr. Leonardo C Campos.

The author with the collaborators would like to thank the Central Analítica-UFC/CT-INFRA/MCTI-SISANO/Pró-Equipamentos CAPES for the support. This work was partially supported by the Brazilian Institute of Science and Technology (INCT) in Carbon Nanomaterials and the Brazilian agencies Fapemig. We thank the Coordenação de Aperfeiçoamento de Pessoal de Nível Superior (CAPES). The group also thanks the National Council for Scientific and Technological Development (CNPq) for funding this research.

5 MOS_2 EXCITON BEHAVIOUR IN A PLASMON-RICH ENVIRONMENT: INTERACTIONS WITH SUPERCRYSTALS OF GOLDNANOPARTICLES

Electric fields cause charge movement in metals' surfaces, when the field is oscillating it generates charge waves called *plasmons* (Sec. 2.5). By reducing the size of the metal structure to the nanometer scale, the surface portion of the material is maximized, the charge oscillations and the field are restricted to a small region along the particle surface, so plasmons in metallic nanoparticles (NPs - Sec. 3.2) are called *localized surface plasmons (LSP)* and have their properties determined by the particle's size. By arranging Au nanoparticles in an organized array, we allow the LSPs of neighboring NPs to interact with each other creating new collective oscillations that may travel through the superstructure.

Light-matter interactions (Sec. 2.5.1) govern many important phenomena in nature, from the heat generated by absorption, the detection of light by rhodopsin proteins that allow animals to see, all the way to the world's primary source of biological energy: photosynthesis. In technology this is also true, Einstein was given his Nobel prize by the explanation of the photoelectric effect and the same principle is behind photodetectors in labs, digital cameras, and photovoltaic solar cells. So we believe the exploration of new regimes of light-matter interaction is important and worth spending plenty of effort on, be it for the possible technological outcomes or simply for the satisfaction of our curiosity about how nature works in its details.

In this chapter we will investigate the effect of a plasmonic supercrystals composed of a face-centered-cubic arrangement of gold nanoparticles (or simply *supercrystals* - Sec. 3.2.1) on the optical properties of our thin semiconductor of choice (molybdenum dissulfide - MoS_2 Sec. 3.1). The supercrystals are known to operate on the ultra and deep-strong light-matter coupling regime, being the latter a regime just recently developed experimentally. In This regime photons are coupled to matter oscillations forming *plasmon-polaritons*. On the other hand, when light is shone on MoS_2 some excited electrons interact with the holes forming particles named *excitons* (Sec. 2.2.1). We will investigate the reflectance in MoS_2-supercrystals heterostructures with the intention of revealing how excitons interact with plasmons in this new regime of light-matter coupling.

5.1 Objectives

The general objective of the work presented in this chapter is to **check if there is exciton-plasmon interaction in the MoS_2-Au NPs supercrystal heterostructure and, if so,**

determine the possible interaction paths. This is done through the specific objectives:

- Absorbance measurements of different layer (L) numbers of MoS_2 on top of different layer numbers of Au NPs supercrystal to verify the excitonic behaviour in different local environments;
- Fit the measured spectra and analyse the peaks behaviour, comparing the heterostructures with its isolated counterparts;
- Use the measurements and fits to propose possible paths of interaction (or not) between the excitons in MoS_2 and the plasmons in the supercrystal.

5.2 Methods

The sample is composed of a glass substrate with supercrystals with different number of layers (L), on top of the supercrystals there are MoS_2 flakes with different number of layers. To prepare the sample we grew the supercrystals as described in section 3.2.1, the ~25nm Au nanoparticles (NPs) were functionalized with 5k-PSSH (table 4) and a glass substrate was used. We then used PDMS with exfoliated MoS_2 (Sec. 3.1.1.1) to deposit the MoS_2 on top of the supercrystals via the dry-stamp technique (Sec. 3.1.1.2). The dry stamp alignment was made in a way to have the most possible combinations of different layer numbers between both materials. Figure 13 shows schemes for different configurations of heterostructures, varying the number of layers for the MoS_2 and for the supercrystals.

We used contrast in bright and dark-field optical microscopy to identify the number of layers in our sample. See in figure 14 a transmission, bright-field microscopic image with the well defined number of supercrystal layers by the colour contrast (blue for monolayer (1L) supercrystal and dark purple for few-layers (FL)).

We used the procedures described in section 3.4 to measure reflectance, transmittance, and to calculate the absorbance for the different spots in the sample. Each spot (as shown in figure 14 and table 3) is made out of the glass with the MoS_2, the glass with the supercrystal, or the glass-supercrystal-MoS_2 heterostructure.

To help with the analysis of the measured absorbance spectra a fitting procedure was done, in order to acquire precise quantitative data on the shape and position of the background and the peaks. This was done with peak-o-mat(PEAK-O-MAT…, 2020) (a python based software). The background was modelled as a constant plus a Fermi step function (Eq. 5.1) and each peak was modelled as a Lorentzian curve (Eq. 5.2). The fitting was done in groups of spectra, always

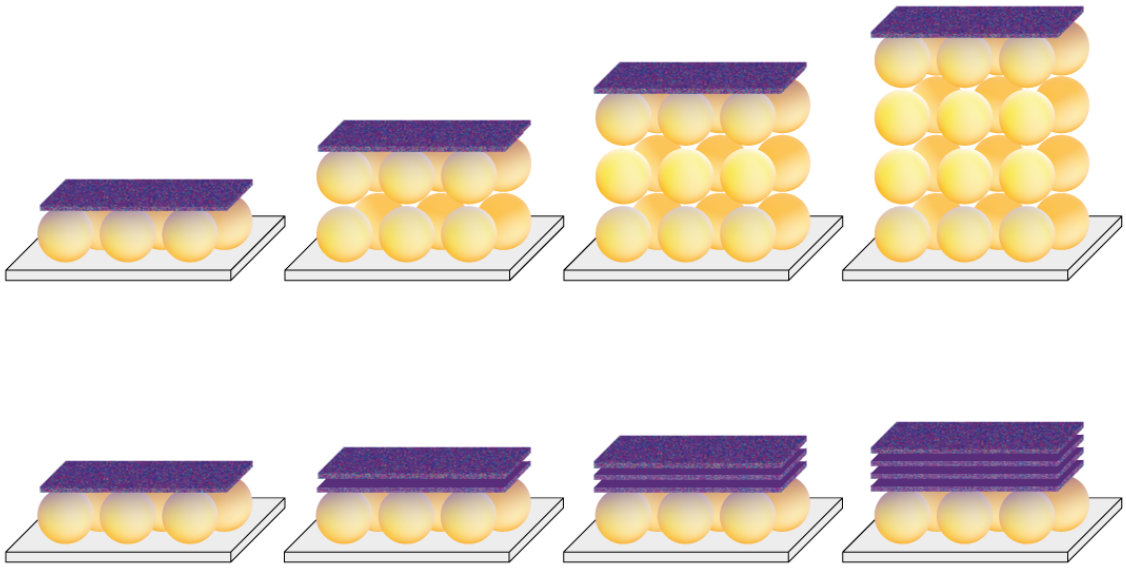

Figure 13 – Depiction of various heterostructures configurations. On top, from left to right: monolayer (1L) MoS_2 on top of 1L, 2L, 3L and 4L supercrystal. On the bottom, from left to right: 1L supercrystal covered with 1L, 2L, 3L and 4L MoS_2.

aiming for the evolution of parameters more coherent with the whole group - for example, when fitting the group of different layers of MoS_2 on top of monolayer supercrystal (Sec. 5.3.3, Fig. 18), we first fitted the few-layers (FL) MoS_2 on 1L supercrystal spectra using the peaks of FL MoS_2 and the step function of 1L supercrystal as starting parameters, once the best fit was done, we use the parameters obtained as starting point to fit the 4L MoS_2 on 1L supercrystal spectra and so on. This means we used slightly different fits for the same spot when analysed in combination with different groups of spectra. For example, the 1L MoS_2 on 1L supercrystal was fitted with two peaks when fitted together with the group of varied MoS_2 layers on top of 1L supercrystal (Sec. 5.3.3), while the same heterostructure was fitted with only one (larger) peak when the analysis was done in the context of 1L MoS_2 on top of varied supercrystal layers (Sec. 5.3.5).

$$f(x)_{Fermi-step} = \frac{A}{exp(E_0 - x)/k_B.T + 1} \tag{5.1}$$

$$f(x)_{Lorentzian} = \frac{A}{\left(\frac{x-E_0}{fwhm/2}\right)^2 + 1} \tag{5.2}$$

In the equations above A represents the maximum amplitude, E_0 is the energy peak position, k_B is Boltzmann's constant, T is absolute temperature, x is the light energy, and $fwhm$ is the full width at half maximum

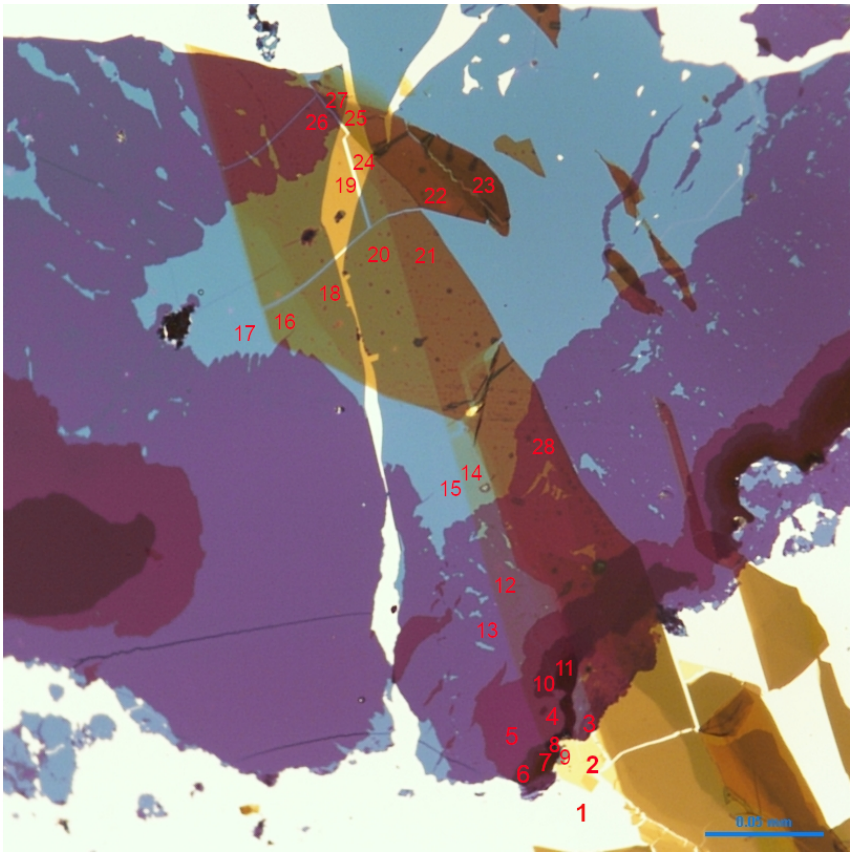

Figure 14 – An optical transmission bright-field microscope image of the sample analysed, with the regions of interest marked as spot numbers. Blue and purple areas are supercrystals with different layer numbers, the MoS_2 appears in yellow.

We fitted the measured spectra to obtain quantitative information (peak positions and full-width at half-maximum - FWHM), with this information we were able to properly analyse changes in the optical behaviour of the heterostructures and their isolated counterparts.

5.3 Results and Discussion

Our sample is depicted in figure 15, in it we have monolayer (1L), three-layers (3L), four-layers (4L) and few-layers (FL) of MoS_2 on top of glass, 1L and 2L of supercrystals. Unfortunately the area of 2L MoS_2 was small and we were only able to find it on top of 1L supercrystals. Find an electron microscope image of supercrystals, an optical image and a scheme of the heterostructure in figure 15. The spots measured are marked in Fig. 14 and table 3 identifies the number of MoS_2 and of supercrystals for each spot. We measured some spots with the same heterostructure configuration (in the case of spots 22 and 23 they have different thickness of FL MoS_2), this was done to check for consistency and we chose to show here the spots closer to other regions of interest - for example, we chose to use spot 8 for 1L MoS_2 on FL supercrystal

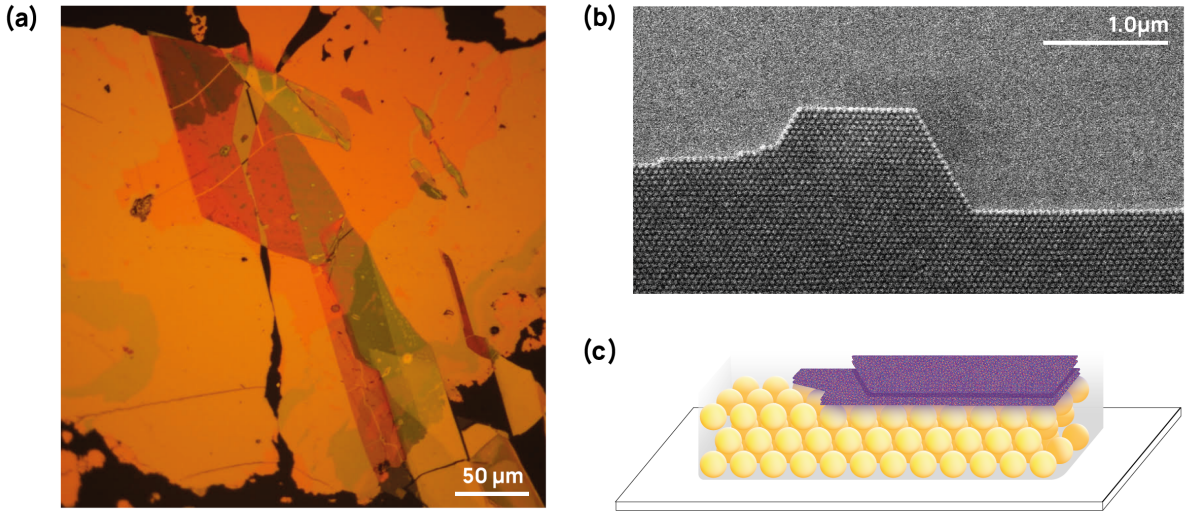

Figure 15 – (a)An optical reflection bright-field microscope image of the sample analysed (same region as in Fig. 14). (b) Scanning Electron Microscopy (SEM) image of Au NPs supercrystal. (c)A schematic representation of the glass-supercrystal-MoS_2 heterostructure.

for its proximity with spot 7.

MoS_2 \SC	**0L**	**1L**	**2L**	**3L**	**4L**	**FL**
0L	1	15 + 17	13	5	6	7
1L	2	14	12	3+4	10	8 + 9 + 11
2L		16				
3L	19	18	26			
4L	24	21	28			
Few-Layers	25	22+23	27			

Table 3 – Spot numbers according to their heterostructure configuration, always with glass on the bottom, followed by the supercrystal and finally the MoS_2. The numbers refer to the markings on figure 14. The first column indicates the number of MoS_2 layers, while the first row indicates the number of supercrystals layers. Squares with "+" indicate more than one spot with the same configuration, while empty squared indicate there were no spots with the corresponding configuration.

5.3.1 Absorption for varied MoS_2 layers

The absorption measurements in the varied Mos_2 layers (figure 16) reveals three peaks that we identified as the A, B and C excitons (1.87, 2.06 and 2.75 eV on average, respectively). This is in accordance with previous reports that indicate the same peaks in 1.88, 2.05 and 2.82eV for MoS_2 on top of PDMS(CASTELLANOS-GOMEZ *et al.*, 2016). The narrow peaks of the A and B excitons are associated with the direct transitions at the K point of the MoS_2's

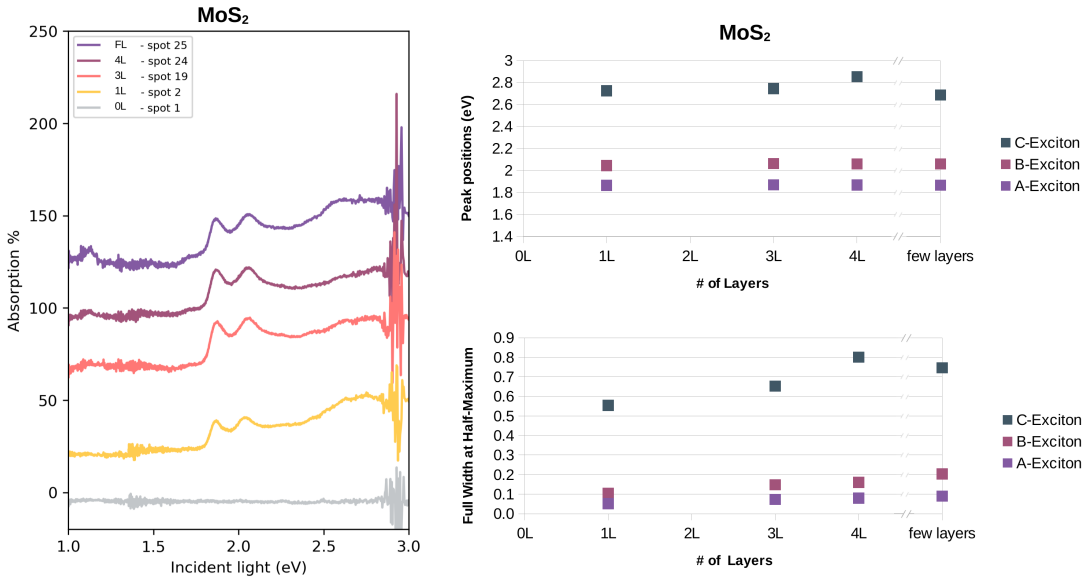

Figure 16 – Absorption spectra for varied number of MoS_2 layers. With the positions (top-right) and full width at half-maximum (bottom-right) of the peaks found in the fitting procedure for the corresponding spectra.

Brillouin Zone (Fig. 4), their energy difference is associated with the spin orbit-coupling in these structures(MUELLER *et al.*, 2018) . The origin of the broad exciton C peak is still a subject of debate(CASTELLANOS-GOMEZ *et al.*, 2016).

5.3.2 Absorption for varied supercrystal layers

[supercrystals absorption]The optical behaviour of layered gold nanoparticle supercrystal is controlled by the resonant standing-wave modes, i.e. collective plasmons. More modes appear as the thickness of the supercrystal increases and are identified with j = 1, 2, 3... and are related to the vertical standing wave inside the material (check figure 3 of reference(MUELLER *et al.*, 2020), where they indicate $j = 2h/\lambda_{pp}$ - h is height and λ_{pp} is the plasmon-polariton wavelength). Our measured spectra (Fig. 17) show absorption peaks for the same plasmonic modes (identified with j1, j2, and j3), with new modes appearing and with the modes decreasing in energy with increasing number of supercrystal layers. This behaviour corresponds to the behaviour in supercrystals with ultra- and deep-strong light-matter coupling regimes(MUELLER *et al.*, 2020). Notice there are no peaks for the glass underneath the samples, nor for the monolayer supercrystal.

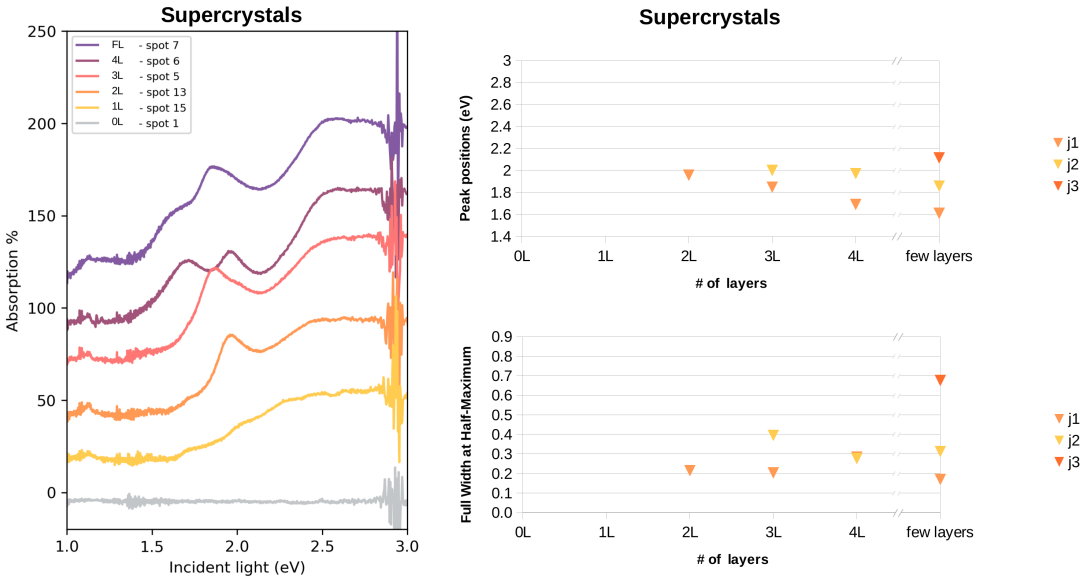

Figure 17 – Absorption spectra for varied number of supercrystal layers. With the positions (top-right) and full width at half-maximum (bottom-right) of the peaks found in the fitting procedure for the corresponding spectra.

5.3.3 Effect of 1L supercrystal substrate on the absorption of MoS_2 layers

When analysing MoS_2 with growing thickness on top of monolayer supercrystal we verify two peaks that become more prominent and grow further apart, until their distinction is very clear in the few-layers sample, where they are easily identified as the A and B excitons, in this sample the C exciton also appears[1]. Because of this asymptotic behaviour (made clear in figure 19) we feel confident in naming these peaks exciton A and B. What this tells us is that, whatever the source of influence the plasmonic substrate has with the excitons in MoS_2, this influence is confined to an area near the surface of the supercrystal, drastically affecting, thus, the thin samples, while having a smaller effect in thicker MoS_2.

We find the explanation for this in the dielectric screening effect, in accordance with previous experimental reports of exciton blue shift as a function of the dielectric constant of the surrounding environment(LIN *et al.*, 2014). The high index of refraction of the substrate (reported as ∼11 for similar supercrystals, with 25nm gold NPs(MUELLER *et al.*, 2020)) drastically alters the exciton interaction fields that travel through the region inside the supercrystal leading to higher energy resonances when compared to pristine MoS_2. This leads to a different averaged interaction between the electrons and the holes, this effect is less evident in thick samples where

[1] In the appendix B find the plots from Figs. 18 and 20 with vertical guide lines in the MoS_2 excitons A and B positions

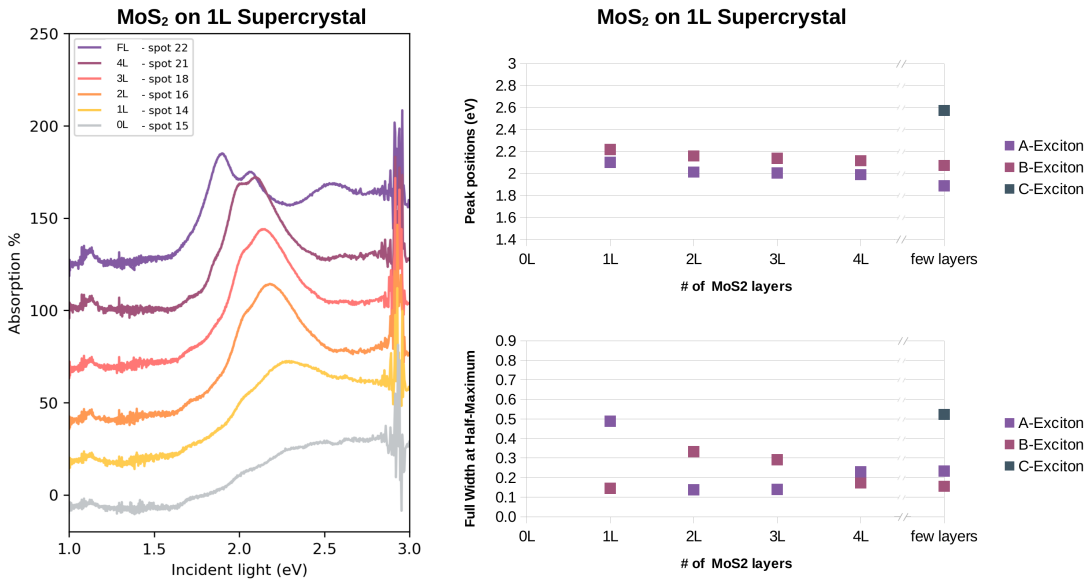

Figure 18 – Absorption spectra for varied number of MoS_2 layers on top of a monolayer of supercrystal. With the positions (top-right) and full width at half-maximum (bottom-right) of the peaks found in the fitting procedure for the corresponding spectra.

most of the excitons are formed far from the contact surface.

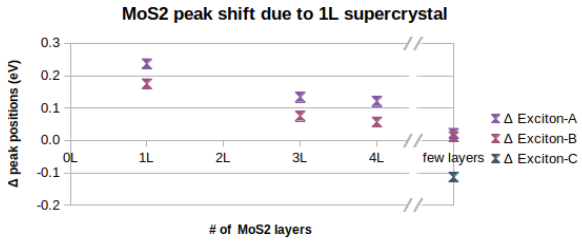

Figure 19 – Variation of the exciton absorption peaks caused by placing MoS_2 on top of a monolayer supercrystal. This was calculated by subtracting the pristine MoS_2 excitonic peaks (Fig. 16) from their corresponding peaks with the 1L supercrystal underneath (Fig. 18).

5.3.4 Absorption for varied MoS_2 layers, on top of 2L supercrystal

When we increase the thickness for 2L supercrystals and vary the number of MoS_2 layers, many features appear in the same spectral region, given the proximity of the j1 peak in 2L supercrystal to the A and B exciton peaks in MoS_2, the fit aids us in analysing this collection of spectra. With the analysis done in the previous section in mind (Sec. 5.3.3), we identify two peaks as the excitons A and B that approach their pristine values in for the few-layers MoS_2 region (see Fig. 21), this behaviour corroborates to our previous analysis - the influence of the

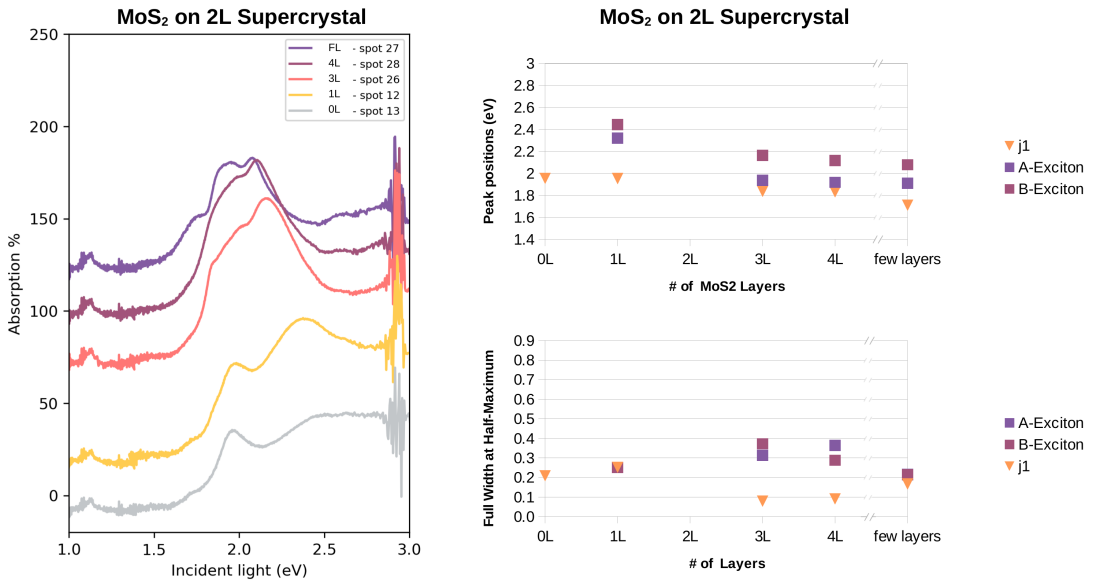

Figure 20 – Absorption spectra for varied number of MoS_2 layers on top of a bi-layer (2L) supercrystal. With the positions (top-right) and full width at half-maximum (bottom-right) of the peaks found in the fitting procedure for the corresponding spectra.

high index of refraction of the supercrystal is restricted to excitons in a thin area near its surface.

This section contrasts with the 1L supercrystal environment found in the last section, where the excitons had no plasmonic mode to interact. Here, the MoS_2 finds a plasmonic mode (j1) in the same energy region as the excitons, making interactions likely. We notice the j1 plasmonic peak lowers in energy for increasing MoS_2 thickness. This is noticeable for 3L and thicker MoS_2 (see Fig. 21), where the excitonic density is larger and so it the total dipole moment of the MoS_2, facilitating the interaction with the oscilating dipole modes of the supercrystal.

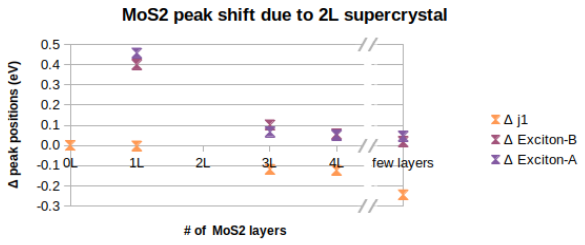

Figure 21 – Variation of the exciton absorption peaks caused by placing MoS_2 on top of a bi-layer (2L) supercrystal. This was calculated by subtracting the pristine MoS_2 excitonic peaks (Fig. 16) from their corresponding peaks with the 2L supercrystal underneath (Fig. 18).

5.3.5 *Effect of one MoS_2 layer to the supercrystal absorption*

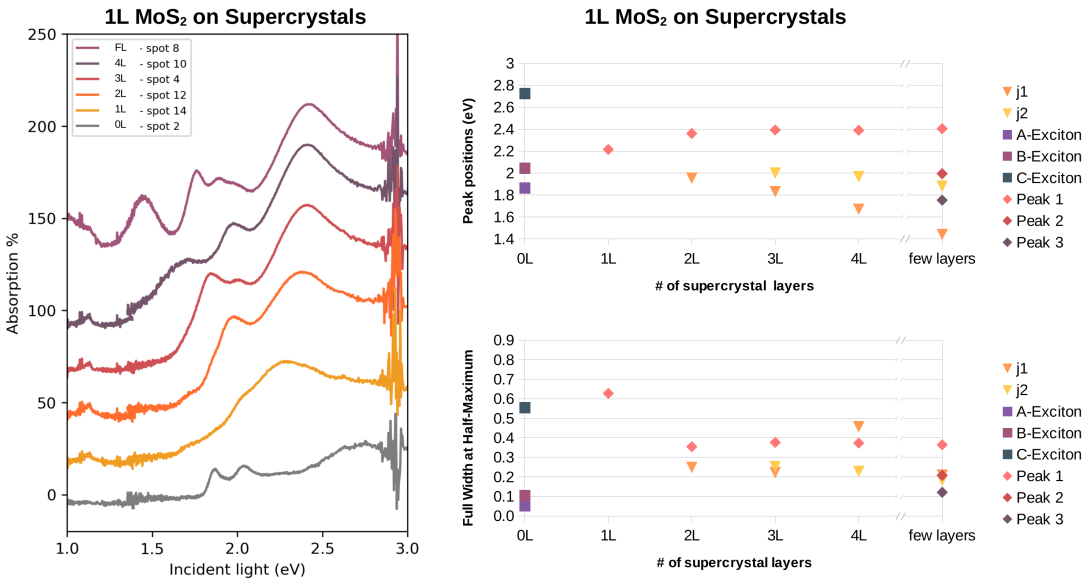

Figure 22 – Absorption spectra for varied number of supercrystal layers on top of a monolayer MoS_2. With the positions (top-right) and full width at half-maximum (bottom-right) of the peaks found in the fitting procedure for the corresponding spectra.

When we cover the supercrystals with an MoS_2 monolayer and measure their absorbance spectra (figure 22), we can notice the plasmonic modes (j1, j2, and j3) are still present in the same positions as the ones in the pristine supercrystal (Fig. 17) - the fitting procedure shows a reduction smaller than 20meV (6meV) for the j1 (j2) mode in the heterostructure up until four layers. This shows us that the presence of the MoS_2 doesn't affect the plasmonic modes that the supercrystal had without the thin cover.

For the sake of simplicity, during the fitting procedure we decided to fit the exciton A and B peaks (that are very close together and were already discussed) as a single peak (Peak 1). We notice this AB excitonic peak upshifts in energy from mono to three-layer supercrystal, reaching an equilibrium. This corroborates further with the explanation given of the dielectric screening by the high dielectric constant material. Increasing the number of supercrystal layers the force fields of the A and B excitons are more affected, but this effect reaches a limit as the fields that travel too far from the excitons have little effect on their energy.

One final thing that calls attention in this collection of measurements is the considerable difference between the spectra for the few-layers supercrystal. The area covered by the

MoS_2 has two peaks, it is not clear if Peak 2 in the spectra of Fig. 22 is the j3 plasmonic mode, it is positioned over 100meV below the peak in the uncovered supercrystal (j3 in Fig. 17). The other feature, Peak 3, could very well be another plasmonic mode (j4 maybe), but it is not present in the few-layers supercrystal with nothing on top. When closely analysing the area of the sample corresponding to spectra in question (spots 7 and 8 in the optical image, figure 14), we notice it is an area near the edge of the supercrystal macro-structure, its irregularity in topography might as well be the cause of this unexpected behaviour. i.e. It is possible that we are trying to compare different thickness of supercrystals, and such comparison should not gain much attention.

A superposition of the supercrystals spectra with and without 1L MoS_2 on top is presented in appendix B.

5.4 Conclusions

In this chapter we presented absorption spectra for a big variety (21 in total) of MoS_2-supercrystal configurations, in relation to the number of layers of each material. The analysis of the experimental data allowed us to verify the influence of the supercrystal in the A and B excitons, pushing them further apart from their pristine counterparts the thinner the MoS_2 (Fig. 19). This allows us to conclude that the interference of the supercrystal for these excitons is restricted to a thin portion of the volume exactly above the surface of the supercrystal. We further propose this evanescent influence is due to the dielectric screening of the excitons' Coulomb interaction, drastically up-shifting the excitons' resonance energy because of the extraordinarily high index of refraction of the plasmonic substrate.

We were also able to demonstrate the interaction by a red-shift of the j1 mode of the bi-layer supercrystal with three and more layers MoS_2, given their higher exciton density and total dipole moment. Further investigation is needed to understand this plasmon-exciton interaction, we believe theoretically modelling the heterostructues will shed more light into the questions risen here. Future experimental work is already on the way, with different 2D materials on top of supercrystals.

6 CONCLUSIONS

With the work presented in this thesis, we are able to verify how bi-dimensional Molybdenum Dissulfide feels the effects of surface interactions, using an investigative and methodical approach, we present a qualitative and quantitative analysis on how contact changes the electrical and optical properties of MoS_2. In the first part (Chap. 4), we not only show that a nanoscale contact with MoS_2 shifts the valence band as a function of compressive pressure, but also quantitatively model this shift - finding the rate of change to be 0.21, 0.23, and 0.78 meV/nN for the few-layers, three-layers, and two-layers MoS_2, respectively. In the second part of the work (Chap. 5, we verify the exciton energies in MoS_2 drastically blue-shifts when contact is made with a gold Nanoparticles supercrystal, an effect due to the high index of refraction of the contacted material. We also verify the effect of the excitons' dipoles red-shifting a plasmon mode of the neighbouring supercrystal.

In chapter 4, our proposed 3-diode model, together with the Schottky contact theory, is shown able to simulate the Conductive Atomic Force Microscopy (CAFM) I-V results in MoS_2. When combined with experimental data, the model opens up new possibilities of investigating the manipulation of the electronic properties of 2D semiconducting materials. Inhomogeneous barrier effects explain the non-ideal Schottky contact present in the tip-flake interface, pinpointing the small geometry of the tip as the main explanation for ideality factors higher than unity in CAFM measurements. The flake-substrate interface acts as a broad ideal Schottky contact in the low-force domain. For high applied forces, the local strain shifts the MoS_2 valence band, lowering the local Schottky Barrier Height (SBH), and most of the current goes through the small strained area. The local shift of the band also leads to SBH inhomogeneity, which gives rise to the non-ideal behaviour observable for the flake-substrate contact in the high-force regime. We verify that increment in compressive force decreases the resistance of the system and the Schottky Barriers in both contacts. With the validation of our model, we are able to estimate from the experiments the rate of change in the MoS_2 valence band energy to be on the order of 0.21, 0.23, and 0.78 meV/nN for the few-layers, three-layers, and two-layers MoS_2, respectively. Making rough approximations (Sec. 4.4.3), we can translate these values to 31, 33, and 110 meV/GPa (16, 17, and 59 meV/% of strain), for FL, 3L, and 2L MoS_2, respectively.

In chapter 5, we show that placing the MoS_2 on a material with high light-matter interaction up-shifts the resonance energy of the excitons. This is due to the strong dielectric-screening of such materials, the high index of refraction interferes with the path of the Coulomb

force field of the electron-hole interactions, but this effect is only felt in a very thin area right on top of the supercrystal's surface, so the excitons on the MoS_2 layers next to the supercrystal are the most affected. The excitons also interfere with the resonant energy of the plasmon mode of the supercrystal, the collective dipole oscillations of the material are insensitive to very thin MoS_2, but increasing the number of layers increases the number of excitons (and the total dipole moment) and the plasmon mode resonance lowers in energy. So there are exciton-dipole interactions on the MoS_2-supercrystal interface, and the optical behaviour of MoS_2 (governed by the excitons) is sensitive to surface contacts in the semiconductor.

6.1 Products

The work done in chapter 4 was published as an article in a peer-reviewed paper:

De Araujo, D. B., De Almeida, R. F., Gadelha, A. C., Rezende, N. P., Salomão, F. C. C. S., Silva, F., Campos, L. C., &Barros, E. B. (2020). **Controlling the electronic bands of a 2D semiconductor by force microscopy**. *2D Materials*, 7(4), 045029. doi.org/10.1088/2053-1583/aba5cb.

The images and some parts of the text of the corresponding chapter were taken from the published article and its Supplementary Information.

The work was also presented in a conference:

DE ARAÚJO, D. B.; ALMEIDA, R. Q. ; BARROS, E. B. . **Study of electrical transport in 2D MoS_2**. In: Encontro de Outono da SBF, 2019 (Fall meeting of the Brazilian Physics Society, 2019), Aracaju, SE .

Most of the work from chapter 5 was done during a Sandwich experience at Freie Universität Berlin with the funding of the CAPES - Print project (12 months Doctorate sandwich fellowship) and the European Research Council (6 months PhD fellowship), for a total of 18 months abroad.

During the development of this Doctorate, collaborations were possible leading to some parallel publications:

Luis P.M. dos Santos, Rafael M. Freire, Sebastian Michea, Juliano C. Denardin, Daniel B. Araújo, Eduardo B. Barros, Adriana N. Correia, Pedro de Lima-Neto. **Electrodeposition of 1-D tellurium nanostructure on gold surface from choline chloride-urea and choline chloride-ethylene glycol mixtures**, Journal of Molecular Liquids. 2019, Volume 288, 111038, ISSN 0167-7322, doi.org/10.1016/j.molliq.2019.111038.

Jan N. Kirchhof, Yuefeng Yu, Gabriel Antheaume, Georgy Gordeev, Denis Yagodkin, Peter Elliott, Daniel B. de Araújo, Sangeeta Sharma, Stephanie Reich, and Kirill I. Bolotin. **Nanomechanical Spectroscopy of 2D Materials**. Nano Lett. 2022, 22, 20, 8037–8044. doi.org/10.1021/acs.nanolett.2c01289.

Jan N Kirchhof, Yuefeng Yu, Denis Yagodkin, Nele Stetzuhn, Daniel B de Araújo, Kostas Kanellopulos, Samuel Manas-Valero, Eugenio Coronado, Herre van der Zant, Stephanie Reich, Silvan Schmid and Kirill I Bolotin. **Nanomechanical absorption spectroscopy of 2D materials with femtowatt sensitivity**. 2023. 2D Mater. **10** 035012. doi.org/10.1088/2053-1583/acd0bf.

BIBLIOGRAPHY

ABERASTURI, D. J. de; SERRANO-MONTES, A. B.; LIZ-MARZÁN, L. M. Modern applications of plasmonic nanoparticles: From energy to health. **Advanced Optical Materials**, Wiley, v. 3, n. 5, p. 602–617, feb 2015.

ARAÚJO, D. B. de; ALMEIDA, R. Q.; GADELHA, A. C.; REZENDE, N. P.; SALOMÃO, F. C. C. S.; SILVA, F. W. N.; CAMPOS, L. C.; BARROS, E. B. Controlling the electronic bands of a 2d semiconductor by force microscopy. **2D Materials**, IOP Publishing, v. 7, n. 4, p. 045029, sep 2020.

BHATTACHARYYA, S.; SINGH, A. K. Semiconductor-metal transition in semiconducting bilayer sheets of transition-metal dichalcogenides. **Physical Review B**, American Physical Society (APS), v. 86, n. 7, p. 075454, aug 2012.

CASTELLANOS-GOMEZ, A.; BUSCEMA, M.; MOLENAAR, R.; SINGH, V.; JANSSEN, L.; ZANT, H. S. J. van der; STEELE, G. A. Deterministic transfer of two-dimensional materials by all-dry viscoelastic stamping. **2D Materials**, IOP Publishing, v. 1, n. 1, p. 011002, apr 2014.

CASTELLANOS-GOMEZ, A.; QUEREDA, J.; MEULEN, H. P. van der; AGRAïT, N.; RUBIO-BOLLINGER, G. Spatially resolved optical absorption spectroscopy of single- and few-layer MoS2by hyperspectral imaging. **Nanotechnology**, IOP Publishing, v. 27, n. 11, p. 115705, feb 2016.

CASTRO-VILLARREAL, P.; RUIZ-SÁNCHEZ, R. Pseudomagnetic field in curved graphene. **Physical Review B**, American Physical Society (APS), v. 95, n. 12, p. 125432, mar 2017.

CHAVES, A.; AZADANI, J. G.; ALSALMAN, H.; COSTA, D. R. da; FRISENDA, R.; CHAVES, A. J.; SONG, S. H.; KIM, Y. D.; HE, D.; ZHOU, J.; CASTELLANOS-GOMEZ, A.; PEETERS, F. M.; LIU, Z.; HINKLE, C. L.; OH, S.-H.; YE, P. D.; KOESTER, S. J.; LEE, Y. H.; AVOURIS, P.; WANG, X.; LOW, T. Bandgap engineering of two-dimensional semiconductor materials. **npj 2D Materials and Applications**, Springer Science and Business Media LLC, v. 4, n. 1, aug 2020.

CHHOWALLA, M.; SHIN, H. S.; EDA, G.; LI, L.-J.; LOH, K. P.; ZHANG, H. The chemistry of two-dimensional layered transition metal dichalcogenide nanosheets. **Nature Chemistry**, Springer Science and Business Media LLC, v. 5, n. 4, p. 263–275, mar 2013.

CHOI, W.; CHOUDHARY, N.; HAN, G. H.; PARK, J.; AKINWANDE, D.; LEE, Y. H. Recent development of two-dimensional transition metal dichalcogenides and their applications. **Materials Today**, Elsevier BV, v. 20, n. 3, p. 116–130, apr 2017.

COLLINS, C. B.; CARLSON, R. O. Properties of silicon doped with iron or copper. **Physical Review**, American Physical Society (APS), v. 108, n. 6, p. 1409–1414, dec 1957.

CONLEY, H. J.; WANG, B.; ZIEGLER, J. I.; HAGLUND, R. F.; PANTELIDES, S. T.; BOLOTIN, K. I. Bandgap engineering of strained monolayer and bilayer MoS2. **Nano Letters**, American Chemical Society (ACS), v. 13, n. 8, p. 3626–3630, jul 2013.

DANIEL, M.-C.; ASTRUC, D. Gold nanoparticles: assembly, supramolecular chemistry, quantum-size-related properties, and applications toward biology, catalysis, and nanotechnology. **Chemical Reviews**, American Chemical Society (ACS), v. 104, n. 1, p. 293–346, dec 2003.

DATABASE, P. **Platinum - 5.00Available at: http://www.pgmdatabase.com/jmpgm/data/datasheet.do?record=1178&database=cesdatabase.**

DEB, P.; KIM, H.; QIN, Y.; LAHIJI, R.; OLIVER, M.; REIFENBERGER, R.; SANDS, T. GaN nanorod schottky and p-n junction diodes. **Nano Letters**, American Chemical Society (ACS), v. 6, n. 12, p. 2893–2898, nov 2006.

DEY, A.; JANA, R.; DHAR, J.; DAS, P.; RAY, P. P. Gaussian distribution of inhomogeneous barrier height of al/ZnS/ITO schottky barrier diodes. **Materials Today: Proceedings**, Elsevier BV, v. 5, n. 3, p. 9958–9964, 2018.

DICKINSON, R. G.; PAULING, L. THE CRYSTAL STRUCTURE OF MOLYBDENITE. **Journal of the American Chemical Society**, American Chemical Society (ACS), v. 45, n. 6, p. 1466–1471, jun 1923.

FENG, J.; QIAN, X.; HUANG, C.-W.; LI, J. Strain-engineered artificial atom as a broad-spectrum solar energy funnel. **Nature Photonics**, Springer Science and Business Media LLC, v. 6, n. 12, p. 866–872, nov 2012.

FOSSILIENATLAS, M. **Molybdenite**. Available at: https://www.mineralienatlas.de/lexikon/index.php/MineralData?mineral=Molybdenite.

GADELHA, A. C.; CADORE, A. R.; WATANABE, K.; TANIGUCHI, T.; PAULA, A. M. de; MALARD, L. M.; LACERDA, R. G.; CAMPOS, L. C. Gate-tunable non-volatile photomemory effect in MoS 2 transistors. **2D Materials**, IOP Publishing, v. 6, n. 2, p. 025036, mar 2019.

GHOBADI, N. A comparative study of the mechanical properties of multilayer MoS 2 and graphene/MoS 2 heterostructure: effects of temperature, number of layers and stacking order. **Current Applied Physics**, Elsevier BV, v. 17, n. 11, p. 1483–1493, nov 2017.

GUO, L.; KRAUSS, P. R.; CHOU, S. Y. Nanoscale silicon field effect transistors fabricated using imprint lithography. **Applied Physics Letters**, AIP Publishing, v. 71, n. 13, p. 1881–1883, sep 1997.

HAISS, W.; THANH, N. T. K.; AVEYARD, J.; FERNIG, D. G. Determination of size and concentration of gold nanoparticles from UV-vis spectra. **Analytical Chemistry**, American Chemical Society (ACS), v. 79, n. 11, p. 4215–4221, apr 2007.

HAN, G. H.; DUONG, D. L.; KEUM, D. H.; YUN, S. J.; LEE, Y. H. van der waals metallic transition metal dichalcogenides. **Chemical Reviews**, American Chemical Society (ACS), v. 118, n. 13, p. 6297–6336, jun 2018.

HE, K.; POOLE, C.; MAK, K. F.; SHAN, J. Experimental demonstration of continuous electronic structure tuning via strain in atomically thin MoS2. **Nano Letters**, American Chemical Society (ACS), v. 13, n. 6, p. 2931–2936, may 2013.

HOLLER, J.; BAURIEDL, L.; KORN, T.; SEITZ, A.; ÖZYIGIT, F.; EICHINGER, M.; SCHüLLER, C.; WATANABE, K.; TANIGUCHI, T.; STRUNK, C.; PARADISO, N. Air tightness of hBN encapsulation and its impact on raman spectroscopy of van der waals materials. **2D Materials**, IOP Publishing, v. 7, n. 1, p. 015012, nov 2019.

HSU, Y.-T.; VAEZI, A.; FISCHER, M. H.; KIM, E.-A. Topological superconductivity in monolayer transition metal dichalcogenides. **Nature Communications**, Springer Science and Business Media LLC, v. 8, n. 1, apr 2017.

JARIWALA, D.; DAVOYAN, A. R.; WONG, J.; ATWATER, H. A. Van der waals materials for atomically-thin photovoltaics: Promise and outlook. **ACS Photonics**, American Chemical Society (ACS), v. 4, n. 12, p. 2962–2970, nov 2017.

JIANG, L.; WEBER, J.; PUGLISI, F. M.; PAVAN, P.; LARCHER, L.; FRAMMELSBERGER, W.; BENSTETTER, G.; LANZA, M. Understanding current instabilities in conductive atomic force microscopy. **Materials**, MDPI AG, v. 12, n. 3, p. 459, feb 2019.

JIN, W.; YEH, P.-C.; ZAKI, N.; ZHANG, D.; SADOWSKI, J. T.; AL-MAHBOOB, A.; ZANDE, A. M. van der; CHENET, D. A.; DADAP, J. I.; HERMAN, I. P.; SUTTER, P.; HONE, J.; OSGOOD, R. M. Direct measurement of the thickness-dependent electronic band structure of MoS2using angle-resolved photoemission spectroscopy. **Physical Review Letters**, American Physical Society (APS), v. 111, n. 10, p. 106801, sep 2013.

JOHARI, P.; SHENOY, V. B. Tuning the electronic properties of semiconducting transition metal dichalcogenides by applying mechanical strains. **ACS Nano**, American Chemical Society (ACS), v. 6, n. 6, p. 5449–5456, may 2012.

JOHN, A. P.; THENAPPARAMBIL, A.; THALAKULAM, M. Strain-engineering the schottky barrier and electrical transport on MoS2. **Nanotechnology**, IOP Publishing, v. 31, n. 27, p. 275703, apr 2020.

KAUR, J.; KANT, R. Curvature-induced anomalous enhancement in the work function of nanostructures. **The Journal of Physical Chemistry Letters**, American Chemical Society (ACS), v. 6, n. 15, p. 2870–2874, jul 2015.

KELLY, P. **Properties of Materials**. [S.l.]: CRC Press, 2014.

KIM, S. J.; KIM, D.; MIN, B. K.; YI, Y.; MONDAL, S.; NGUYEN, V.-T.; HWANG, J.; SUH, D.; CHO, K.; CHOI, C.-G. Bandgap tuned WS 2 thin-film photodetector by strain gradient in van der waals effective homojunctions. **Advanced Optical Materials**, Wiley, v. 9, n. 22, p. 2101310, sep 2021.

KITTEL, C. **Kittel's Introduction to Solid State Physics**. [S.l.]: Wiley Sons, Limited, John, 2018. 1 p. ISBN 9781119454168.

KLYUKANOV, A. A.; GASHIN, P.; SCURTU, R. Ideality factor in transport theory of schottky barrier diodes. **arXiv: Materials Science**, 2012.

LEE, C.; YAN, H.; BRUS, L. E.; HEINZ, T. F.; HONE, J.; RYU, S. Anomalous lattice vibrations of single- and few-layer MoS2. **ACS Nano**, American Chemical Society (ACS), v. 4, n. 5, p. 2695–2700, apr 2010.

LEVY, N.; BURKE, S. A.; MEAKER, K. L.; PANLASIGUI, M.; ZETTL, A.; GUINEA, F.; NETO, A. H. C.; CROMMIE, M. F. Strain-induced pseudo–magnetic fields greater than 300 tesla in graphene nanobubbles. **Science**, American Association for the Advancement of Science (AAAS), v. 329, n. 5991, p. 544–547, jul 2010.

LI, H.; JIA, X.; ZHANG, Q.; WANG, X. Metallic transition-metal dichalcogenide nanocatalysts for energy conversion. **Chem**, Elsevier BV, v. 4, n. 7, p. 1510–1537, jul 2018.

LI, Y. **Probing the Response of Two-Dimensional Crystals by Optical Spectroscopy**. [S.l.]: Springer International Publishing, 2016.

LIN, Y.; LING, X.; YU, L.; HUANG, S.; HSU, A. L.; LEE, Y.-H.; KONG, J.; DRESSELHAUS, M. S.; PALACIOS, T. Dielectric screening of excitons and trions in single-layer MoS2. **Nano Letters**, American Chemical Society (ACS), v. 14, n. 10, p. 5569–5576, sep 2014.

LIU, B.; WU, L.-J.; ZHAO, Y.-Q.; WANG, L.-Z.; CAI, M.-Q. Tuning the schottky barrier height of the pd–MoS2 contact by different strains. **Physical Chemistry Chemical Physics**, Royal Society of Chemistry (RSC), v. 17, n. 40, p. 27088–27093, 2015.

LIU, Y.; GUO, J.; ZHU, E.; LIAO, L.; LEE, S.-J.; DING, M.; SHAKIR, I.; GAMBIN, V.; HUANG, Y.; DUAN, X. Approaching the schottky–mott limit in van der waals metal–semiconductor junctions. **Nature**, Springer Science and Business Media LLC, v. 557, n. 7707, p. 696–700, may 2018.

MAIER, S. A. **Plasmonics**: Fundamentals and applications. [S.l.]: Springer, 2007. 248 p. ISBN 9780387331508.

MAK, K. F.; LEE, C.; HONE, J.; SHAN, J.; HEINZ, T. F. Atomically thin MoS2: A new direct-gap semiconductor. **Physical Review Letters**, American Physical Society (APS), v. 105, n. 13, p. 136805, sep 2010.

MANZELI, S.; ALLAIN, A.; GHADIMI, A.; KIS, A. Piezoresistivity and strain-induced band gap tuning in atomically thin MoS2. **Nano Letters**, American Chemical Society (ACS), v. 15, n. 8, p. 5330–5335, jul 2015.

MANZELI, S.; OVCHINNIKOV, D.; PASQUIER, D.; YAZYEV, O. V.; KIS, A. 2d transition metal dichalcogenides. **Nature Reviews Materials**, Springer Science and Business Media LLC, v. 2, n. 8, jun 2017.

MUELLER, N. S.; OKAMURA, Y.; VIEIRA, B. G. M.; JUERGENSEN, S.; LANGE, H.; BARROS, E. B.; SCHULZ, F.; REICH, S. Deep strong light–matter coupling in plasmonic nanoparticle crystals. **Nature**, Springer Science and Business Media LLC, v. 583, n. 7818, p. 780–784, jul 2020.

MUELLER, N. S.; PFITZNER, E.; OKAMURA, Y.; GORDEEV, G.; KUSCH, P.; LANGE, H.; HEBERLE, J.; SCHULZ, F.; REICH, S. Surface-enhanced raman scattering and surface-enhanced infrared absorption by plasmon polaritons in three-dimensional nanoparticle supercrystals. **ACS Nano**, American Chemical Society (ACS), v. 15, n. 3, p. 5523–5533, mar 2021.

MUELLER, N. S.; VIEIRA, B. G. M.; SCHULZ, F.; KUSCH, P.; ODDONE, V.; BARROS, E. B.; LANGE, H.; REICH, S. Dark interlayer plasmons in colloidal gold nanoparticle bi- and few-layers. **ACS Photonics**, American Chemical Society (ACS), v. 5, n. 10, p. 3962–3969, oct 2018.

MUELLER, T.; MALIC, E. Exciton physics and device application of two-dimensional transition metal dichalcogenide semiconductors. **npj 2D Materials and Applications**, Springer Science and Business Media LLC, v. 2, n. 1, sep 2018.

NANOWORLD. **EFM tip**. 2020. Available at: https://www.nanoworld.com/pointprobe-electrostatic-force-microscopy-afm-tip-efm.

NAYAK, A. P.; BHATTACHARYYA, S.; ZHU, J.; LIU, J.; WU, X.; PANDEY, T.; JIN, C.; SINGH, A. K.; AKINWANDE, D.; LIN, J.-F. Pressure-induced semiconducting to metallic transition in multilayered molybdenum disulphide. **Nature Communications**, Springer Science and Business Media LLC, v. 5, n. 1, may 2014.

NERI, I.; LÓPEZ-SUÁREZ, M. Electronic transport modulation on suspended few-layer MoS2 under strain. **Physical Review B**, American Physical Society (APS), v. 97, n. 24, p. 241408, jun 2018.

NOBELPRIZE.ORG. **The Nobel Prize in Physics 2010. Nobel Prize Outreach AB 2023.** 2023. Available at: https://www.nobelprize.org/prizes/physics/2010/summary.

NOVOSELOV, K. S.; GEIM, A. K.; MOROZOV, S. V.; JIANG, D.; ZHANG, Y.; DUBONOS, S. V.; GRIGORIEVA, I. V.; FIRSOV, A. A. Electric field effect in atomically thin carbon films. **Science**, American Association for the Advancement of Science (AAAS), v. 306, n. 5696, p. 666–669, oct 2004.

NOVOSELOV, K. S.; JIANG, D.; SCHEDIN, F.; BOOTH, T. J.; KHOTKEVICH, V. V.; MOROZOV, S. V.; GEIM, A. K. Two-dimensional atomic crystals. **Proceedings of the National Academy of Sciences**, Proceedings of the National Academy of Sciences, v. 102, n. 30, p. 10451–10453, jul 2005.

NOVOSELOV, K. S.; MISHCHENKO, A.; CARVALHO, A.; NETO, A. H. C. 2d materials and van der waals heterostructures. **Science**, American Association for the Advancement of Science (AAAS), v. 353, n. 6298, jul 2016.

OHDOMARI, I.; TU, K. N. Parallel silicide contacts. **Journal of Applied Physics**, AIP Publishing, v. 51, n. 7, p. 3735–3739, jul 1980.

OTTAVIANO, L.; PALLESCHI, S.; PERROZZI, F.; D'OLIMPIO, G.; PRIANTE, F.; DONARELLI, M.; BENASSI, P.; NARDONE, M.; GONCHIGSUREN, M.; GOMBOSUREN, M.; LUCIA, A.; MOCCIA, G.; CACIOPPO, O. A. Mechanical exfoliation and layer number identification of MoS 2 revisited. **2D Materials**, IOP Publishing, v. 4, n. 4, p. 045013, sep 2017.

PATHAK, C. S.; GARG, M.; SINGH, J. P.; SINGH, R. Current transport properties of monolayer graphene/n-si schottky diodes. **Semiconductor Science and Technology**, IOP Publishing, v. 33, n. 5, p. 055006, apr 2018.

PEAK-O-MAT 1.2.9. 2020. Available at: https://qceha.net/.

PENG, Z.; CHEN, X.; FAN, Y.; SROLOVITZ, D. J.; LEI, D. Strain engineering of 2d semiconductors and graphene: from strain fields to band-structure tuning and photonic applications. **Light: Science &amp Applications**, Springer Science and Business Media LLC, v. 9, n. 1, nov 2020.

POSTORINO, S.; GRASSANO, D.; D'ALESSANDRO, M.; PIANETTI, A.; PULCI, O.; PALUMMO, M. Strain-induced effects on the electronic properties of 2d materials. **Nanomaterials and Nanotechnology**, SAGE Publications, v. 10, p. 184798042090256, jan 2020.

PRINCETON, L. S. 2023. Available at: http://web.princeton.edu/sites/ehs/labsafetymanual/cheminfo/aquaregia.htm.

QI, J.; LAN, Y.-W.; STIEG, A. Z.; CHEN, J.-H.; ZHONG, Y.-L.; LI, L.-J.; CHEN, C.-D.; ZHANG, Y.; WANG, K. L. Piezoelectric effect in chemical vapour deposition-grown atomic-monolayer triangular molybdenum disulfide piezotronics. **Nature Communications**, Springer Science and Business Media LLC, v. 6, n. 1, jun 2015.

QUEREDA, J.; PALACIOS, J. J.; AGRäIT, N.; CASTELLANOS-GOMEZ, A.; RUBIO-BOLLINGER, G. Strain engineering of schottky barriers in single- and few-layer MoS 2 vertical devices. **2D Materials**, IOP Publishing, v. 4, n. 2, p. 021006, jan 2017.

RT, T. The physics and chemistry of the schottky barrier height. **Applied Physics Reviews**, AIP Publishing, v. 1, n. 1, p. 011304, mar 2014.

SCHULZ, F.; TOBER, S.; LANGE, H. Size-dependent phase transfer functionalization of gold nanoparticles to promote well-ordered self-assembly. **Langmuir**, American Chemical Society (ACS), v. 33, n. 50, p. 14437–14444, dec 2017.

SHEN, T.; PENUMATCHA, A. V.; APPENZELLER, J. Strain engineering for transition metal dichalcogenides based field effect transistors. **ACS Nano**, v. 10, n. 4, p. 4712–4718, 2016. PMID: 27043387. Available at: https://doi.org/10.1021/acsnano.6b01149.

SHI, H.; PAN, H.; ZHANG, Y.-W.; YAKOBSON, B. I. Quasiparticle band structures and optical properties of strained monolayer MoS2. **Physical Review B**, American Physical Society (APS), v. 87, n. 15, p. 155304, apr 2013.

SMYTH, C. M.; ADDOU, R.; MCDONNELL, S.; HINKLE, C. L.; WALLACE, R. M. Contact metal–MoS2 interfacial reactions and potential implications on MoS2-based device performance. **The Journal of Physical Chemistry C**, American Chemical Society (ACS), v. 120, n. 27, p. 14719–14729, jun 2016.

SONG, S.; KEUM, D. H.; CHO, S.; PERELLO, D.; KIM, Y.; LEE, Y. H. Room temperature semiconductor–metal transition of MoTe2 thin films engineered by strain. **Nano Letters**, American Chemical Society (ACS), v. 16, n. 1, p. 188–193, dec 2015.

SPLENDIANI, A.; SUN, L.; ZHANG, Y.; LI, T.; KIM, J.; CHIM, C.-Y.; GALLI, G.; WANG, F. Emerging photoluminescence in monolayer MoS2. **Nano Letters**, American Chemical Society (ACS), v. 10, n. 4, p. 1271–1275, mar 2010.

TIU, Z. C.; OOI, S. I.; GUO, J.; ZHANG, H.; AHMAD, H. Review: application of transition metal dichalcogenide in pulsed fiber laser system. **Materials Research Express**, IOP Publishing, v. 6, n. 8, p. 082004, may 2019.

TUNG, R. T. Electron transport at metal-semiconductor interfaces: General theory. **Physical Review B**, American Physical Society (APS), v. 45, n. 23, p. 13509–13523, jun 1992.

WALLACE, P. R. The band theory of graphite. **Physical Review**, American Physical Society (APS), v. 71, n. 9, p. 622–634, may 1947.

WANG, Q. H.; KALANTAR-ZADEH, K.; KIS, A.; COLEMAN, J. N.; STRANO, M. S. Electronics and optoelectronics of two-dimensional transition metal dichalcogenides. **Nature Nanotechnology**, Springer Science and Business Media LLC, v. 7, n. 11, p. 699–712, nov 2012.

WILSON, J.; YOFFE, A. The transition metal dichalcogenides discussion and interpretation of the observed optical, electrical and structural properties. **Advances in Physics**, Informa UK Limited, v. 18, n. 73, p. 193–335, may 1969.

WU, W.; WANG, L.; LI, Y.; ZHANG, F.; LIN, L.; NIU, S.; CHENET, D.; ZHANG, X.; HAO, Y.; HEINZ, T. F.; HONE, J.; WANG, Z. L. Piezoelectricity of single-atomic-layer MoS2 for energy conversion and piezotronics. **Nature**, Springer Science and Business Media LLC, v. 514, n. 7523, p. 470–474, oct 2014.

YANG, S.; WANG, C.; SAHIN, H.; CHEN, H.; LI, Y.; LI, S.-S.; SUSLU, A.; PEETERS, F. M.; LIU, Q.; LI, J.; TONGAY, S. Tuning the optical, magnetic, and electrical properties of ReSe2 by nanoscale strain engineering. **Nano Letters**, American Chemical Society (ACS), v. 15, n. 3, p. 1660–1666, feb 2015.

YU PETER Y., C. M. **Fundamentals of semiconductors**: physics and materials properties. [S.l.]: Springer, 1996. 617 p. ISBN 3540614613.

YUE, Q.; KANG, J.; SHAO, Z.; ZHANG, X.; CHANG, S.; WANG, G.; QIN, S.; LI, J. Mechanical and electronic properties of monolayer MoS2 under elastic strain. **Physics Letters A**, Elsevier BV, v. 376, n. 12-13, p. 1166–1170, feb 2012.

ZHANG, Z.; LI, L.; HORNG, J.; WANG, N. Z.; YANG, F.; YU, Y.; ZHANG, Y.; CHEN, G.; WATANABE, K.; TANIGUCHI, T.; CHEN, X. H.; WANG, F.; ZHANG, Y. Strain-modulated bandgap and piezo-resistive effect in black phosphorus field-effect transistors. **Nano Letters**, American Chemical Society (ACS), v. 17, n. 10, p. 6097–6103, sep 2017.

ZHAO, Y.; LUO, X.; LI, H.; ZHANG, J.; ARAUJO, P. T.; GAN, C. K.; WU, J.; ZHANG, H.; QUEK, S. Y.; DRESSELHAUS, M. S.; XIONG, Q. Interlayer breathing and shear modes in few-trilayer MoS2 and WSe2. **Nano Letters**, American Chemical Society (ACS), v. 13, n. 3, p. 1007–1015, mar 2013.

ZHU, C. R.; WANG, G.; LIU, B. L.; MARIE, X.; QIAO, X. F.; ZHANG, X.; WU, X. X.; FAN, H.; TAN, P. H.; AMAND, T.; URBASZEK, B. Strain tuning of optical emission energy and polarization in monolayer and bilayer MoS2. **Physical Review B**, American Physical Society (APS), v. 88, n. 12, p. 121301, sep 2013.

ZIBOUCHE, N.; KUC, A.; MUSFELDT, J.; HEINE, T. Transition-metal dichalcogenides for spintronic applications. **Annalen der Physik**, Wiley, v. 526, n. 9-10, p. 395–401, aug 2014.

APPENDIX A – EXTRA FIGURES FROM CHAPTER 5

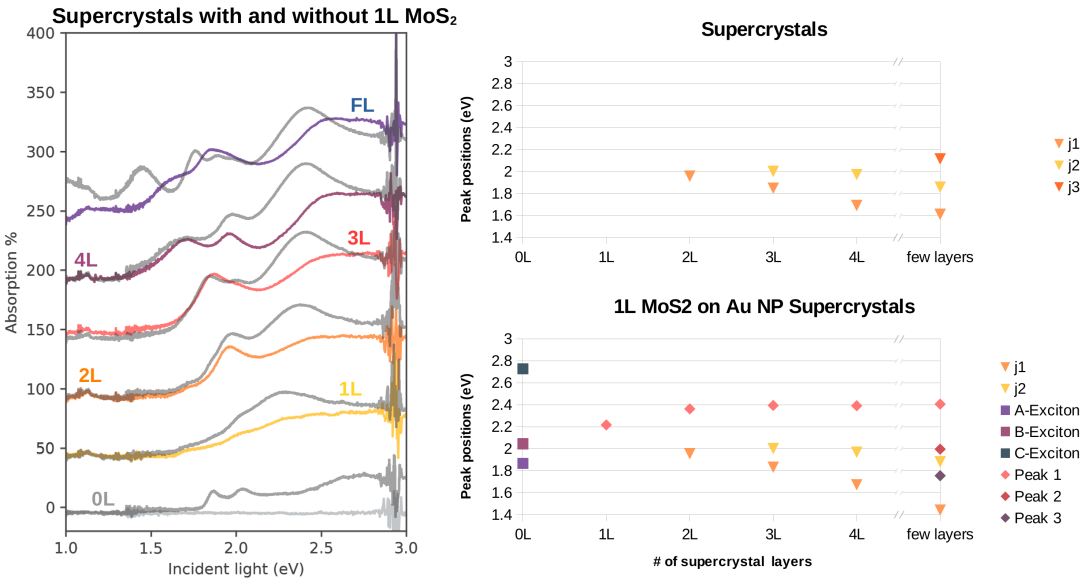

Figure 23 – Superposition of absorption spectra of uncovered supercrystal (in colour) and supercrystal with 1L MoS_2 on top (dark grey), for different number of layers. Plotted on the right are the peak positions found by the fitting procedure of the compared spectra.

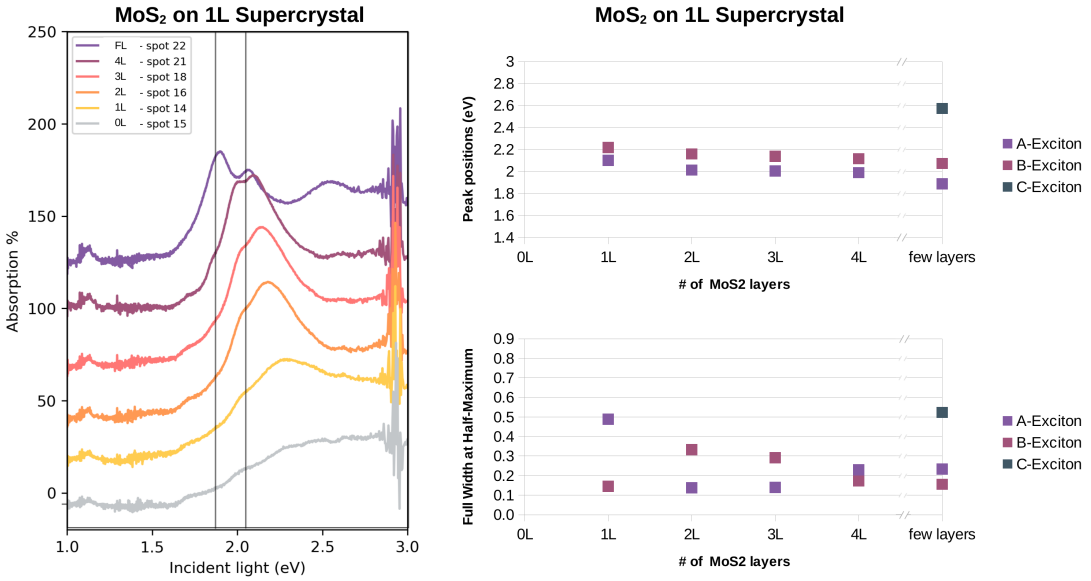

Figure 24 – Absorption spectra for varied number of MoS_2 layers on top of a monolayer supercrystal. With the positions (top-right) and full width at half-maximum (bottom-right) of the peaks found in the fitting procedure for the corresponding spectra. Vertical lines are placed in the position of the A and B excitons of pristine MoS_2.

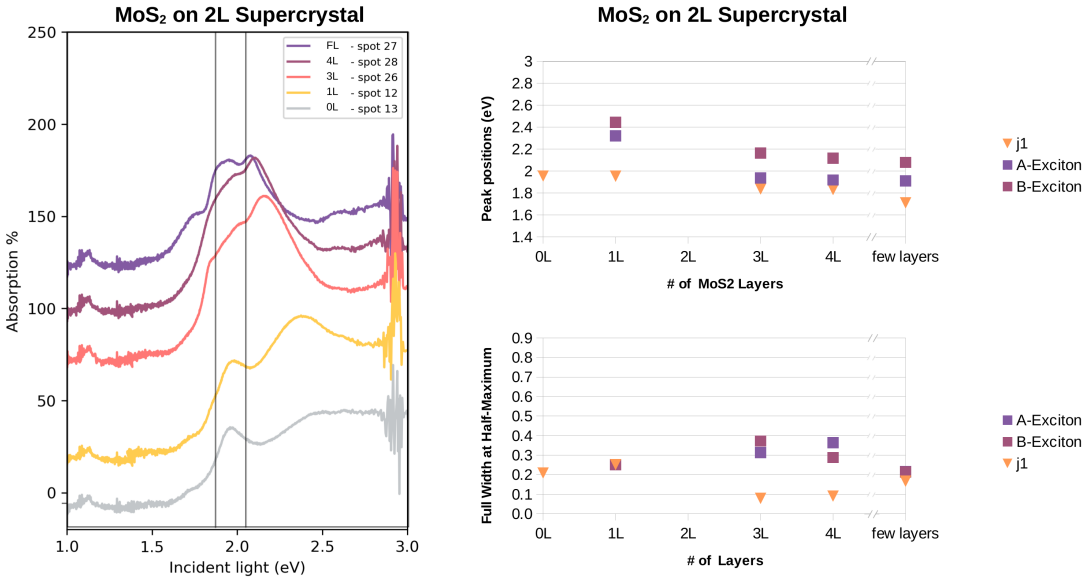

Figure 25 – Absorption spectra for varied number of MoS_2 layers on top of a bi-layer supercrystal. With the positions (top-right) and full width at half-maximum (bottom-right) of the peaks found in the fitting procedure for the corresponding spectra. Vertical lines are placed in the position of the A and B excitons of pristine MoS_2.

APPENDIX B – PREPARAÇÃO DE AMOSTRA: SUPERCRISTAIS

Traduzido da seção 3.2.1.

Em 2020, o grupo da Profa. Reich publicou um artigo intitulado “Acoplamento luz-matéria profundamente forte em cristais de nanopartículas plasmônicas”(MUELLER *et al.*, 2020), eles mostraram experimentalmente que supercristais de NPs de Au (≥ 30 nm) têm a maior interação luz-matéria já registrada, tudo em condições ambientais. Em setembro de 2021, comecei minha experiência sanduíche com o grupo mencionado acima me hospedando na Freie Universität Berlin. Enquanto estava no exterior, tive a sorte de ser treinado (juntamente com MSc. Arseniy Epshin) em primeira mão pelo Dr. Florian Shulz, pesquisador da Universität Hamburg responsável por produzir as amostras no artigo mencionado(SCHULZ *et al.*, 2017). Apresento o passo a passo deste procedimento, com o intuito de servir de guia para os pesquisadores que desejam produzir seus próprios supercristais de nanopartículas de ouro. Também é meu dever científico de disseminar conhecimento - pensando nisso, **apresento aqui uma versão dos procedimentos em PORTUGUÊS**.

Para este procedimento utilizamos: água Milli-Q ultra pura (18.2 MΩ.cm), ácido tetracloroáurico(III) ($HAuCl_4 \cdot 3H_2O$) (≥99.9%), brometo de cetrimônio (CTAB) (≥98%), boro-hidreto de sódio ($NaBH_4$) (≥98%), cloreto de cetrimônio (CTAC) (≥ 98%), ácido L-ascórbico (AA) (≥99,0%), poliestireno terminado em tiol (PSSH) (com uma variedade de massas molares, todos da Polymer Source - Canadá), tetrahidrofurano (THF) (≥99,5%), tolueno (≥99,5%), etanol (≥96%), dietilenoglicol (DEG), ácido nítrico (HNO_3) e ácido clorídrico (HCl).

É importante observar que qualquer impureza no crescimento pode levar à formação irregular de aglomerados e nanopartículas, por isso é fundamental o uso de água Milli-Q durante todo o procedimento. As vidrarias utilizadas para o manuseio das soluções de ouro devem ser utilizadas somente para este fim, sendo limpas com Água Régia entre os usos consecutivos. Para preparar a Água régia, a coordenadora de segurança do laboratório de química, Dra. Katayoun Hubmann, misturou ácido nítrico e ácido clorídrico na proporção de 1:3 - é preciso ter cuidado com essa substância pois tem poder corrosivo muito forte - sempre foi manuseado com equipamento de proteção dentro de uma capela devido à liberação de gases tóxicos(PRINCETON, 2023). Para estimar o tamanho das partículas nas soluções intermediárias, pode-se usar a absorbância (UV/Vis) a 450 nm, conforme descrito por Haiss *et al.*(HAISS *et al.*, 2007).

Para facilitar a maioria dos procedimentos, preparamos previamente as soluções aquosas robustas, em sua forma mais concentrada, com armazenamento adequado - $HAuCl_4$ (0,5

mM, 500 mL), armazenadas em recipiente fechado e escuro no refrigerador; CTAB (200 mM, 50 mL, 3,64 g), armazenado em recipiente fechado na prateleira; CTAC (200 mM, 100 mL, 6,39 g), armazenado em recipiente fechado na prateleira. Se a solução de CTAB (ou CTAC) parecesse ter cristalizado, nós a sonicamos com um sonicador de banho até que estivesse completamente dissolvida novamente. Dessa forma, as únicas soluções com as quais tínhamos que nos preocupar durante o crescimento dos NPs eram as menos concentradas (que eram facilmente produzidas por diluição) e as soluções instáveis ($NaBH_4$, AA).

B.1 Aglomerados de Au

Nesta etapa, produzimos pequenos aglomerados de ouro (∼2 nm) reduzindo (com $NaBH_4$) o ouro em $HAuCl_4$ em um ambiente rico em CTAB. As moléculas CTAB encapsulam e estabilizam o ouro metálico.

Usando um agitador magnético a 800 rpm, misturamos CTAB (200 mM, 5 mL) e $HAuCl_4$ (0,5 mM, 5 mL). $NaBH_4$ aquoso recém-preparado (10 mM, 0,6 mL de 4 mg em 10,5 mL) foi adicionado com uma pipeta por injeção única na solução de ouro-CTAB agitada (800 rpm) (Fig. 26 (a)), a solução tornou-se marrom. Após dois minutos, a agitação foi desligada e a solução foi mantida aberta e em repouso por 3 horas na capela para garantir a conversão do barohidreto de sódio (há formação de H_2). A mistura foi feita em banho-maria a 27ºC. Com isso, produzimos aglomerados de Au encapsulados por CTAB (<5 nm). Esta solução pode ser mantida na geladeira para uso futuro, mas o armazenamento a longo prazo (mais de alguns meses) não é recomendado.

B.2 Nanoesferas de primeira geração (∼ 10*nm*)

Nesta etapa mudamos o agente de encapsulamento para CTAC e aumentamos os aglomerados de Au reduzindo $HAuCl_4$ (desta vez com o agente leve AA) na superfície dos clusters de Au formados anteriormente. Se as nanopartículas fossem deixadas para serem crescidas na solução de CTAB elas evoluiriam para nanobastões, o CTAC garante a forma esférica. O excesso de CTAB é lavado.

Em um cilindro volumétrico, misturamos 20 mL de CTAC (200 mM) com 15 mL de AA (100 mM, de 0,89 g em 50 mL), 500 µL da solução cluster da Sec. B.1 foi adicionado e a mistura foi sonicada em banho por 5 minutos, a solução foi colocada em um béquer e agitada

a 600 rpm. 20 mL de $HAuCl_4$ (0,5 mM) foram adicionados à mistura agitada (600 rpm) por meio de injeção única com uma pipeta volumétrica enquanto pressionava o balão, Fig. 26 (b). A solução ficou vermelha imediatamente. A agitação foi desligada e a solução foi mantida em repouso por 20 minutos. Para ajustar o tamanho das NPs pode-se reduzir o volume da solução de cluster usada aqui, levando a nanopartículas maiores de primeira geração.

Para limpar a solução do CTAB e tornar a distribuição de tamanho das nanopartículas mais estreita, colocamos a solução em eppendorfs (24x2 mL - eppendorfs maiores podem ser usados se tivermos acesso a uma centrífuga grande) e centrifugamos por 30 min a 20.000 g (15ºC). Se a solução ainda apresentar coloração homogênea depois, centrifugue-a por períodos mais longos. O sobrenadante foi removido dos eppendorfs (a solução foi colocada em apenas dois eppendorfs de 2 mL) e água Milli-Q (2 mL, 1 mL por eppendorf) foi adicionada. Fizemos uma segunda e uma terceira centrifugação (20 min, 20.000 g), sendo o sobrenadante removido e substituído por CTAC (20 mM, 2 mL) duas vezes. Etapas extras de lavagem apenas melhorarão a qualidade da solução concentrada final. A solução foi diluída em 10 mL de CTAC (20 mM) e armazenada em geladeira (podendo assim ser conservada por até 6 meses).

B.3 Nanosferas de segunda geração ($> 20nm$)

Nanopartículas de primeira geração são usadas como sementes e a redução lenta de $HAuCl_4$ é usada para crescer homogeneamente as partículas, com CTAC como agente de encapsulamento. A centrifugação é usada para limpar a solução, garantindo uma estreita distribuição dos diâmetros das nanoesferas. O crescimento adicional das partículas é possível usando partículas de segunda (ou superior) geração como sementes.

Um béquer limpo foi colocado em banho-maria a 27ºC com agitação magnética a 400 rpm. Nela adicionamos 20 mL de CTAC (100 mM), 500 µL de sementes (nanoesferas de 1ª geração da Sec. 3.2.1.2) e 130 µL de AA fresco (100 mM). Reduzir o volume das sementes reduz o número de NPs e aumenta o tamanho das nanoesferas da próxima geração. Utilizamos uma bomba de seringa (na vazão de 20 mL/h) para adicionar 20 mL de $HAuCl_4$ (0,5 mM) gota a gota à mistura agitada (400 rpm), para isso utilizamos uma seringa plástica limpa com uma extensão de teflon - não é recomendado o uso de peças metálicas para manipular $HAuCl_4$, pois irão reduzir o ouro que deve ser reduzido apenas na superfície das sementes.

A solução foi limpa sendo colocada em eppendorfs e centrifugada (ver tabela 4) três vezes, com o sobrenadante substituído por 2 mL de água Milli-Q em cada etapa - a concentração

de CTAC não deve cair abaixo de 5 mM, se necessário adicionar 2 mL de CTAC (20 mM) em vez de água. Etapas extras de lavagem podem ser feitas dependendo da qualidade da solução e dos cuidados do pesquisador. As especificações para a centrifugação (tabela 4) dependem do tamanho da partícula, isso pode ser um palpite do pesquisador experiente ou estimado a partir do espectro UV/Vis da solução(HAISS *et al.*, 2007). Para armazenar esta solução, dissolva o pellet final em 10 mL CTAC (20 mM) e guarde em geladeira, concentre-o (por centrifugação) antes de continuar os procedimentos.

Table 4 – Parâmetros de centrifugação e PSSH para cada tamanho de NP

Tamanho da geração (nm)	**Aceleração (g)**	**T1 (min)**	**T2 (min)**	**tamanho do PSSH**
<20	20.000	45	30	2k-PSSH
20	10.000	30	20	2k-PSSH
30	7.000	30	15	2k-PSSH
40	5.000	30	12	5k-PSSH
50	2.500	30	10	12k-PSSH
70	2.500	30	10	12k-PSSH

Especificações para centrifugação de Au NPs em solução em relação ao diâmetro aproximado do NP (Sec. **??**), para cada geração de tamanho a aceleração deve ser usado o tempo T1 na primeira centrifugação e T2 para qualquer outra centrifugação. Tamanho do PSSH recomendado (de acordo com o peso molar médio) para funcionalizar NPs para cada valor de diâmetro (Sec. B.4)

B.4 Funcionalização de polímeros de nanopartículas

Nesta seção a extremidade tiol do PSSH reage com a superfície do Au funcionalizando-o com um polímero, isso estabiliza as partículas, impedindo qualquer contato com suas superfícies metálicas (ver Fig. 26 (c)). A nova solução é à base de tolueno, limpamos por centrifugação com substituição do sobrenadante e por separação de fases com água e etanol - removendo todo o excesso de PSSH e quaisquer impurezas solúveis em água ou álcool. O produto é uma solução concentrada e estável de tolueno de NPs de Au revestidas com polímero.

Escolhemos o tamanho do PSSH (2k, 5k ou 12k, em referência ao seu peso molar médio) de acordo com a tabela 4, uma solução de PSSH em THF (6 mL, 0,5 mM) foi preparada em um balão de fundo redondo limpo e com um agitador magnético a 700 rpm. Os Au NPs da Sec. **??** (concentrados em $\sim$ 500 µL) foram adicionados de uma pipeta de precisão gota a gota diretamente no líquido agitado. A mistura foi deixada com 700 rpm durante a noite. Na manhã seguinte, a agitação foi interrompida, o agitador magnético foi removido do balão de fundo redondo e este foi levado ao evaporador rotativo para remover o THF e a água, Fig. 26 (e).

O rotaevaporador foi ajustado para 250 rpm, 40ºC, chegando a 11 mbar de forma escalonada, foi deixado por 30 minutos (pode ser necessário deixar por mais tempo). Os solventes foram limpos da câmara de condensação do evaporador. As nanopartículas deixadas no vidro do frasco foram dissolvidas em 1 mL de tolueno e colocadas em um eppendorf, 500 µL extras de tolueno foram usados para limpar os vestígios de NPs deixados no frasco de fundo redondo e foram colocados no mesmo eppendorf.

A solução de NP-tolueno foi centrifugada segundo a força e o tempo (T1) dados na tabela 4 por 4 vezes, cada vez o sobrenadante foi substituído por 1 mL de tolueno - isso remove o excesso de PSSH e afunila a distribuição de tamanho das NPs. Em um cilindro de vidro fino e limpo com tampa misturamos a solução de tolueno Au NP com 1 mL de Milli-Q e 1 mL de etanol. O cilindro foi fechado e agitado manualmente, foi então deixado no balcão até que as fases se separassem, Fig. 26 (f). Em seguida, usamos uma pipeta de vidro limpa, fina e de bico longo para remover a fase transparente à base de água e etanol. Esta separação de fases foi repetida mais três vezes (num total de 4 vezes, adicionando mais água e etanol antes de cada separação). Uma etapa final de centrifugação pode ser feita para aumentar a concentração das nanoesferas de ouro cobertas com PSSH à base de tolueno (de cor rosa a marrom). A solução é estável e pode ser armazenada indefinidamente em vidro com tampa resistente ao tolueno e parafilme, em geladeira.

B.5 Cristalização da superestrutura

Agora evaporamos lentamente o tolueno no topo de uma interface líquida (DEG), gerando por automontagem uma estrutura cristalina feita de nanopartículas, os supercristais. Quando o tolueno é evaporado, os supercristais ficam flutuando em DEG, a subfase DEG líquida é drenada até que os supercristais sejam expostos a um substrato de vidro que foi previamente submerso. Os supercristais são fixados na lâmina de vidro, o tolueno e DEG residuais são removidos da amostra por evaporação a vácuo.

Um pequeno pedaço de lâmina de vidro limpa (o substrato alvo) foi colocado no fundo de um poço de Teflon (∼1cm de diâmetro), o substrato foi submerso em DEG (300 µL), o o líquido cobriu ∼60% do poço (cuidado para não deixar bolhas sob o substrato). Uma mistura 1:3 de Au NPs (da Sec. B.4) e tolueno foi pipetada no topo do DEG e o poço foi coberto com uma lâmina de vidro fina. O poço foi deixado intacto na capela por dois dias para a completa evaporação do tolueno, uma fina película reflexiva pode ser vista na superfície da subfase DEG.

O DEG foi drenado com uma seringa através de um orifício de 1 mm de espessura no fundo do poço de Teflon, deixando os supercristais presos ao substrato alvo. As superfícies dos vidros foram delicadamente secas com papel (cuidado para não tocar nos supercristais), em seguida o substrato com os supercristais foi levado a uma câmara de vácuo de 1 mbar por 3 horas para secar completamente a amostra de tolueno e DEG. Um esquema do poço é representado na figura 26 (f), os supercristais são representados na Fig. 15.

Pode-se controlar a velocidade de evaporação do tolueno alterando o volume de ar no poço (usando mais DEG), mais ar equivale a uma evaporação mais rápida; e/ou adicionando um peso em cima da tampa deslizante (evaporação mais lenta) ou não cobrindo completamente o poço (evaporação mais rápida). A evaporação rápida leva a amostras de supercristais mais finos. Aumentar o volume da solução de NPs-tolueno aumenta a espessura média dos supercristais gerados. Diferentes substratos podem ser submersos em DEG, e também é possível pescar os supercristais flutuantes antes de drenar a subfase (essa "pesca" foi usada para pequenas grades TEM), também pode-se usar uma pipeta para drenar o DEG.

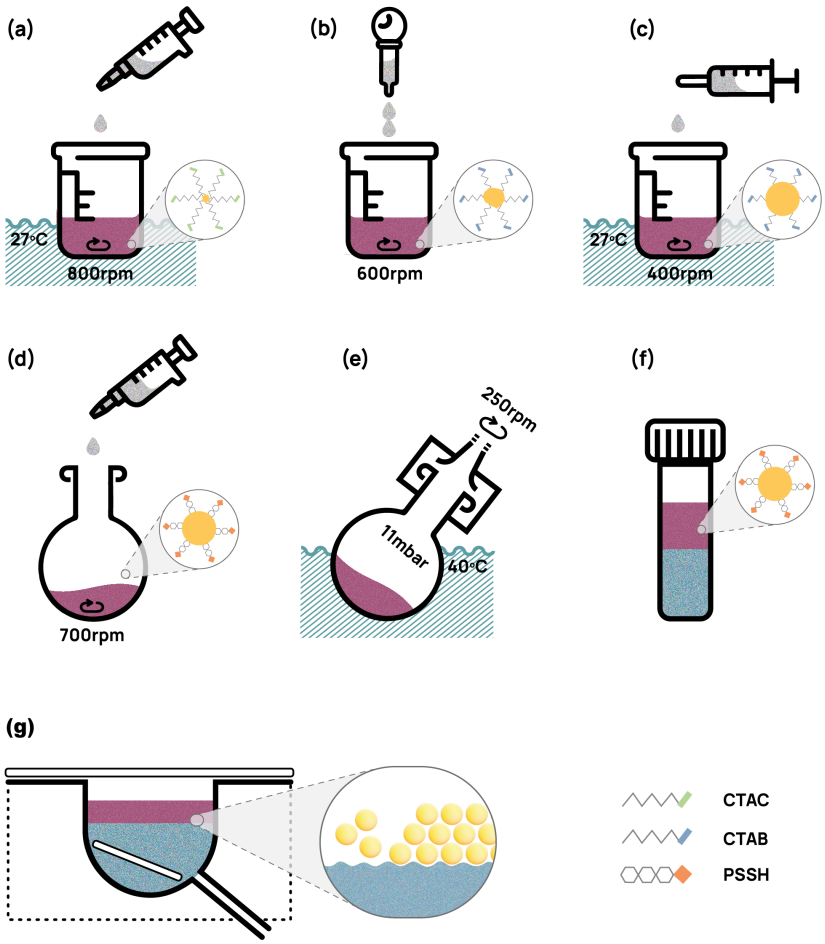

Figure 26 – Passos principais no crescimento de nanopartículas e formação de supercristais, com zoom na configuração das partículas após cada etapa representada, veja as representações simplistas das moléculas de encapsulamento CTAB, CTAC e PSSH no canto inferior direito canto da figura. (a) Formação de aglomerados de Au encapsulados com CTAB via injeção única de $NaBH_4$ em solução de $HAuCl_4$-CTAB em banho-maria a 27ºC e com agitador magnético a 800 rpm (Sec. B.1). (b) Geração de NPs esféricas de primeira geração, pressiona-se o balão preso à pipeta volumétrica para injetar rapidamente 20 mL de $HAuCl_4$ na solução de aglomerados em CTAC, a agitação magnética é de 600 rpm (Sec. B.2). (c) As NPs de segunda geração são formadas por meio de adição gota a gota de 20 mL de $HAuCl_4$ (durante 1 hora com uma bomba para seringa) às NPs de 1ª geração em CTAC, feito em banho-maria a 27ºC e com agitação magnética a 400 rpm (Sec. B.3). A etapa (c) pode ser repetida para crescer nanopartículas maiores. (d) As partículas são funcionalizadas com o PSSH específico (ver tabela 4) usando uma pipeta para adicionar gota a gota 0,5 mL de NPs em CTAC a uma solução de THF e PSSH agitada a 700 rpm. (e) THF e água são evaporados da solução em rotaevaporador a 250 rpm com banho-maria a 40ºC, deixando as nanopartículas secas na parede do balão de fundo redondo para serem posteriormente dissolvidas em tolueno (Sec. B.4). (f) Com as NPs funcionalizadas com PSSH dissolvidas em tolueno, um procedimento de separação de fases é feito misturando e agitando água e etanol em um frasco com tampa, quaisquer moléculas residuais solúveis em água ou etanol são removidas separando as fases no frasco. (g) A solução final de NPs com PSSH é colocada em cima de DEG em um poço de Teflon. À medida que o tolueno evapora, forma-se o supercristal na subfase líquida (visível no zoom). O substrato final é visível dentro da subfase DEG, uma lâmina de vidro fina é colocada no topo do poço de Teflon para que o tolueno evapore lentamente. Quando o tolueno evapora os supercristais ficam flutuando, uma seringa é colocada no orifício (1 mm) no fundo do poço e o DEG é cuidadosamente removido, deixando os supercristais no substrato.